

CONTROL OF SYSTEMS WITH HYSTERESIS USING SERVOCOMPENSATORS

By

Alexander James Esbrook

A DISSERTATION

Submitted to
Michigan State University
in partial fulfillment of the requirements
for the degree of

DOCTOR OF PHILOSOPHY

Electrical Engineering

2012

ABSTRACT

CONTROL OF SYSTEMS WITH HYSTERESIS USING SERVOCOMPENSATORS

By

Alexander James Esbrook

The tracking problem in systems with hysteresis has become an important topic of research in the past two decades, due in large part to advances in smart material actuators. In particular, applications like Scanning Probe Microscopy require high performance from hysteretic smart material actuators. Servocompensators, or internal model controllers, have been used successfully in many varieties of tracking problems for both linear and nonlinear systems; therefore, their application to systems with hysteresis is considered in this dissertation.

The use of Multi-Harmonic Servocompensator (MHSC) is first proposed to simultaneously compensate for hysteresis and enable high-bandwidth tracking in systems with hysteresis, such as nanopositioners. With the model represented by linear dynamics preceded with a Prandtl-Ishlinskii hysteresis operator, the stability and periodicity of the closed-loop system's solutions are established when hysteresis inversion is included in the controller. Experiments on a commercial nanopositioner show that, with the proposed method, tracking can be achieved for a 200 Hz reference signal with 0.52% mean error and 1.5% peak error over a travel range of 40 μm . Additionally, the proposed method is shown at high frequencies to be superior to Iterative Learning Control (ILC), a common technique in nanopositioning control.

The theoretical and practical weaknesses of the proposed approach are then addressed. First, the design of a novel adaptive servocompensator specialized to systems with hysteresis is presented, based on frequency estimation coupled with slow adaptation, and the stability in cases with one, two, or n unknown frequencies are established. Next, a condition in the form of a Linear

Matrix Inequality is presented proving the stability of the proposed MHSC when hysteresis inversion is not used. It is then experimentally demonstrated that removing hysteresis inversion further reduces the tracking error achievable by the MHSC. Finally, the properties of self-excited limit cycles are studied for an integral-controlled system containing a play operator. A Newton-Raphson algorithm is formulated to calculate the limit cycles, and linear relationships between the amplitude and period of these limit cycles and system parameters are obtained.

ACKNOWLEDGMENTS

I am first and foremost thankful for my family. I would like to thank my Mother and Father, Rachael and James, for their everlasting support in my endeavors, and for making me stand in corners long enough to learn the meaning of the word work. I would also like to acknowledge the support of my Brothers, James and Eric, and my Sister, Emily, for their encouragement and support. I am also grateful to my girlfriend Tabitha, who has stood by me through the long nights and hard days this past year.

I am also tremendously grateful to Dr. Xiaobo Tan for encouraging me to pursue a career in research, pushing me to excel in my studies, and for providing technical and editorial support throughout my PhD study. I will be forever grateful for the opportunities he has provided me in my career. Dr. Hassan K. Khalil has also been invaluable in aiding me in my research. I am also grateful to Dr. George Zhu and Dr. Ning Xi for serving on my graduate committee.

Finally, I would like to thank the National Science Foundation (CMMI 0824830) for their monetary support of my research.

TABLE OF CONTENTS

List of Tables	viii
List of Figures	ix
Chapter 1 Introduction	1
1.1 Systems with Hysteresis	1
1.2 Control of Systems with Hysteresis: Existing work	5
1.2.1 Inversion-Focused Methods	6
1.2.2 Rejection-Focused Methods	7
1.3 The Multi-Harmonic Servocompensator: Union of Design Philosophies	8
1.4 Overview of Contributions	10
Chapter 2 Overview of Hysteresis Models	14
2.1 Introduction	14
2.2 The Prandtl-Ishlinskii Operator	14
2.3 Modified Prandtl-Ishlinskii Operator	19
2.4 The Preisach-Krasnosel'skii-Pokrovskii Operator	23
Chapter 3 Attenuation of Hysteresis through Servocompensators	25
3.1 Introduction	25
3.2 Servocompensator Design for Uncertain Systems	26
3.3 Asymptotically Stable Periodic Solutions in Systems with Hysteresis	30
3.3.1 Output Feedback Control of Systems with Servocompensators	35
3.4 Experimental Implementation of Proposed Controller	36
3.4.1 Nanopositioner Modeling	36
3.4.2 Experimental Results	41
Chapter 4 Harmonic Analysis of Hysteresis Operators with Application to Control Design for Multi-Harmonic Servocompensators	49
4.1 Introduction	49
4.2 Open-Loop Computation of Hysteresis Operator Outputs	50
4.2.1 Harmonic Analysis of a Play Operator	51
4.2.2 Example Calculations for a Sinusoidal Input	55
4.2.3 Example Calculations for a Raster/Sawtooth Input	58
4.2.4 Harmonic Analysis of a PKP Hysteron	60
4.3 Illustration in Controller Design	63

Chapter 5	A Nonlinear Adaptive Servocompensator	67
5.1	Introduction	67
5.2	Robust Adaptive Servocompensator Design	68
5.2.1	System Equations and Error System	68
5.2.2	Controller Design	73
5.2.3	Robust Adaptive Law	75
5.2.4	Partially Known Exosystem	79
5.3	Analysis of Closed-Loop System including Hysteresis	80
5.4	Experimental Results	81
5.5	Shortcomings of the Nonlinear Adaptive Servocompensator in Nanopositioning Problems	87
Chapter 6	A Frequency Estimation-Based Indirect Adaptive Servocompensator	89
6.1	Introduction	89
6.2	Problem Formulation and Controller Design	91
6.3	Analysis of the Closed-Loop System	95
6.3.1	Stability of the Boundary-Layer System	95
6.3.2	Averaging Analysis for the Case of n Unknown Frequencies: Local Exponential Stability	97
6.3.3	Averaging Analysis for the Case of One Unknown Frequency: Exponential Stability	99
6.3.4	Averaging Analysis for the Case of Two Unknown Frequencies: Exponential Stability	105
6.4	Analysis of the Closed-Loop System in the Presence of Hysteresis	110
6.5	Simulation and Experimental Results	113
6.5.1	Simulation Results for the Case of One Unknown Frequency	113
6.5.2	Experimental Results for the Case of One Unknown Frequency	114
6.5.3	Experimental Results for the Case of Two Unknown Frequencies	117
Chapter 7	Stability of Systems with Hysteresis without Hysteresis Inversion: an LMI Approach	122
7.1	Introduction	122
7.2	Sufficient Conditions for Stability in Systems with Hysteresis	125
7.2.1	Specialization to Positive-Real Systems	132
7.3	Stability of Servocompensators in Systems with Hysteresis without Hysteresis Inversion	135
7.4	Simulation Example: Verification of the LMI condition	138
7.5	Applications to Nanopositioning Control	141
Chapter 8	Properties of Self-Excited Limit Cycles in a System with Hysteresis	146
8.1	Introduction	146
8.2	Motivating Example: Issues with Rejection-focused methods	147
8.3	Self-Excited Limit Cycles in a System with Hysteresis	149
8.3.1	Computation of the Limit Cycles	153
8.3.2	Properties of the Limit Cycles	158

8.3.3	Stability of Self-Excited Limit Cycles	163
8.4	Simulation Results	165
Chapter 9	Conclusions and Future Work	170
9.1	Conclusions	170
9.2	Future Work	172
Bibliography	175

LIST OF TABLES

Table 3.1	Tracking error results for various controllers. All results are presented as a percentage of the reference amplitude ($20\mu\text{m}$).	41
Table 3.2	Tracking errors results for a Sawtooth signals. All results are presented as a percentage of the reference amplitude ($20\mu\text{m}$).	45
Table 3.3	Loading performance for MHSC and ILC. First two columns are presented as a percentage of the reference amplitude ($20\mu\text{m}$), second two columns are percent change from the unloaded case.	48
Table 4.1	Proposed algorithm's estimations of harmonic amplitude compared with actual values from closed-loop system (4.30). Setup column gives value for play radius used and the harmonic being estimated.	66
Table 5.1	Tracking error in percent of reference amplitude for adaptive servocompensator (ASC) and iterative learning (ILC) controllers	84
Table 5.2	Tracking error under varying loading conditions	85
Table 6.1	Tracking error results for proposed controllers (MHASC, ASC) and ILC. Results are presented as a percentage of the reference amplitude ($20\mu\text{m}$).	117

LIST OF FIGURES

Figure 1.1	Plasticity hysteresis curves observed in [1].	2
Figure 1.2	Illustration of Atomic Force Microscopy from [2].	3
Figure 1.3	Hysterons of several Presiach-like operators. For interpretation of the references to color in this and all other figures, the reader is referred to the electronic version of this dissertation.	4
Figure 1.4	Amplitude spectra of the output of an example hysteresis for a sinusoidal input. Primary harmonic (5 Hz) is larger than pictured.	9
Figure 2.1	Illustration of a Play Operator. r is the play radius.	15
Figure 2.2	The inversion process for hysteresis operators. u_d is the desired output, and u is the actual output.	17
Figure 2.3	Deadzone functions with positive and negative thresholds. The slopes in linear regions are unity.	19
Figure 2.4	Illustration of the PKP hysteron. This operator is parameterized by the thresholds α , β , and slope a	24
Figure 3.1	Closed-loop system with hysteresis, as defined in (3.13), (3.14), and (2.27).	31
Figure 3.2	Equivalent block diagram for the closed-loop system (2.13),(3.13), and (3.14) in steady state analysis.	34
Figure 3.3	Nanopositioning stage used in experimentation, Nano-OP65 nanopositioning stage coupled with a Nano-Drive controller from Mad City Labs Inc, with a primary resonance of 3 kHz. Position feedback is provided by a built-in capacitive sensor.	37
Figure 3.4	Measured hysteresis loops for the nanopositioner.	38
Figure 3.5	Plant output used in the identification of the modified PI operator, and resulting model output.	39

Figure 3.6	Model prediction and experimental data for a decreasing sinusoid used to optimize the hysteresis model.	39
Figure 3.7	Experimental results at 200 Hz for the proposed methods (SHSC and MHSC), ILC and PI+I.	42
Figure 3.8	Comparison between multi-harmonic servocompensator (MHSC) and Iterative Learning Control (ILC).	43
Figure 3.9	Frequency spectra of the tracking error signal for references at 5 Hz and 200 Hz. An SHSC was used in each case. Graphs are aligned so that the peaks on each graph correspond to the same harmonic of the reference. Note the prominence of the harmonics near 3000 Hz in the 200 Hz plot.	44
Figure 3.10	Experimental results at 50 Hz for sawtooth reference signal. Two periods are shown.	46
Figure 3.11	Experimental results for a reference trajectory of $y_r = 5 \sin(2\pi 5t - \pi/2) + 5 \sin(2\pi 15t + \pi/2) + 10 \sin(2\pi 25t - \pi/2)$	47
Figure 3.12	Tracking errors for a 50 Hz reference signal, for loaded and unloaded nanopositioner. An MHSC was used in both cases. Note the similarity in the time trajectory of the tracking error.	48
Figure 4.1	A sample curve showing how the time instants T_i and T_o are calculated for a play operator. The variable r is the radius of the play operator, and it is assumed that the input at time zero is $2r$	53
Figure 4.2	Reconstruction of the output $u(t)$ of a play operator. The play radius $r = 0.3$, and the time axis is shared by each signal.	54
Figure 4.3	Plot of c_n for increasing amplitude A . The play radius is held constant at $r = 0.5$	58
Figure 4.4	Plot of c_n for increasing play radius r . Values of c_n and r are normalized by the input amplitude A	59
Figure 4.5	Mean tracking errors for various controllers and play radii. Note that the controller gains and structure is unchanged by altering the play radius.	65
Figure 5.1	Tracking error for a 50 Hz reference signal, with two periods shown. Tracking range is $\pm 20 \mu\text{m}$	83

Figure 5.2	Tracking error for a 200 Hz reference signal with four periods shown. Tracking range is $\pm 20 \mu\text{m}$	83
Figure 5.3	Tracking error under a changing reference signal.	86
Figure 5.4	Trajectory of $\psi(1)$ under a changing reference signal.	86
Figure 5.5	Experimental results for adaptive servocompensator implemented with four adaptation variables. $\psi(1)$ and $\psi(3)$ are shown in the top plot. Notice the peaking events in the adaptation variables near 30 and 42 s. The lower plot shows the tracking error during the second peaking event. . . .	88
Figure 6.1	Block Diagram of the closed-loop system.	93
Figure 6.2	Phase portrait of average system for a sample plant and controller. The zero level curves of θ_1 (primarily vertical) and $\dot{\theta}_1$ (primarily horizontal) together with the neutral axis $\theta_1 = \theta_2$ are also plotted.	110
Figure 6.3	Illustration of linear plant preceded by hysteresis operator, commonly used to model piezoelectric-actuated nanopositioners.	110
Figure 6.4	Simulation results on the model of the piezoelectric plant. Two simulations are presented, with $R_{11} = 10$ and $R_{11} = 11$	115
Figure 6.5	Output spectrum for nanopositioner used in experimental studies. Input to power supply is $3 \sin(2\pi 5) + 4 V$. Primary harmonic is not shown, but has an amplitude of $25.2 \mu\text{m}$	115
Figure 6.6	Experimental results for a 5 Hz sinusoidal signal.	118
Figure 6.7	Experimental results for a 100 Hz sinusoidal signal.	118
Figure 6.8	Experimental Results for a 5 Hz sawtooth signal.	119
Figure 6.9	Phase portrait of σ_1 and σ_2 for various initial conditions. Desired equilibria are marked by the stars (red, in the lower right and top left), and initial conditions are marked by squares.	120
Figure 6.10	Plot of tracking error and adaptation variables vs. time. Adaptation is enabled at 2 s.	120

Figure 6.11	Phase portrait for experiments with $\sigma_1(0) = \sigma_2(0) = 2\pi 50$ and $\sigma_1(0) \neq \sigma_2(0)$ ($\sigma_1(0) = 2\pi 50$, $\sigma_2(0) = 2.01\pi 50$.)	121
Figure 7.1	Hysteresis loops for play operators with equalized relative gains, where r is equal to 0.7, and $\mu = 3$	139
Figure 7.2	Mean tracking error for controllers used in experimental trials. SHSC refers to compensation of only the reference harmonic, and MHSC refers to compensation of the first, second, and third harmonics of the reference.	144
Figure 7.3	Frequency spectrum of the tracking error with SHSC with and without inversion. Bump near 3 kHz is caused by the resonance peak of the nanopositioner.	145
Figure 8.1	Hysteresis state for systems that are unstable when the hysteresis is in the play region, with varying play radii.	150
Figure 8.2	Closed-loop system described in (8.5).	150
Figure 8.3	Illustration of the state of the play operator P_r during a sine-like limit cycle. The stars indicate times when the system dynamics switch.	153
Figure 8.4	Switching times computed from algorithm and simulation, versus gain k_p	165
Figure 8.5	Limit cycle solutions computed from algorithm and simulation, versus gain k_p	166
Figure 8.6	Peak amplitude of limit cycles versus absolute value of the limit cycle solutions α_0	167
Figure 8.7	True solution and Scaled solution for $r = 1$. Note the phase difference created by the different transient behavior.	168
Figure 8.8	True solution and Scaled solution for $r = 1$ at steady state, with phase offset included.	169
Figure 8.9	True solution and Scaled solution for $a = 10$ at steady state, with phase offset included.	169

Chapter 1

Introduction

1.1 Systems with Hysteresis

The phenomenon hysteresis is caused by the existence of multiple possible internal states within a system for a given input. This phenomenon was first observed by scientists in the fields of ferromagnetism [3] and plasticity [1] in the late 19th century, shown in Fig. 1.1. Mathematical models of hysteresis were first developed by Preisach [4] and Prandtl [5] in the early 20th century. Most research on hysteresis focused on modeling and characterization of physical hysteresis until the 1970's, when the mathematical theory of ordinary differential equations coupled with hysteresis operators was developed [6,7]. Recent advances in the field of materials science have created a new class of actuator/sensor hybrids called *Smart Materials* [8], whose behavior strongly exhibits hysteresis. A broad range of materials fall into this class, including piezoelectrics [9], shape memory alloys [10], electro-active polymers [11], magnetostrictives [12], magnetorheological fluids [13], and conjugated polymers [14]. Piezoelectric materials were the first of these smart materials to be developed, with the discovery of the piezoelectric coupling effect in the 1800's [9], and have been successively employed in a variety of industries including manufacturing, automotive, and medical devices [15].

Of particular importance to our work is the technology of nanopositioning, which deals with precision motion and manipulation on the nanometer scale. Nanopositioning plays a key role in technologies like Scanning Probe Microscopy (SPM), used in the advancement of fields such as

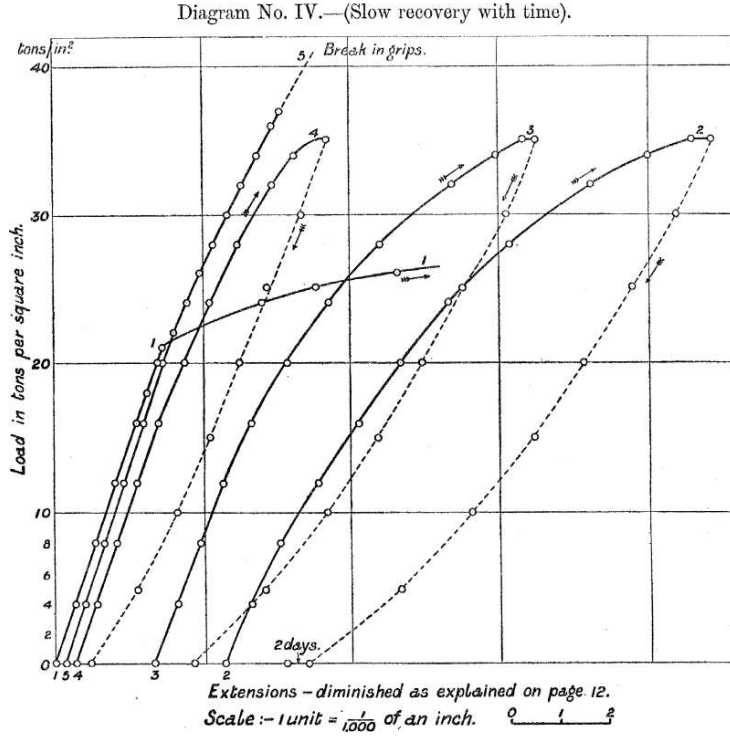


Figure 1.1: Plasticity hysteresis curves observed in [1].

biology [16], materials science [17], lithography [18], and others. The SPM process aims to generate a 3-dimensional mapping of a surface with nanometer resolution. One example of SPM is atomic force microscopy (AFM), illustrated in Fig. 1.2. An AFM probe rests on top of the sample to be mapped, suspended above the surface by atomic forces. A laser is directed down onto the AFM probe, which reflects off the probe onto an optical detector. The sample is then moved beneath the AFM probe, which causes the probe to move up and down. This motion is detected by the optical detector, and is used together with position tracking of the sample to form the 3-dimensional mapping. The primary performance metrics in AFM are the imaging accuracy and the imaging speed [2]. The technologies behind AFM probes and optical detectors are fairly mature, and therefore the limiting factor in both of these metrics is the effective bandwidth of the positioning system. The most effective actuators for such problems are piezoelectric nanopositioners, which are capable of high speed and precision, but are difficult to control due to the effect of

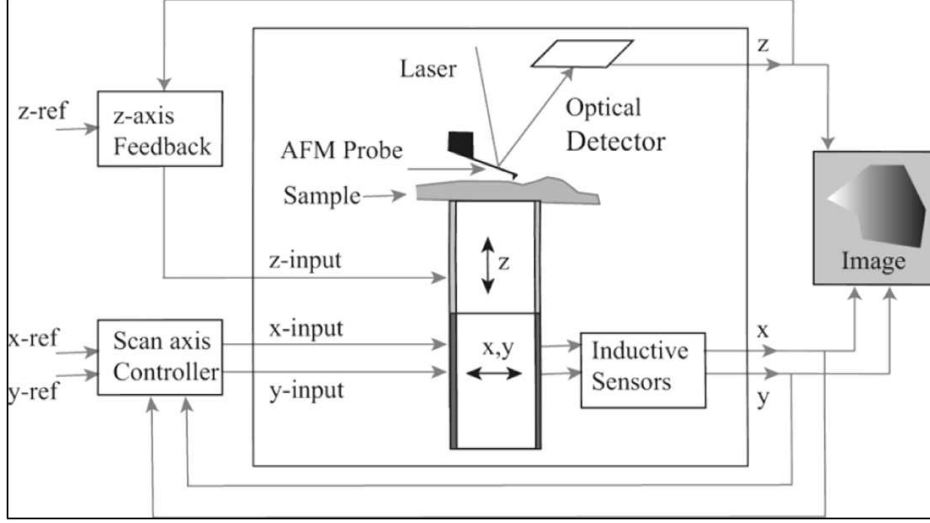


Figure 1.2: Illustration of Atomic Force Microscopy from [2].

hysteresis.

The promising applications of smart materials have motivated efforts to better understand and control their behavior, which has ignited further research into systems with hysteresis. When modeling the behavior of smart materials, it is important to distinguish between sensing and actuation models. Modeling conducted for sensing applications typically focuses on the internal dynamics of the smart materials, and are often based on the physics and chemistry of the materials [19–21]. In modeling the actuation behavior of smart materials, a more phenomenological or “Black box” approach can be taken. A common and faithful model for smart material actuators consists of a linear system preceded by a hysteresis operator [11, 22–26]:

$$\begin{aligned}\dot{x}(t) &= Ax(t) + Bu(t) \\ u(t) &= \Gamma[v; \Gamma_0](t)\end{aligned}\tag{1.1}$$

where $v(t)$ is the system input, and Γ is a hysteresis operator [7, 27–29]. It is also worth noting that there are significant uncertainties in both the hysteresis and dynamics of the system, as the

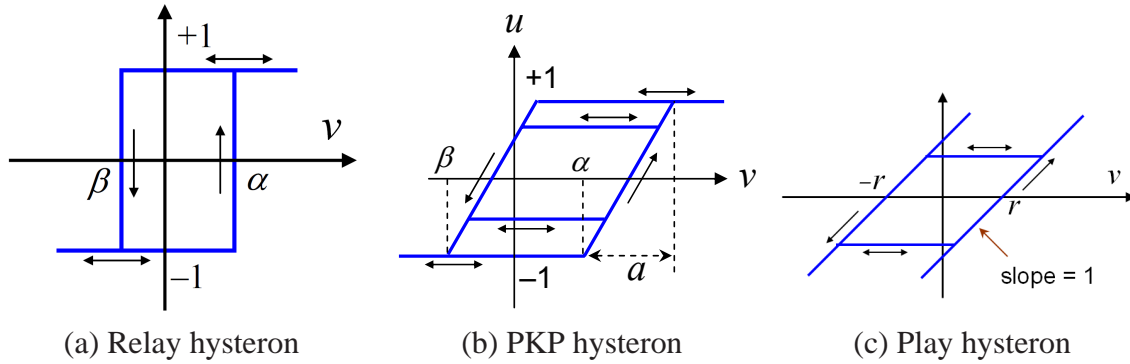


Figure 1.3: Hysteresons of several Preisach-like operators. For interpretation of the references to color in this and all other figures, the reader is referred to the electronic version of this dissertation.

behavior of the system varies with environmental and loading conditions [2]. We will refer to this combination of a linear dynamic system and hysteresis operator as a *system with hysteresis*. Clearly, in order to control the actuation of smart materials, we must investigate such systems with hysteresis.

The first step in our investigation is to identify the system model (1.1) to be considered. As there are a wealth of tools available for capturing linear dynamics, most research into the modeling of systems with hysteresis is focused on characterization and identification of the hysteresis operator. The oldest and most widely used is the Preisach model [4], developed in the 1930's as a model for magnetic hysteresis. Preisach models are formed through a weighted superposition of relay *hysteresons* (shown in Fig. 1.3a), unit hysteresis elements whose parameters are varied to approximate a wide variety of physical hysteresis phenomena [8, 28]. The Preisach model has also proven to be an excellent model for smart material actuators [25, 30, 31]. As the effectiveness of the operator itself is fairly established, most recent works have focused on identification or implementation of the Preisach operator [12, 23].

The success and maturity of the Preisach model has resulted in the development of a number of "Preisach-like" operators [22], which use hysteresons modified from the original Preisach model.

The Preisach-Krasnosel'skii-Pokrovskii (PKP) operator [24, 29] is formed with PKP hysterons (Fig. 1.3b), which are similar to the relay hysteron but incorporate finite slopes. In our work, we will focus on the Prandtl-Ishlinskii (PI) operator [5], which uses play operators as hysterons (Fig. 1.3c), in reference to the phenomenon of mechanical play they emulate. We will also make use of the modified PI operator [32], which consists of a PI operator cascaded with dead-zone operators. As we will see in Chapter 2, the PI operator and its generalization possesses several practical advantages over other Preisach-like operators that make it well suited for online control applications.

1.2 Control of Systems with Hysteresis: Existing work

Once we have arrived at a faithful model for a system with hysteresis, we can then address the problem of controller design for such systems. A common control objective for any actuator is to force the trajectory of the system to track a desired reference. This is also the case in nanopositioning applications like SPM, where the positioner output is intended to track a prescribed path. A multitude of control strategies have been proposed to solve such tracking problems in systems with hysteresis [33–39]. As with modeling systems with hysteresis, the meritorious element of these controllers is the manner in which they address the effect of hysteresis within the system. For most of these controller designs, we can differentiate between their philosophies as being either inversion-focused or rejection-focused. The differences between these control techniques are often closely tied to the system model considered by the authors.

1.2.1 Inversion-Focused Methods

One of the most natural and widespread approaches in control theory is the technique of model inversion. The objective of model inversion is to design a controller to reduce the input-output map of a system to a unity gain. Following the development of hysteresis models, researchers began to develop inverse hysteresis operators for use in control applications. Inversion strategies for the Preisach operator have been developed [23, 31, 40]; however, these result in only approximate inversions. The PI operator on the other hand possesses a closed-form inversion [32], which turns out to be another PI operator. For both models, hysteresis inversion has proven to be a very effective technique for reducing the impact of hysteresis, and it is commonly used in the control of systems with hysteresis [12, 22, 23, 33, 34, 40–42].

Inversion-focused control algorithms center around improving or optimizing a hysteresis inversion, often through online adaptation of the weights of a Preisach-like operator. This approach was first detailed in [33], where an adaptive inverse approach based on a generic hysteresis model and model reference adaptive control (MRAC) was proposed. An obstacle to this design is that classical MRAC approaches, such as those described in [43], lead to bilinear coupling of adaptation terms. Such bilinear coupling impedes the design of adaptation laws unless one of the coupled terms is a scalar [43]. This was addressed in [33] through over-parameterization of the adaptation variables. In [41], slow adaptation was utilized in an MRAC scheme to separate adaptation of the hysteresis parameters from the controller parameters. An adaptive sliding mode approach coupled with adaptive hysteresis inversion was used in [44] for discrete-time systems with hysteresis. In addition, neural networks have been used to invert hysteresis and compensate for uncertain dynamics [45].

A noteworthy disadvantage of these methods is that the high numbers of hysterons required by

Presiach-like operators makes these adaptive approaches computationally expensive. For example, 55 hysterons were used to describe the hysteresis behavior of a magnetostrictive material in [35], which, if used in an inversion-focused control strategy, would require implementation of 55 on-line adaptation laws. In addition, implementation of the inversion itself can be computationally expensive, a fact that we will observe in Chapter 7. These computational concerns have motivated efforts to implement hysteresis inversions using an FPGA [46]; however, this adds another level of complexity to the design and analysis of the system.

1.2.2 Rejection-Focused Methods

An alternate way of thinking, as opposed to the inversion-focused approach, is to consider the undesirable effects of hysteresis as an uncertain disturbance to be rejected. The hysteresis effect is broken into a known gain and an uncertain disturbance, and the controller is then designed to be robust to the uncertainty. This technique is especially popular in the nan positioning literature, where the high performance demands of SPM systems require controllers capable of tracking and disturbance attenuation. H_∞ control [37] and 2-degree of freedom control [47] have been shown to provide robustness to plant uncertainty and facilitate tracking in the presence of hysteresis. A similar approach was used in [48], where a high gain and notch filter feedback controller is combined with a feedforward dynamic inversion. In the work of [49], the hysteresis effect was modeled by a combination of a linear gain and unstructured exogenous disturbance, which is attenuated by an adaptive robust controller. Sliding mode control [39] and disturbance observers [50, 51] have also been used to compensate for the effect of hysteresis.

The stability proofs in these papers are carried out using the ubiquitous Lyapunov criterion. However, by assuming the hysteresis to be an unstructured disturbance, these methods ignore the operator behavior of the hysteresis, and therefore can only prove ultimate boundedness of the

states. Indeed, later in this dissertation we will also show that using such design methods can cause the controller to send the system into a self-excited limit cycle. In addition, the theoretical bounds on the tracking error can be very conservative, a fact that has motivated efforts to improve the accuracy of the model bounds [52].

1.3 The Multi-Harmonic Servocompensator: Union of Design Philosophies

As we have discussed, inversion-focused and rejection-focused methods are fundamentally opposed in the mindset behind their designs. Inversion-focused methods use detailed modeling of the hysteresis phenomenon in order to achieve robust performance, but suffer from the resulting controller complexity. Rejection-focused methods utilize the might of control theory to attenuate the effect of hysteresis, without explicitly utilizing knowledge of the phenomenon itself in the controller design. In a union of these philosophies, we will explore the use of *servocompensators* in systems with hysteresis. We will see that the design of this servocompensator makes specific use of the effect of hysteresis in the closed-loop system to formulate a *simple, robust, and high-performance* controller for systems with hysteresis.

Servocompensators, also referred to as internal-model controllers, were originally designed in the 1970's by Davison [53, 54] and Francis [55, 56]. The defining feature of servocompensators is their ability to completely cancel signals contained within the design class of their internal models. This property is also shown to be robust to perturbations from both exogenous inputs and model uncertainties, as long as the system is not destabilized. This makes servocompensators excellent choices for solving tracking problems. Isidori and Byrnes [57] extended the internal model approach to nonlinear systems; however, the class of nonlinear systems considered does not

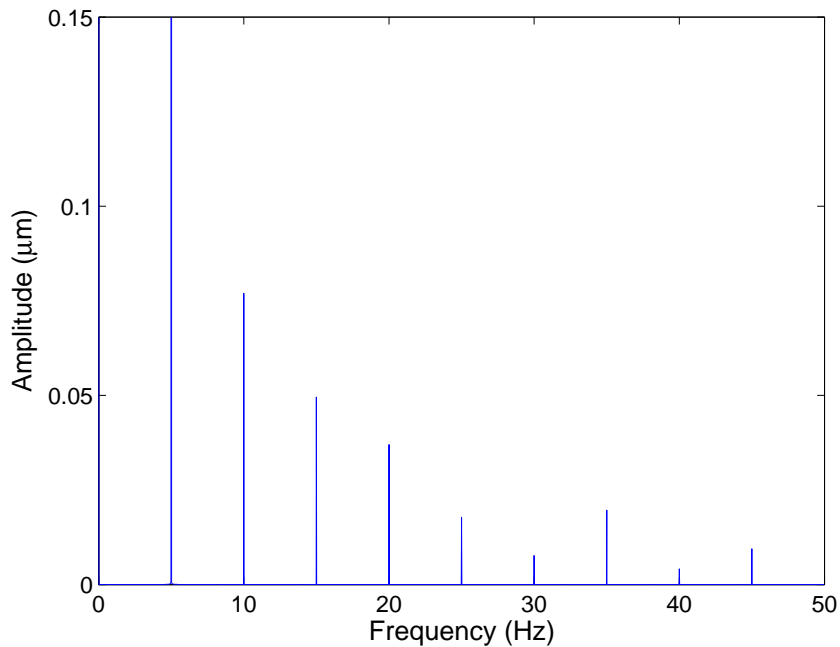


Figure 1.4: Amplitude spectra of the output of an example hysteresis for a sinusoidal input. Primary harmonic (5 Hz) is larger than pictured.

consider the memory behavior observed in systems with hysteresis.

An important aspect of hysteresis operators is that for periodic inputs, the output of the operator can be expressed as a Fourier series, as shown in Fig. 1.4 for a sinusoidal input. The addition of hysteresis causes harmonics of the input to appear in the output, which quickly diminish in size with increasing frequency. In addition, hysteresis will also alter the amplitude and phase of the primary harmonic. We can utilize this knowledge to design a servocompensator incorporating internal models for the input signal along with additional harmonics to achieve precise and robust tracking performance, by canceling the majority of the hysteresis effect. We will refer to such a controller as a *multi-harmonic servocompensator* (MHSC).

1.4 Overview of Contributions

The principle contribution of this work lies in addressing the tracking problem for systems with hysteresis using servocompensators, which we approach in several ways. We first discuss the design and analysis of a servocompensator for solving tracking problems in systems with hysteresis, which we validate experimentally through implementation on a commercial nanopositioning stage. A crucial element of this analysis is that we utilize a modified PI operator to model the hysteresis in the system. This operator possesses an important contraction property, which, coupled with an approximate hysteresis inversion, allows us to prove the existence of a unique, asymptotically stable, periodic solution. We can then invoke the disturbance rejection properties of the servocompensator to prove the attenuation of hysteresis at steady state, assuming that the internal model of the desired reference trajectory is known. Our experimental results will confirm the rejection properties of the controller, where we show our proposed method can achieve one third of the mean tracking error of a competitive technique in nanopositioning (Iterative Learning Control).

We then present results on a tool for computing the output of a hysteresis operator are presented, based on Fourier series theory. This algorithm first formulates the output of individual hysterons as a series of pulse signals in combination with the input, which facilitate evaluation of the Fourier integrals. Then, by assuming either a sinusoidal or sawtooth input signal, we will show that the Fourier coefficients can be computed in a closed form manner. We then present simulation results on this method, and show that the algorithm represents a valuable design tool for servocompensators in systems with hysteresis.

Next, we will extend the design of the MHSC to cases where the internal model of the reference is not known *a priori*. We first adapt a traditionally designed nonlinear adaptive servocompensator, and prove its stability in systems with hysteresis. This approach combines high-gain stabilizing

control with a canonical internal model controller that is subject to adaptation. During our discussion of the experimental results, we will discover that this design cannot incorporate the principles of the multi-harmonic servocompensator to reduce the effect of hysteresis. We will then discuss the inclusion of a frequency estimator based on slow adaptation into the MHSC, a design which we refer to as an *indirect adaptive servocompensator* (IASC). In this discussion, the term frequency will refer to the fundamental frequency of a periodic signal. For example, a sinusoid, a triangular wave, or a square wave will all be described as having one frequency although the latter two clearly have harmonic frequency components. However, these harmonics are known multiples of the fundamental frequency; therefore knowledge of the fundamental frequency implies knowledge of the remaining harmonic components. Through our stability analysis, we will analytically demonstrate some noteworthy properties for systems with one, two, and n unknown frequencies. In particular, for systems with one unknown frequency, we will prove and verify a stability condition related to the amplitude of the reference signal as compared to disturbances, and for the case of two unknown frequencies, prove the existence of a degenerate case for the system. We will then prove the stability of such controllers in a system with hysteresis, and demonstrate its performance experimentally.

Next, we discuss the stability and tracking error convergence of a system with hysteresis using a general feedback controller with an integral action. The theory of switched systems, in particular, that of the common Lyapunov function [58], and a linear matrix inequality (LMI) will be used to prove that the tracking error and state vector exponentially converge to zero for a constant reference. The principal contribution of this work is to present sufficient conditions (in the form of an LMI) for the regulation of the closed-loop system in terms of the hysteresis parameters, without requiring the hysteresis to be small. This addresses a key weakness of our prior results, namely the requirement that hysteresis inversion be included in the controller design in order to prove stability. As we will see, the presence of an integral action is crucial to the formulation of

our LMI condition. This then allows us to show the stability of systems with hysteresis controlled by servocompensators without requiring hysteresis inversion. We then show that the MHSC can achieve even higher performance without hysteresis inversion than when hysteresis inversion is used; in particular, the mean tracking error achieved by the MHSC is cut in half when hysteresis inversion is removed.

Finally, inspired by discoveries made during the course of the LMI work, we investigate self-excited limit cycles occurring in a particular class of systems with hysteresis. In particular, we will focus on a linear plant controlled by an integral controller, where a play operator [32] is present in the feedback loop. We focus our attention on odd symmetric limit cycles within the system. A Newton-Raphson algorithm is formulated to calculate the limit cycles, and using the odd symmetry, we are then able to prove that there exist linear relationships between several properties of the limit cycles and the parameters of the system. These results are verified in simulation, where we also demonstrate the effectiveness of the Newton-Raphson algorithm at predicting the solutions of the system. We will also illustrate a crucial weakness of rejection-focused designs, in that even for constant references, the steady-state trajectory may be a self-excited limit cycle.

The dissertation is organized as follows. Chapter 2 provides background information on the hysteresis models used in this work. We also derive some important expressions used in the analysis of the closed-loop systems with hysteresis in the following Chapters. Chapter 3 presents the design and analysis of our proposed MHSC in systems with hysteresis, as well as experimental comparisons to established control methods. Our Fourier series algorithm is contained in Chapter 4. We investigate the application of a traditional adaptive servocompensator to nanopositioning control in Chapter 5, which also motivates the design of our novel adaptive servocompensator. Chapter 6 discusses the design, analysis, and experimental validation of the proposed IASC. The LMI results proving stability of our controller without using hysteresis inversion are contained in

Chapter 7. Our limit cycle investigation is contained in Chapter 8. Finally, we provide concluding remarks and discuss potential future work in Chapter 9.

Chapter 2

Overview of Hysteresis Models

2.1 Introduction

As we have discussed in Chapter 1, the primary challenge in modeling of systems with hysteresis is the formulation of the hysteresis operator. A complete review of hysteresis modeling is outside the scope of this dissertation; we instead direct the reader to the monographs [7, 28, 29] for such an overview. We will instead focus on the operators used within this thesis; the Prandtl-Ishlinskii (PI) operator, modified Prandtl-Ishlinskii (modified PI) operator, and the Preisach-Krasnosel'skii-Pokrovskii (PKP) operator. Each operator falls under the umbrella of “Preisach-Like” operators described in Section 1.2, in that each is formed by a weighted superposition of unit hysteresis elements called hysterons. We will begin the discussion of each hysteresis operator by presenting the details of its hysteron, followed by the formulation of the operator itself. In addition, we will also discuss inversion of the PI and modified PI operators, and characterize the inversion error when the inversion is inexact.

2.2 The Prandtl-Ishlinskii Operator

The PI operator has seen widespread use in modeling piezoelectric hysteresis [26, 32, 44, 59]. In this dissertation, we will focus on the PI operator because it possesses a variety of important mathematical properties which are useful to control designers. First, the PI operator possesses an

exact, closed form inversion, which makes the operator an excellent choice for control designers interested in online implementation. Second, it possesses a contraction property which, as we will see, can be utilized in the stability proofs of several closed-loop systems considered in this thesis.

The hysteron of the PI operator is the play operator, illustrated in Fig. 2.1. The play operator is characterized by a single parameter r_i , which we refer to as the play radius. For a monotone continuous input $v(t)$, we denote the output and state of a play operator with radius r_i as

$$P_{r_i}[v; P_{r_i}[v](0)](t) = \max\{\min\{v(t) + r_i, P_{r_i}[v](0)\}, v(t) - r_i\} \quad (2.1)$$

By breaking any arbitrary input into monotone segments and replacing $P_{r_i}[v](0)$ by $P_{r_i}[v](t_i)$, where the monotonicity of $v(t)$ changes at $v(t_i)$, the state $P_{r_i}[v](t)$ can be defined for arbitrary inputs.

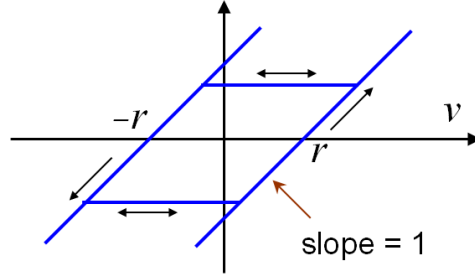


Figure 2.1: Illustration of a Play Operator. r is the play radius.

Now define the vectors $r = [r_0, r_1, \dots, r_p]'$ and $\theta_h = [\theta_{h0}, \theta_{h1}, \dots, \theta_{hp}]'$, where $'$ denotes the transpose. The PI operator, which we will denote as Γ_h , is written as

$$\Gamma_h[v; W(0)](t) = \sum_{i=0}^p \theta_{hi} P_{r_i}[v; P_{r_i}(0)](t) \quad (2.2)$$

where we let the vector $W(t) = [W_0(t), W_1(t), \dots, W_p(t)]'$ represent the states of the play operators

(i.e. $W_i(t) = P_{r_i}[v; P_{r_i}(0)](t)$). We can also write Γ_h in the inner product form

$$\Gamma_h[v; W(0)](t) = \theta'_h W(t) \quad (2.3)$$

For later use, we will also define the operator \mathcal{P} , which captures the evolution of $W(t)$ under the input $v(t)$;

$$W(t) = \mathcal{P}[v; W(0)](t) \quad (2.4)$$

Remark 1 *The PI operator described in Eqs. (2.2)-(2.4) is also referred to as a finite-element PI operator. A more accurate description of hysteresis can be achieved by using an infinite-element PI operator [32, 44]. However, in the interest of practical application, the finite-element PI operator is often used in controller design. Therefore, we focus on the finite-element PI operator in this thesis.*

We now discuss the inversion of the PI operator Γ_h . Specifically, we will discuss the formulation of the left inverse of the PI operator Γ_h , which we will define as Γ_h^{-1} . This inverse operator is also a PI operator, with different weights and initial conditions. Let \bar{r} and $\bar{\theta}_h$ denote the radius and weights of the play operators of the inverse operator. Then we can write the inverse operator, with input $u_d(t)$, as

$$\Gamma_h^{-1}[u_d; \bar{W}(0)](t) = \sum_{i=0}^p \bar{\theta}_{hi} P_{\bar{r}_i}[u_d; P_{\bar{r}_i}(0)](t) \quad (2.5)$$

where we have denoted the state of the play operators in Γ_h^{-1} with the vector

$$\bar{W}(t) = [\bar{W}_0(t), \bar{W}_1(t), \dots, \bar{W}_p(t)]$$

The inverse parameters \bar{r} , $\bar{\theta}_h$, and $\bar{W}(0)$ can be calculated from the following equations, presented

in [32]:

$$\bar{r}_i = \sum_{j=0}^i \theta_{hj}(r_j - r_i), \quad i = 0, 1, \dots, p \quad (2.6)$$

$$\bar{\theta}_{h0} = 1/\theta_{h0} \quad (2.7)$$

$$\bar{\theta}_{hi} = -\frac{\theta_{hi}}{\left(\theta_{h0} + \sum_{j=1}^i \theta_{hj}\right) \left(\theta_{h0} + \sum_{j=1}^{i-1} \theta_{hj}\right)}, \quad i = 1, \dots, p \quad (2.8)$$

$$\bar{W}_i(0) = \sum_{j=0}^i \theta_{hj}W_j(0) + \sum_{j=i+1}^p \theta_{hj}W_j(0), \quad i = 0, 1, \dots, p \quad (2.9)$$

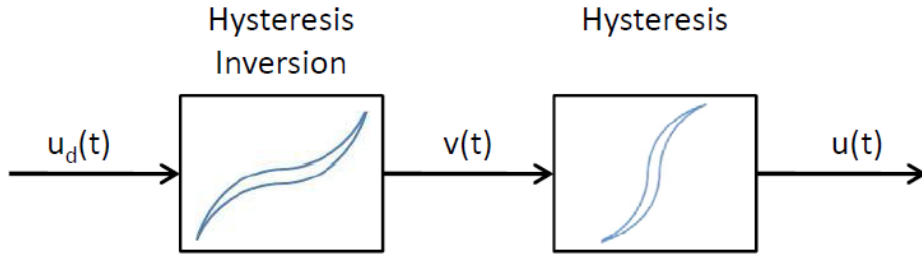


Figure 2.2: The inversion process for hysteresis operators. u_d is the desired output, and u is the actual output.

The inversion process is illustrated in Fig. 2.2. The inversion input $u_d(t)$ is the desired output of the hysteresis operator, and is designed to accomplish some larger control objective, such as tracking or stabilization via state feedback. As the hysteresis operator is modeled as part of the plant itself, $v(t)$ is the input to the hysteretic system. The signal $u(t)$ is the output of the modeled hysteresis operator in the plant, and therefore is not measurable or available for use in the controller. However, its definition is very useful in analysis of the system.

The inverse operator Γ_h^{-1} is an exact inversion, implying that the difference between u and u_d is identically zero. However, in practical circumstances the forward hysteresis operator Γ_h is not exactly known. Rather, only an estimate $\hat{\Gamma}_h$, with weights $\hat{\theta}_h$ and radii \hat{r} , is available for control

design. In our work, we will operate under the following assumption.

Assumption 1 *The uncertainty between the models Γ_h and $\hat{\Gamma}_h$ is limited to the weights $\hat{\theta}_h$ and θ_h .*

This implies that $\hat{r} = r$ is known.

This assumption is commonly used by designers working with the PI model [32], as the radii are chosen to span the available input range of the actuator, and the order of the model is chosen based on computational concerns. This approximate model and its parameters are used to create the approximate inversion, $\hat{\Gamma}_h^{-1}$, whose weights and radii are $\bar{\theta}_h$ and \bar{r} . We will now replace the ideal inversion Γ_h^{-1} with this approximate inversion. With the input of u_d and output of v , the approximate inversion obeys the equation

$$v(t) = \hat{\Gamma}_h^{-1}[u_d; \bar{W}(0)](t) = \sum_{i=0}^p \bar{\theta}_{hi} P_{\bar{r}_i}[u_d; P_{\bar{r}_i}(0)](t) \quad (2.10)$$

We will now characterize the inversion error $u(t) - u_d(t)$ when an approximate inversion is used. $u(t)$ is still described by (2.3). Since the PI operator's inversion is exact, we can use (2.10) to write $u_d(t)$ as

$$\begin{aligned} u_d(t) &= \hat{\Gamma}_h [\hat{\Gamma}_h^{-1}[u_d; \bar{W}(0)]; W(0)](t) \\ &= \hat{\Gamma}_h[v; W(0)](t) \triangleq \hat{\theta}'_h W(t) \end{aligned} \quad (2.11)$$

Using (2.3) and (2.11), we can then write

$$u_d(t) - u(t) = \hat{\theta}'_h W(t) - \theta'_h W(t) \triangleq \tilde{\theta}'_h W(t) \quad (2.12)$$

where $W(t)$ is defined by composite hysteresis operator

$$W(t) = \mathcal{W}[u_d; W(0)](t) \triangleq \mathcal{P} \circ \hat{\Gamma}_h^{-1}[u_d; W(0)](t) \quad (2.13)$$

2.3 Modified Prandtl-Ishlinskii Operator

A disadvantage of the PI operator is that it is odd symmetric, which can be seen from the illustration of the play operator in Fig. 2.1. This is a significant disadvantage, as the hysteresis loops exhibited by smart material systems are often asymmetric. In [32], a modified PI operator was proposed to address this deficiency. This model combines the original PI operator with a superposition of one-sided deadzone functions, illustrated in Fig 2.3. Each deadzone function is parameterized by a single threshold parameter, written as z in Fig. 2.3. The output a deadzone function d_{z_i} , where z_i is the threshold, can be expressed as

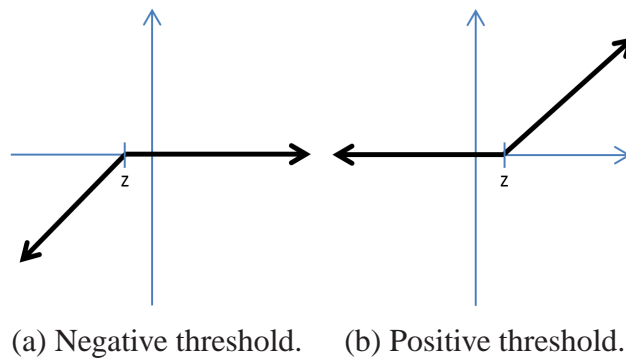


Figure 2.3: Deadzone functions with positive and negative thresholds. The slopes in linear regions are unity.

$$d_{z_i}(v(t)) = \begin{cases} \max(v(t) - z_i, 0), & z_i > 0 \\ v(t), & z_i = 0 \\ \min(v(t) - z_i, 0), & z_i < 0 \end{cases} \quad (2.14)$$

Note that if $z_i = 0$, the deadzone function becomes a unity gain. Now denote the vector of deadzone thresholds $z = [z_{-l}, \dots, z_{-1}, z_0, z_1, \dots, z_l]'$, where

$$-\infty < z_{-l} < \dots < z_{-1} < z_0 = 0 < z_1 < \dots < z_l < \infty$$

We will also denote the weight vector $\theta_d = [\theta_{d_{-l}}, \dots, \theta_{d_{-1}}, \theta_{d_0}, \theta_{d_1}, \dots, \theta_{d_l}]'$. We can now denote the superposition of deadzone functions as Φ , with input $v_1(t)$ as

$$\Phi(v_1(t)) = \sum_{i=-l}^l \theta_{d_i} d_{z_i}(v_1(t)) \triangleq \theta_d' D_z(v_1(t)) \quad (2.15)$$

where the vector $D_z(v(t)) = [d_{z_{-l}}(v(t)), \dots, d_{z_l}(v(t))]'$ denotes a stack of deadzone functions with thresholds z . Using (2.15) along with (2.3), we can define the modified PI operator, denoted as Γ_{hd} . With input $v(t)$, the operator can be written as

$$\Gamma_{hd}[v; W(0)](t) = \Phi(\Gamma_h[v; W(0)](t)) = \theta_d' D_z(\theta_h' W(t)) \quad (2.16)$$

As the deadzone operator is simply a collection of functions, a closed form inversion also exists for the deadzone operator. This inversion is also a deadzone operator, with modified weights and thresholds. For deadzone functions with positive thresholds, the inversion parameters $\bar{\theta}_d$ and \bar{z} can

be computed as

$$\bar{z}_i = \sum_{j=0}^i \theta_{dj}(z_j - z_i), \quad i = 0, \dots, l \quad (2.17)$$

$$\bar{\theta}_{d0} = 1/\theta_{d0} \quad (2.18)$$

$$\bar{\theta}_{di} = -\frac{\theta_{di}}{\left(\theta_{d0} + \sum_{j=1}^i \theta_{dj}\right) \left(\theta_{d0} + \sum_{j=1}^{i-1} \theta_{dj}\right)}, \quad i = 1, \dots, l \quad (2.19)$$

and for negative thresholds,

$$\bar{z}_i = \sum_{j=i}^0 \theta_{dj}(z_j - z_i), \quad i = -l, \dots, 0 \quad (2.20)$$

$$\bar{\theta}_{d0} = 1/\theta_{d0} \quad (2.21)$$

$$\bar{\theta}_i = -\frac{\theta_{di}}{\left(\theta_{d0} + \sum_{j=i}^{-1} \theta_{dj}\right) \left(\theta_{d0} + \sum_{j=i+1}^{-1} \theta_{dj}\right)}, \quad i = -l, \dots, 0 \quad (2.22)$$

Using these definitions, we can form the inverse of the modified PI operator as

$$\Gamma_{hd}^{-1}[u_d; W(0)](t) = \Gamma_h^{-1}[\bar{\theta}'_d D_{\bar{z}}(u_d); \bar{W}(0)](t) \quad (2.23)$$

Note that the order of the PI and deadzone operators are switched in the inverse operator with respect to the forward operator. We have already discussed how the hysteresis models are unknown in practical applications. Therefore, we must consider an inexact hysteresis inversion, based on an approximation of Γ_{hd} , which we denote as $\hat{\Gamma}_{hd}$.

Assumption 2 *The uncertainty between the models Γ_{hd} and $\hat{\Gamma}_{hd}$ are limited to the hysteresis weights $\hat{\theta}_h$ and θ_h , and the deadzone weights $\hat{\theta}_d$ and θ_d . This implies that the vectors r and z are known.*

This is a similar condition to that imposed for the PI operator in Assumption 1, and it is made for similar reasons. We will denote this estimate and its output $u(t)$ as

$$u(t) = \hat{\Gamma}_{hd}[v; W(0)](t) = \hat{\Phi}(\hat{\Gamma}_h[v; W(0)](t)) = \hat{\theta}'_d D_z(\hat{\theta}'_h W(t)) \quad (2.24)$$

We can then use the approximated model to derive an approximate inversion,

$$\hat{\Gamma}_{hd}^{-1}[u_d; \bar{W}(0)](t) = \hat{\Gamma}_h^{-1}[\tilde{\theta}'_d D_{\bar{z}}(u_d); \bar{W}(0)](t) \quad (2.25)$$

Our final discussion regarding the modified PI operator considers the inversion error, where we attempt to derive a similar expression for the inversion error as that achieved for the PI operator in (2.12). Using the identity $u_d(t) = \hat{\Gamma}_{hd}[\hat{\Gamma}_{hd}^{-1}[u_d; \bar{W}(0)]; W(0)]$ and (2.24), the inversion error $u(t) - u_d(t)$ can be expressed as

$$u_d(t) - u(t) = \hat{\theta}'_d D_z(\hat{\theta}'_h W(t)) - \theta'_d D_z(\theta'_h W(t)) \quad (2.26)$$

where $W(t)$ is defined by the composite hysteresis operator

$$W(t) = \mathcal{W}_d[u_d; W(0)](t) \triangleq \mathcal{P} \circ \hat{\Gamma}_{hd}^{-1}[u_d; W(0)](t) \quad (2.27)$$

We will now derive a bound for this inversion related to the parameter errors, which we define as $\tilde{\theta}_d = \hat{\theta}_d - \theta_d$ and $\tilde{\theta}_h$, defined in (2.12). Adding and subtracting $\hat{\theta}'_d D_z(\theta'_h W(t))$ to (2.26) allows us

to arrive at

$$\begin{aligned}
u_d(t) - u(t) &= \hat{\theta}'_d D_z(\hat{\theta}'_h W(t)) - \theta'_d D_z(\theta'_h W(t)) + \hat{\theta}'_d D_z(\theta'_h W(t)) - \hat{\theta}'_d D_z(\theta'_h W(t)) \\
&= (\hat{\theta}'_d - \theta'_d) D_z(\theta'_h W(t)) + \hat{\theta}'_d [D_z(\hat{\theta}'_h W(t)) - D_z(\theta'_h W(t))]
\end{aligned} \tag{2.28}$$

It can be easily seen from (2.14) that the dead-zone operator obeys the Lipschitz condition

$$|d_{z_i}(a) - d_{z_i}(b)| \leq |a - b| \tag{2.29}$$

for any threshold z_i . Using this property together with the holder inequality, and taking the absolute value of (2.28), we have

$$\begin{aligned}
|u - u_d| &\leq \|\tilde{\theta}_d\| \|D_z(\theta'_h W(t))\| + \|\hat{\theta}_d\|_\infty [(2l + 1) \|\tilde{\theta}'_h W(t)\|] \\
&\leq \|\tilde{\theta}_d\| \|D_z(\theta'_h W(t))\| + \|\hat{\theta}_d\|_\infty [(2l + 1) \|\tilde{\theta}_h\| \|W(t)\|] \\
&\leq \varepsilon_d [\|D_z(\theta'_h W(t))\| + (2l + 1) \|\hat{\theta}_d\|_\infty \|W(t)\|]
\end{aligned} \tag{2.30}$$

where $\varepsilon_d = \max(\|\tilde{\theta}_h\|, \|\tilde{\theta}_d\|)$ and $\|\cdot\|_\infty$ represents the infinity norm [60].

2.4 The Preisach-Krasnosel'skii-Pokrovskii Operator

The final hysteresis operator we will address is the Preisach-Krasnosel'skii-Pokrovskii, or PKP operator [24, 29, 61]. We will not be utilizing this model in any experiments, and therefore we will not be discussing the inversion of this operator. The PKP hysteron is defined by three parameters, labeled in Fig. 2.4 as α , β , and a . This hysteron is very similar to the Preisach hysteron (the relay operator); however, the inclusion of the slope parameter a allows for a continuous output with a

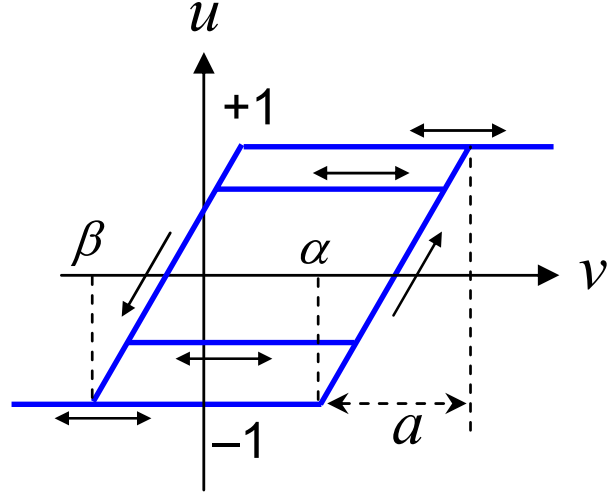


Figure 2.4: Illustration of the PKP hysteron. This operator is parameterized by the thresholds α , β , and slope a .

finite number of hysterons. The selections of α and β allow the operator to model hysteresis curves of complex shapes. For a monotone continuous input $v(t)$, the output of the PKP hysteron can be described by

$$u(t) = \begin{cases} \min(\max\{v(0), -1 + \frac{2(v(t)-\alpha)}{a}, -1\}, 1) & \text{for } \dot{v} \geq 0 \\ \max(\min\{v(0), -1 + \frac{2(v(t)-\beta)}{a}, -1\}, -1) & \text{for } \dot{v} \leq 0 \end{cases} \quad (2.31)$$

As with the play operator, the output of a PKP hysteron for general inputs can be formed by breaking the input into a series of monotone signals. Now denote the ordered triple $\xi_i = (\alpha_i, \beta_i, a_i)$, and let Ω_{ξ_i} denote the output of a PKP operator with parameters ξ_i . The PKP operator, which we will call Γ_p , can then be formed as

$$\Gamma_p[v, \Omega(0)] = \sum_{i=0}^p \theta_{p_i} \Omega_{\xi_i}[v(t), \Omega_{\xi_i}(0)] \quad (2.32)$$

Chapter 3

Attenuation of Hysteresis through Servocompensators

3.1 Introduction

In this Chapter, we will discuss the theory behind the implementation of servocompensators for use in tracking problems in systems with hysteresis. We begin with a discussion of servocompensator design for uncertain linear plants, where we will use a robust Riccati equation approach to ensure robustness of the system. Next, we prove the existence and asymptotic stability of a unique periodic solution when a robust servocompensator and hysteresis inversion are used in a system with hysteresis, where the hysteresis is modeled by a PI or modified PI operator. Since the solutions of the system are periodic, we can interpret the effect of hysteresis at steady state as a structured, periodic, exogenous disturbance, which can be compensated by the servocompensator. In particular, we will show that the tracking error can be made arbitrarily small by increasing the order of the servocompensator. We will then demonstrate the merit of this control design through experiments conducted on a commercial nanopositioner, and show the performance of the proposed controller is superior to other commonly used methods in nanopositioning control. We also demonstrate the robustness of this technique to changing load conditions.

3.2 Servocompensator Design for Uncertain Systems

Recalling Fig. 2.2, we recognize that the input to the inverse operator u_d is typically designed for larger control objectives. Motivated by this, we will design our servocompensator to regulate the output of an uncertain linear plant, and subsequently adjust its design to improve the controllers performance in systems with hysteresis. Consider a linear system

$$\begin{aligned}\dot{x}(t) &= Ax(t) + Bu(t) + Ew(t) \\ e(t) &= y_r(t) - Cx(t) - Du(t)\end{aligned}\tag{3.1}$$

where $x \in \mathbb{R}^n$ is the plant state, $u \in \mathbb{R}$ is the plant input, $y = Cx + Du$ is the plant output, $e \in \mathbb{R}$ is the tracking error, $w(t) = H\sigma(t) \in \mathbb{R}^{m \times 1}$ is considered an exogenous disturbance, and $y_r = G\sigma \in \mathbb{R}$ is the reference trajectory to be tracked. Here H and G are real matrices which map σ to \mathbb{R}^m and \mathbb{R} respectively. $E \in \mathbb{R}^{n \times m}$ translates the disturbance from the exosystem to the plant. The vector $\sigma \in \mathbb{R}^m$ is generated by a linear exosystem,

$$\dot{\sigma}(t) = S\sigma(t)\tag{3.2}$$

where $S \in \mathbb{R}^{m \times m}$. Denote by $\text{eig}(S)$ the set of distinct eigenvalues of the matrix S . We will later use $\text{eig}(S)$ as a design parameter in systems with hysteresis, since the disturbance $Ew(t)$ will arise from a hysteresis operator in systems with hysteresis, rather than an exosystem. It is assumed that (A, B, C, D) is a minimal realization of a SISO plant transfer function, and thus is controllable and observable. The following assumptions are made on the system, as required in [54]:

Assumption 3 $\text{eig}(S) \subset \text{clos}(\mathbf{C}^+) \triangleq \{\lambda \in \mathbf{C}, \text{Re}[\lambda] \geq 0\}$.

Assumption 4 *The system (A, B, C, D) has no zeros at $\text{eig}(S)$.*

Remark 2 *In order to simplify the presentation, we will assume for the remainder of our work that the matrix $D = 0$. This assumption is satisfied for many systems, in particular, for our piezoelectric nanopositioner.*

We will now present the design of our closed-loop controller. We shall integrate into the system a servocompensator, with state η and governed by the differential equations

$$\dot{\eta}(t) = \mathbf{C}^* \eta(t) + \mathbf{B}^* e(t) \quad (3.3)$$

where the matrix $\mathbf{C}^* \in \mathbb{R}^{m \times m}$ possesses the same eigenvalues as S , and \mathbf{B}^* is chosen so that the pair $(\mathbf{C}^*, \mathbf{B}^*)$ is controllable. The control signal $u(t)$ is chosen as a state feedback

$$u(t) = -K_1 x(t) - K_2 \eta(t) \quad (3.4)$$

We can now use (3.3) and (3.4) to close the control loop in for the plant (3.1). This results in the closed loop system,

$$\begin{bmatrix} \dot{x}(t) \\ \dot{\eta}(t) \end{bmatrix} = \begin{bmatrix} A - BK_1 & -BK_2 \\ -\mathbf{B}^* C & \mathbf{C}^* \end{bmatrix} \begin{bmatrix} x(t) \\ \eta(t) \end{bmatrix} + \begin{bmatrix} Ew(t) \\ \mathbf{B}^* y_r(t) \end{bmatrix} \quad (3.5)$$

By Theorem 1 of [53], if the gain vector $[K_1, K_2]$ can be chosen such that closed-loop matrix is Hurwitz, then $e(t) \rightarrow 0$ as $t \rightarrow \infty$. It is shown in [56] that a necessary and sufficient condition for solvability of this problem is that there exist matrices $\Pi \in \mathbb{R}^{n \times p}$ and $\Gamma \in \mathbb{R}^{1 \times p}$ which solve the

linear matrix equations,

$$\begin{aligned} \Pi S &= A\Pi + B\Gamma + E \\ C\Pi &= 0 \end{aligned} \tag{3.6}$$

Thus far, we have acted as if the system parameters are known. A desirable property of servocompensators in closed-loop systems is that the error regulation property is guaranteed for any uncertainty in the system that does not cause instability. This is particularly important in systems with hysteresis, as it is very common for the dynamics/hysteresis model to be inexact, or change with environmental or loading conditions [2, 19], a fact that we will observe in Section 3.4. We will therefore consider a norm-bounded uncertainty [62], where the uncertainty in the plant (3.1) can be represented by

$$\dot{x}(t) = [\hat{A} + B_1^* \Delta^* C_1^*]x(t) + [\hat{B} + B_1^* \Delta^* D_1^*]u(t) \tag{3.7}$$

where

$$A = \hat{A} + B_1^* \Delta^* C_1^* \tag{3.8}$$

$$B = \hat{B} + B_1^* \Delta^* D_1^* \tag{3.9}$$

The matrices B_1^*, C_1^*, D_1^* are known, and represent knowledge of the range of the uncertainties in the matrix/transfer function parameters. The matrix Δ^* is unknown, and satisfies the bound,

$$\Delta^* \leq I, \Delta^{*'} \Delta^* \leq I$$

Now, define the cost functional,

$$J = \int_0^{\infty} [[x(t)', \eta(t)']Q[x(t)', \eta(t)']' + Ru^2] dt, \quad Q = Q' \geq 0, R > 0 \quad (3.10)$$

We define new matrices,

$$\check{A} = \begin{bmatrix} \hat{A} & 0 \\ -\mathbf{B}^*C & \mathbf{C}^* \end{bmatrix}, \check{B} = \begin{bmatrix} \hat{B} \\ 0 \end{bmatrix}, B_1 = \begin{bmatrix} B_1^* & 0 \\ 0 & 0 \end{bmatrix},$$

$$C_1 = \begin{bmatrix} C_1^* & 0 \\ 0 & 0 \end{bmatrix}, D_1 = \begin{bmatrix} D_1^* \\ 0 \end{bmatrix}$$

where each 0 represents an appropriately defined zero matrix. We can then present the following lemma, adapted from Theorem 1 in [62].

Lemma 1 *If for some $\iota = \iota_1^* > 0$, $R = R^* > 0$, there exists a unique positive definite solution $P = P^*$ to the Riccati equation*

$$\begin{aligned} & [\check{A} - \check{B}(\iota R + D_1' D_1)^{-1} D_1' C_1]' P \\ & + P [\check{A} - \check{B}(\iota R + D_1' D_1)^{-1} D_1' C_1] \\ & + \iota P B_1 B_1' P - \iota P \check{B} (\iota R + D_1' D_1)^{-1} \check{B}' P \\ & + 1/\iota C_1' (I - D_1 (\iota R + D_1' D_1)^{-1} D_1') C_1 + Q = 0 \end{aligned} \quad (3.11)$$

then for any fixed $\iota \in (0, \iota_1^*)$ and any fixed $R \in (0, R^*)$, Eq. (3.11) has a unique positive definite

stabilizing solution P , and the control law

$$u(t) = -(lR + D_1' D_1)^{-1} (lB_1' P + D_1' C_1) [x'(t), \eta'(t)]' \triangleq -[K_1, K_2] \begin{bmatrix} x(t) \\ \eta(t) \end{bmatrix} \quad (3.12)$$

guarantees exponential stability of the closed-loop system (3.5) when $y_r(t) = w(t) = 0$, and the matrices A and B are given by (3.8) and (3.9) respectively.

3.3 Asymptotically Stable Periodic Solutions in Systems with Hysteresis

We will now consider the behavior of the controller (3.3), (3.12) when the input $u(t)$ is the output of a hysteresis operator, as assumed in (1.1). The plant output to be controlled is now modeled as a cascade of a modified PI operator (2.16) and the dynamic system (3.1). Furthermore, we will assume that this plant is uncertain, with the dynamic uncertainties obeying (3.8) and (3.9), and the hysteresis uncertainty obeying Assumption 2.

We will now introduce the hysteresis inversion (2.26) into the control structure. The input to the inversion, denoted as $u_d(t)$ in (2.25), will be defined by the right-hand side of (3.12),

$$u_d(t) = -[K_1, K_2] [x'(t), \eta'(t)]' \quad (3.13)$$

Together with (2.25), the closed-loop system (3.5) can now be written as

$$\begin{bmatrix} \dot{x}(t) \\ \dot{\eta}(t) \end{bmatrix} = \begin{bmatrix} A - BK_1 & -BK_2 \\ -\mathbf{B}^* C & \mathbf{C}^* \end{bmatrix} \begin{bmatrix} x(t) \\ \eta(t) \end{bmatrix} + \begin{bmatrix} \hat{\theta}'_d D_z (\hat{\theta}'_h W(t)) - \theta'_d D_z (\theta'_h W(t)) \\ \mathbf{B}^* y_r(t) \end{bmatrix} \quad (3.14)$$

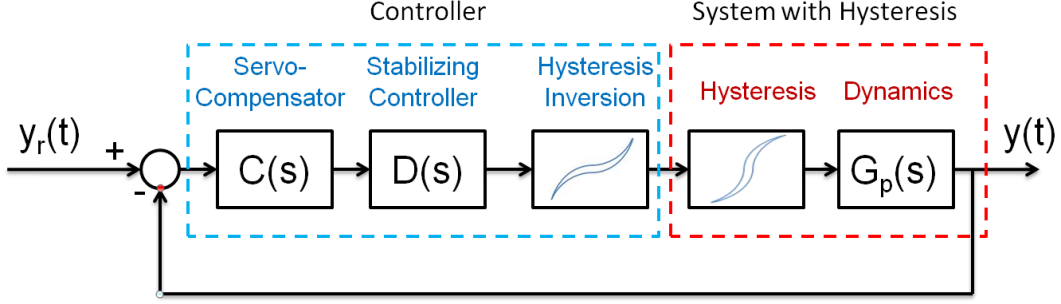


Figure 3.1: Closed-loop system with hysteresis, as defined in (3.13), (3.14), and (2.27).

where $W(t)$ is defined by (2.27). A block diagram of this closed-loop system is illustrated in Fig. 3.1.

The addition of the hysteresis operator into the closed-loop system creates a series of problems in the implementation of the servocompensator controller. First, does the system remain stable with the state feedback (3.12)? In addition, are the trajectories of the closed-loop system periodic for periodic reference trajectories? Such periodicity would allow us to argue that the servocompensator can attenuate the effect of hysteresis on the closed-loop system.

If $W(t)$ was a bounded exogenous disturbance generated by (3.2), the answer to both questions is clearly yes. It turns out that, if the effect of hysteresis is sufficiently small, we can also prove both of these properties closed-loop system with hysteresis. Based on the framework presented in Theorem 2.1 of [63], we can prove, under suitable conditions on the hysteresis operator, the existence of a unique, asymptotically stable, periodic solution. The most restrictive of these conditions is the existence of a contraction property for the composite hysteresis operator \mathcal{W}_d . We will see that this condition can be met for a T -periodic reference trajectory $y_r(t)$ if $u_d(t)$ and $v(t)$ satisfy the following assumption.

Assumption 5 $osc_{[0,T]}[\theta_d d_z(u_{dT})] > 2\bar{r}_p$ and $osc_{[T,2T]}[v_T] > 2r_p$ where, for any continuous func-

tion z ,

$$\text{osc}_{[t_1, t_2]}[z] = \sup_{t_1 \leq \tau \leq \sigma \leq t_2} |z(\tau) - z(\sigma)|$$

and r_p and \bar{r}_p are the largest play radii for Γ_{hd} and $\hat{\Gamma}_{hd}^{-1}$ respectively.

Before proving the existence of an asymptotically stable, periodic solution, we must first show the well-posedness of the closed-loop system. Let $\mathbb{W}_t^{1,1}$ be the Banach space of absolutely continuous functions $u : [0, t] \rightarrow \mathfrak{R}$. We also equip this space with the norm

$$\|u\|_{\mathbb{W}_t^{1,1}} = |u(0)| + \int_0^t |\dot{u}(s)| ds \quad (3.15)$$

Note that, for $f_1, f_2 \in \mathbb{W}_t^{1,1}$ the play operator P_{ri} obeys the condition

$$|P_{ri}[f_1; a](s) - P_{ri}[f_2; a](s)| \leq \|f_1(s) - f_2(s)\|_\infty$$

This property along with (2.29) allows us to prove that the composite hysteresis operator \mathscr{W}_d is Lipschitz continuous, i.e.

$$\|\mathscr{W}_d[f_1; W(0)](s) - \mathscr{W}_d[f_2; W(0)](t)\| \leq L\|f_1 - f_2\|_\infty$$

It is then clear that the right-hand side of (3.14) is Lipschitz continuous, and so the existence and uniqueness of the solution can be established through the typical contraction mapping argument [64]. Similar continuity properties can be proved for the dependence of the system on initial condition; therefore the system (2.27), (3.13), and (3.14) is well posed. We are now prepared to prove the following theorem.

Theorem 1 *Consider the closed-loop system (2.27), (3.13), and (3.14). Let Assumptions 2-5 hold,*

and let the reference trajectory $y_r(t)$ be periodic with period T . Then, there exists an ε such that if $\varepsilon_d < \varepsilon$, where $\varepsilon_d = \max(\|\tilde{\theta}_h\|, \|\tilde{\theta}_d\|)$, the solutions of the closed-loop system (2.27), (3.13), and (3.14), under any initial condition $(x(0), \eta(0), W(0))$, will converge asymptotically to a unique periodic solution.

Proof. Consider an input $f(t)$ with $\text{osc}_{[0,T]}[f(t)] > 2r$. Let P_r be a play operator with radius r . From (2.1) it can be seen that this play operator obeys the contraction property

$$|P_{ri}[f;a](t) - P_{ri}[f;b](t)| = 0, \forall t > T$$

for any two applicable initial conditions a and b . From (2.13), \mathcal{W} is a composite hysteresis operator, formed by the inverse PI operator Γ_{hd}^{-1} , whose largest play radius is \bar{r}_p and the play operators of Γ_{hd} , where the largest play radius is r_p . Assumption 5 therefore implies that, for $t > 2T$,

$$|\mathcal{W}[u_d; W_a(0)](t) - \mathcal{W}[u_d; W_b(0)](t)| = 0 \quad (3.16)$$

for any two applicable initial conditions $W_a(0)$ and $W_b(0)$. We will also note that the modified PI operator (and therefore \mathcal{W}) satisfies the Volterra property

$$f_1(s) = f_2(s), 0 \leq s \leq t \Rightarrow \Gamma_{hd}[f_1; W(0)](t) = \Gamma_{hd}[f_2; W(0)](t), \forall t \geq 0 \quad (3.17)$$

and the semi-group property

$$\Gamma_{hd}[f_2; \Gamma_{hd}[f_1; W(0)](t_1)](t_2 - t_1) \equiv \Gamma_{hd}[f_1; W(0)](t_2), \text{ if } f_2(t) = f_1(t - t_1) \quad (3.18)$$

Finally, we know from the definition of the play operators and the modified PI operator that there

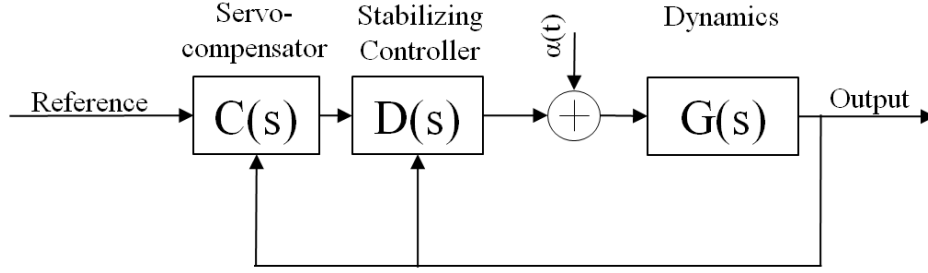


Figure 3.2: Equivalent block diagram for the closed-loop system (2.13),(3.13), and (3.14) in steady state analysis.

exist constants a_g and b_g such that the growth condition

$$\|W(t)\| \leq a_g \|u_d(t)\| + b_g, \forall t \quad (3.19)$$

is satisfied. From our discussions in Section 3.2, we know that if $\varepsilon_d = 0$, i.e. $\tilde{\theta}_h = \tilde{\theta}_d = 0$, the closed-loop system possesses a globally exponentially stable T -periodic solution $(x_T(t), \eta_T(t))$. Therefore, the closed-loop system fits into the class of systems considered in Theorem 2.1 of [63], and for a sufficiently small ε_d there exists an asymptotically stable T -periodic solution $(x(t), \eta(t), W(t))$ for the closed-loop system (2.13),(3.13), and (3.14). \square

Remark 3 *This Theorem can also be applied to a classical PI operator, by considering $\tilde{\theta}_d = 0$.*

Having now established the existence, uniqueness, and stability of the periodic solution $(x(t), \eta(t), W(t))$, we can now discuss the steady state performance of the controller. From the T -periodicity of $W(t)$, we can equivalently write the inversion error (2.26) as the Fourier series

$$\alpha(t) = \theta'_d D_z(\theta'_h W(t)) - \hat{\theta}'_d D_z(\hat{\theta}'_h W(t)) = c_0 + \sum_{k=1}^{\infty} c_k \sin\left(\frac{2\pi kt}{T} + \phi_k\right) \quad (3.20)$$

for some constants ϕ_1, ϕ_2, \dots and $c_0, c_1, \dots \geq 0$. We have now shown that the effect of hysteresis at steady state can be reduced to an equivalent exogenous disturbance $\alpha(t)$, as we illustrate in

Fig. 3.2. We therefore separate the disturbance $\alpha(t)$ into two components. Let us assume that the matrix C^* in our servocompensator (3.3) has been chosen such that its eigenvalues are located at $\pm jk\omega$, $k \in \rho$, where ρ is a finite element vector of whole numbers, and then define

$$\begin{aligned}\alpha_c(t) &= c_0 + \sum_{k \in \rho} c_k \sin\left(\frac{2\pi kt}{T} + \phi_k\right) \\ \alpha_d(t) &= \sum_{k \notin \rho} c_k \sin\left(\frac{2\pi kt}{T} + \phi_k\right)\end{aligned}\tag{3.21}$$

From the properties of the servocompensator, we know that any effect of the disturbance α_c will be eliminated from the system at steady state. Therefore the tracking error under the proposed control scheme will be of the order of α_d , which can be made arbitrarily small by accommodating a sufficient number of harmonics in the servocompensator design.

3.3.1 Output Feedback Control of Systems with Servocompensators

It should be noted that there are many other ways of designing the desired stabilizing control $u_d(t)$, as opposed to the riccati equation approach presented in (3.12). A variety of techniques including LQG control, H_∞ control, or observer theory can be used to stabilize the closed-loop system. In the interest of our experimental implementation, we will now discuss the implementation of an output feedback controller in our closed-loop system. We will use a luemberger observer,

$$\hat{\dot{x}}(t) = A\hat{x}(t) + Bu_d(t) + L(y(t) - C\hat{x}(t))\tag{3.22}$$

which transforms (3.13) into

$$u_d(t) = -[K_1, K_2] \begin{bmatrix} \hat{x}(t) \\ \eta(t) \end{bmatrix}\tag{3.23}$$

The gain vector L is chosen so that $A - LC$ is a Hurwitz matrix. The design of Luenberger observers requires the plant matrices A and B to be known; therefore in the case of output feedback we require the uncertainty Δ^* to be identically zero to show stability. Under this assumption, we can integrate the observer into the control loop, which results in the closed-loop system

$$\begin{bmatrix} \dot{x}(t) \\ \dot{\eta}(t) \\ \dot{\hat{x}}(t) \end{bmatrix} = \begin{bmatrix} A & -BK_2 & -BK_1 \\ -\mathbf{B}^*C & \mathbf{C}^* & 0 \\ LC & -BK_2 & A - BK_1 - LC \end{bmatrix} \begin{bmatrix} x(t) \\ \eta(t) \\ \hat{x}(t) \end{bmatrix} + \begin{bmatrix} \hat{\theta}'_d D_z(\hat{\theta}'_h W(t)) - \theta'_d D_z(\theta'_h W(t)) \\ \mathbf{B}^* y_r(t) \\ 0 \end{bmatrix} \quad (3.24)$$

where the system matrix is Hurwitz. As this system possesses an exponentially stable T -periodic solution when $\varepsilon_d = 0$, we can apply Theorem 2.1 of [63] and conclude stability of the closed-loop system in an identical manner to the proof of Theorem 1.

3.4 Experimental Implementation of Proposed Controller

3.4.1 Nanopositioner Modeling

We now examine the performance of the proposed control scheme on a piezo-actuated nanopositioner, shown in Fig. 3.3. We have discussed the practical importance along with the need for improved controllers for nanopositioning in Chapter 1. This platform therefore provides a valuable and practically relevant test of our controller's performance in systems with hysteresis.

The first step in our experimental tests involves model identification for the piezo-actuated nanopositioner. The hysteretic behavior was experimentally characterized using a quasi-static input, which sweeps the positioner output over its operational range. As seen in Fig. 3.4, the hystere-

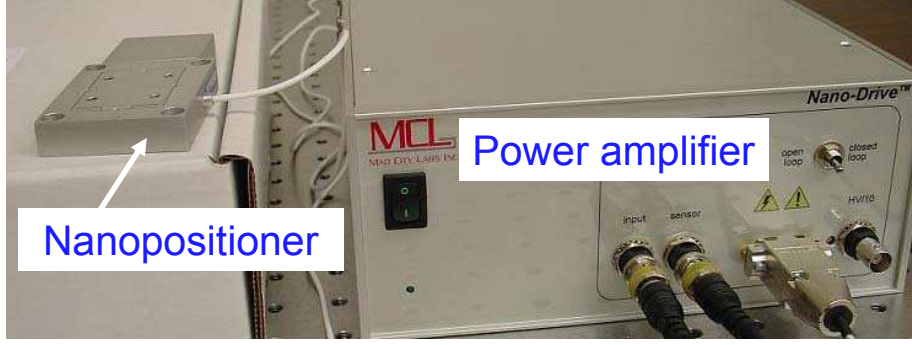


Figure 3.3: Nanopositioning stage used in experimentation, Nano-OP65 nanopositioning stage coupled with a Nano-Drive controller from Mad City Labs Inc, with a primary resonance of 3 kHz. Position feedback is provided by a built-in capacitive sensor.

sis loop is not odd-symmetric; therefore we use a modified PI operator (2.24) with with 9 deadzone elements and 8 play elements to model the asymmetric hysteresis. In addition, a bias scheme was used to center the hysteresis loop about the origin; this was accomplished by subtracting $25.9 \mu\text{m}$ from the plant output and 4V from the plant input in the modeling procedure. The radii r and thresholds z were chosen based on the input and output range of the plant,

$$r = [0, 0.33, 0.66, 1.00, 1.33, 1.66, 2.00, 2.33]'$$

$$z = [-2.68, -1.97, -1.22, -0.42, 0, 0.32, 1.02, 1.76, 2.57]'$$

We then identify the model weights $\hat{\theta}_h$ and $\hat{\theta}_d$ using quadratic optimization routine outlined in [32]:

$$\hat{\theta}_h = [0.719, 0.183, 0.035, 0.055, 0.034, 0.033, 0.023, 0.061]'$$

$$\hat{\theta}_d = [1.062, 0.473, 0.641, 0.311, 8.426, -0.636, -0.501, -0.614, -0.415]'$$

The model weights $\hat{\theta}_h$ and $\hat{\theta}_d$ are then used to calculate the inverse operator, $\hat{\Gamma}_{hd}^{-1}[u_d, W(0)](t)$. Since the model $\hat{\Gamma}_{hd}$ is generated by biasing the input and output, we are required to subtract 25.9

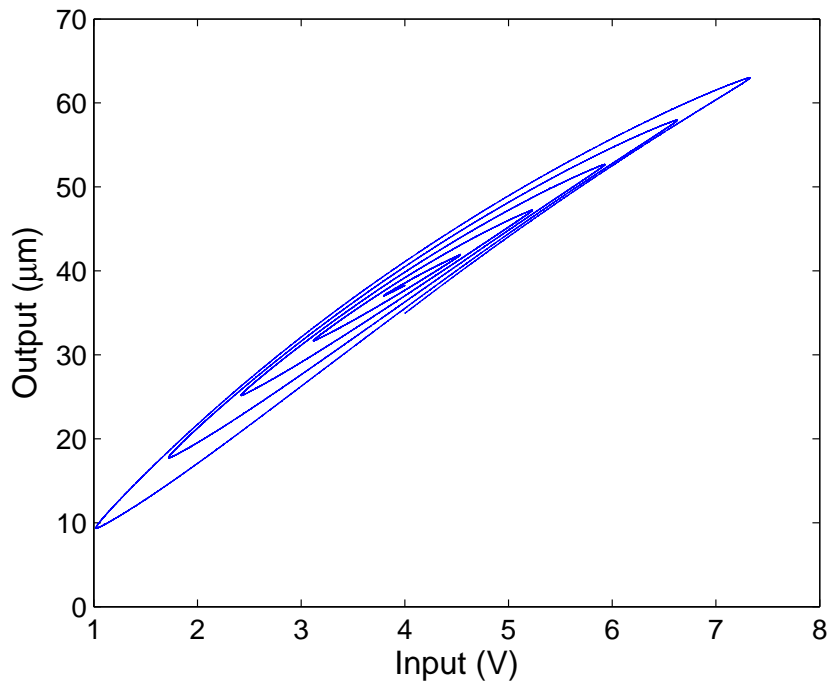


Figure 3.4: Measured hysteresis loops for the nanopositioner.

from the inversion input and add 4 to the inversion output to maintain the inversion structure. A comparison between the model and plant output is shown in Fig. 3.6. The discrepancy between the model prediction and the actual measurement was around $1 \mu\text{m}$ over a travel range of $45 \mu\text{m}$.

We then model the plant dynamics, using frequency response identification techniques with small-amplitude sinusoidal inputs to reduce the impact of hysteresis on the measurements. We found that a fourth-order plant model matched the measured frequency response reasonably well, up to 3.5 kHz. We also set the DC gain of the dynamics to zero, since the DC gain is accounted for in the hysteresis operator. This model has the transfer function

$$G(s) = \frac{8.8 \times 10^{16}}{s^4 + 1.6 \times 10^4 s^3 + 6.6 \times 10^8 s^2 + 5.3 \times 10^{12} s + 8.8 \times 10^{16}} \quad (3.25)$$

Note that the combination of high resonant frequency and order has resulted in very large numbers in (3.25). In order to improve computation accuracy, we used a balanced state-space realization

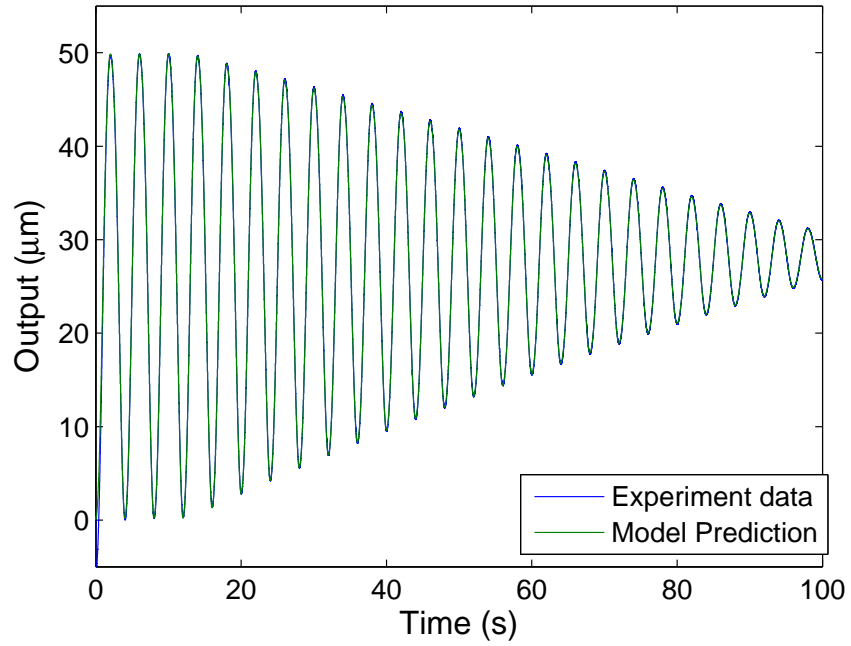


Figure 3.5: Plant output used in the identification of the modified PI operator, and resulting model output.

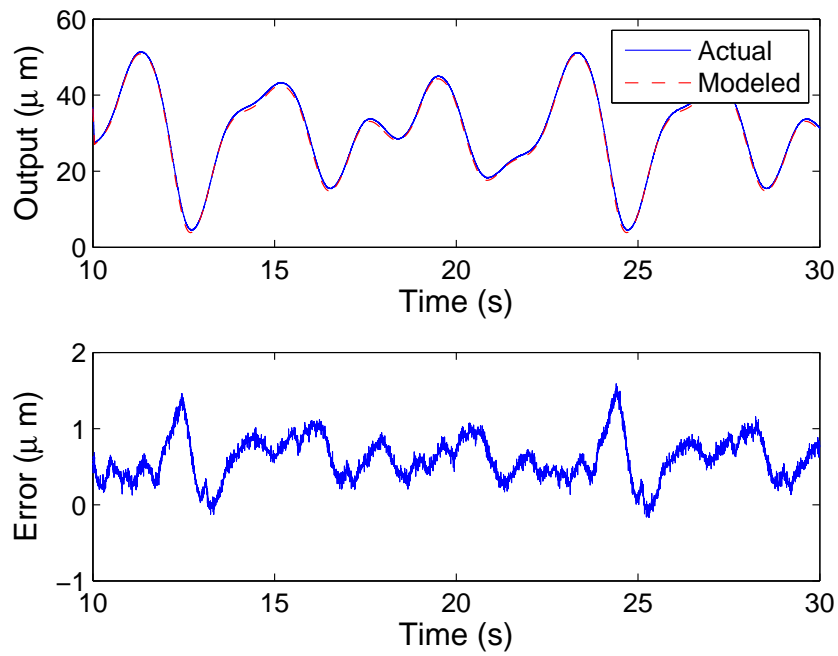


Figure 3.6: Model prediction and experimental data for a decreasing sinusoid used to optimize the hysteresis model.

[65] in our control design:

$$\begin{aligned} \dot{x}(t) &= 1.0 \times 10^4 \begin{bmatrix} -0.014 & 1.700 & 0.095 & -0.050 \\ -1.700 & -0.241 & -0.672 & 0.170 \\ 0.095 & 0.672 & -1.066 & 1.617 \\ 0.050 & 0.170 & -1.617 & -0.305 \end{bmatrix} x(t) + \begin{bmatrix} 27.8 \\ 111.3 \\ -116.5 \\ -44.1 \end{bmatrix} u(t) \\ y(t) &= \begin{bmatrix} 27.8 & -111.3 & -116.5 & 44.1 \end{bmatrix} x(t) \end{aligned} \quad (3.26)$$

These matrices then define the nominal plant matrices $(\hat{A}, \hat{B}, C, 0)$, as defined in 3.8 and 3.9. We next designed our robust stabilizing control (3.12). We then tested how the model parameters varied by loading weight onto the nanopositioning stage. We found that with a maximum load, the parameters of (3.25) varied by around $\pm 5\%$. Therefore, we designed our controller to be robust to changes of $\pm 10\%$ in the parameters of (3.25). We then translated this constraint into balanced coordinates via the same coordinate transformation used to generate (3.26). The resulting matrices become the B_2 , C_1 , and D_1 matrices used in (3.11). Together with the balanced coordinate system matrices from (3.26), we can then calculate the stabilizing control (3.12).

Finally, we implement a Luenberger observer to estimate the states, as explored in Section 3.3.1. Designed and implemented in the standard manner with the nominal state space model of the plant, the output feedback controller is given as

$$\hat{\dot{x}}(t) = \hat{A}\hat{x}(t) + \hat{B}u_d(t) + L(y(t) - C\hat{x}(t)) \quad (3.27)$$

$$u_d(t) = - [K_1, K_2] \begin{bmatrix} \hat{x}(t) \\ \eta(t) \end{bmatrix} \quad (3.28)$$

where L is chosen so that $\hat{A} - LC$ is Hurwitz. In our work, L is chosen using an LQR method, and

equals $[0.3, -3.5, -1.7, -0.23]$.

3.4.2 Experimental Results

We now present the results of our controller implementation. Control and measurement were facilitated by a dSPACE platform. For comparison, we implemented an iterative learning control (ILC) algorithm [38], and a custom-designed proportional-integral controller with hysteresis inversion (PI+I). When discussing the proposed controller, we will distinguish between a single-harmonic servocompensator (SHSC), and a multi-harmonic servocompensator (MHSC). The SHSC is strictly second order, and compensates for the primary harmonic of the reference only. The order of the MHSC will vary between experiments.

Our first set of experiments considers sinusoidal waveforms for the reference trajectory,

$$y_r(t) = (20 \sin(2\pi\omega t) + 30)\mu m$$

with frequencies of 5, 25, 50, 100 and 200 Hz. Two metrics are used to quantify the tracking error. The mean tracking error (MTE) is computed by taking the average of $|e(t)|$ at steady state, and the peak tracking error (PTE) is the average of the maximum tracking error in each period of the reference. Both metrics are computed at steady state.

Table 3.1: Tracking error results for various controllers. All results are presented as a percentage of the reference amplitude ($20\mu m$).

Reference	MHSC (%)		SHSC (%)		ILC (%)		PI+I (%)	
	MTE	PTE	MTE	PTE	MTE	PTE	MTE	PTE
Sine, 5 Hz	0.271	0.899	0.649	1.72	0.135	0.250	1.06	1.93
Sine, 25 Hz	0.268	0.881	0.707	1.85	0.163	0.565	5.40	8.96
Sine, 50 Hz	0.284	1.01	0.770	1.93	0.262	0.711	10.86	17.63
Sine, 100 Hz	0.352	1.03	0.815	2.38	0.528	1.42	21.21	33.65
Sine, 200 Hz	0.519	1.57	0.863	2.50	1.31	3.20	37.61	59.6

Table 3.1 contains the results for each reference and controller, where the MHSC contains the first, second, and third harmonics of the reference. The PI+I controller performs very poorly at high frequencies, a problem that has been well documented [2, 39]. The ILC algorithm performs very well in general, but cannot match the MHSC at 200 Hz, as shown in Fig. 3.7. A detailed comparison between the ILC and MHSC methods is shown in Fig. 3.8. At low frequencies, the ILC algorithm performs better than the MHSC. At 50 Hz, the errors are very close, with ILC still slightly ahead. However, at 100 Hz and 200 Hz, the MHSC is significantly better, with only 40% the mean tracking error of ILC at 200 Hz.

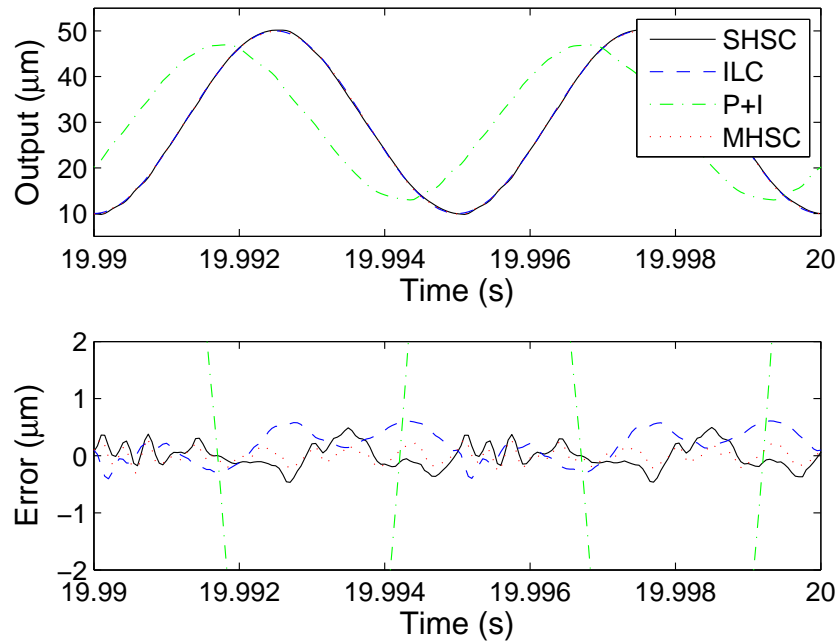


Figure 3.7: Experimental results at 200 Hz for the proposed methods (SHSC and MHSC), ILC and PI+I.

We can also compare the performance of the multi-harmonic servocompensator (MHSC) with that of the single-harmonic servocompensator (SHSC). From our theoretical results, we would expect the MHSC to perform significantly and consistently better than the SHSC; this is confirmed in Table 3.1, as the MHSC outperforms the SHSC by significant margins at each frequency for

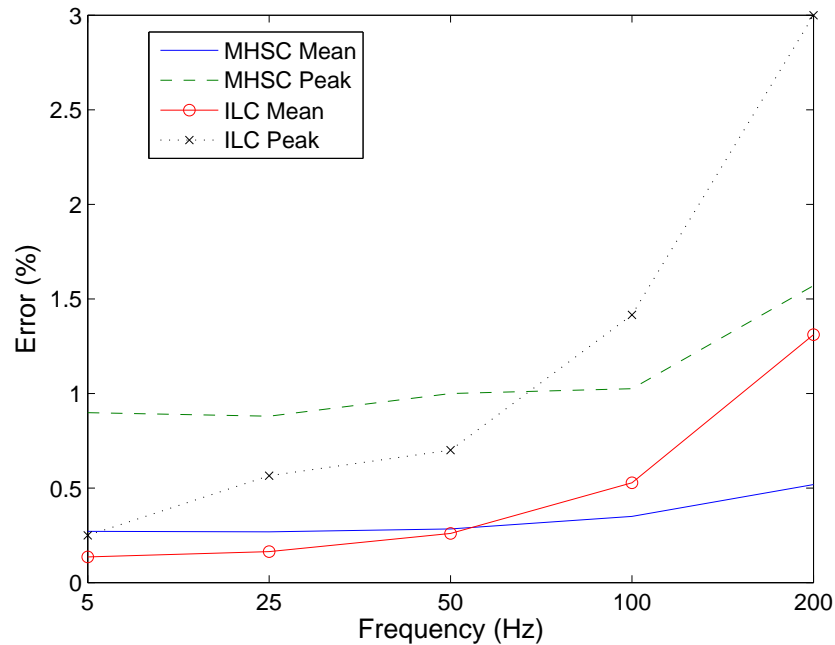


Figure 3.8: Comparison between multi-harmonic servocompensator (MHSC) and Iterative Learning Control (ILC).

both error metrics. However, the performance gap narrows as the reference frequency increases. At 5 Hz, the MHSC has around 40% of the tracking error of the SHSC, whereas at 200 Hz the MHSC has 60%. This can be attributed to the resonant peak of the vibrational dynamics of the system. In particular, with increasing frequencies, the harmonics higher than the second and third become more significant. Fig. 3.9 shows the spectra under SHSC for reference signals at 5 and 200 Hz. In both cases, the second and third harmonics of the reference signal are the most significant in the error signal. However, the other harmonics of the system are significantly larger at 200 Hz in comparison to the dominant second and third harmonics than they are at 5 Hz. It is therefore reasonable to expect that canceling the second and third harmonics in the 200 Hz case would result in reduced benefit as compared to that in the 5 Hz case.

We also demonstrate the ability for the MHSC to track sawtooth reference signals. Sawtooth signals are commonly used in SPM applications, and represent a challenge for our proposed con-

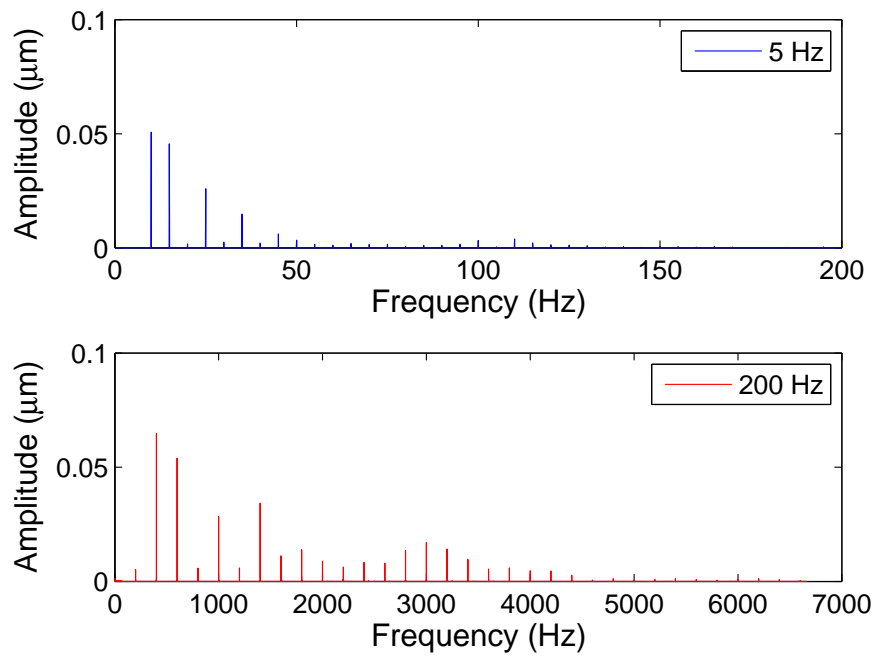


Figure 3.9: Frequency spectra of the tracking error signal for references at 5 Hz and 200 Hz. An SHSC was used in each case. Graphs are aligned so that the peaks on each graph correspond to the same harmonic of the reference. Note the prominence of the harmonics near 3000 Hz in the 200 Hz plot.

troller since they do not have a finite-dimensional internal model. However, by using the first few harmonics of the signal, we can arrive at a reasonable approximation. Fig. 3.10 and Table 3.2 show tracking error results for the three control methods used, where the MHSC incorporated the first 6 odd harmonics of the reference. The ILC controller is well suited to tracking signals like a sawtooth, and this is shown in the tracking results. While the PI+I controller has reasonable performance at 5 Hz, its performance falls off dramatically at 50 Hz. The MHSC does a significantly better job than the P+I controller at tracking this signal, with an average error that was only 20% of what was achieved by the latter controller at 50 Hz. While the tracking error under the MHSC is almost five times of that under ILC at 5 Hz, it becomes comparable to that of ILC with smaller maximum error at 50 Hz, indicating that the MHSC can facilitate tracking of such sawtooth signals.

Table 3.2: Tracking errors results for a Sawtooth signals. All results are presented as a percentage of the reference amplitude ($20\mu\text{m}$).

	5 Hz (%)		50 Hz (%)	
	MTE	PTE	MTE	PTE
MHSC	0.562	4.15	1.08	4.26
ILC	0.114	0.775	0.808	5.70
P+I	1.08	1.30	10.3	12.1

We also test the performance of the proposed controller under more complex inputs. Fig. 3.11 shows the experimental results for the MHSC and ILC with a reference signal of

$$y_r(t) = 5 \sin(2\pi 5t - \pi/2) + 5 \sin(2\pi 15t + \pi/2) + 10 \sin(2\pi 25t - \pi/2)$$

Such an input excites more complex memory states for hysteresis than a sinusoidal or sawtooth input, and is a useful test of the proposed controller's ability to compensate for hysteresis. For this experiment, the MHSC is designed to compensate for the reference signal alone, yielding a 6th order servocompensator. The resulting mean tracking errors are 0.52% for the MHSC and

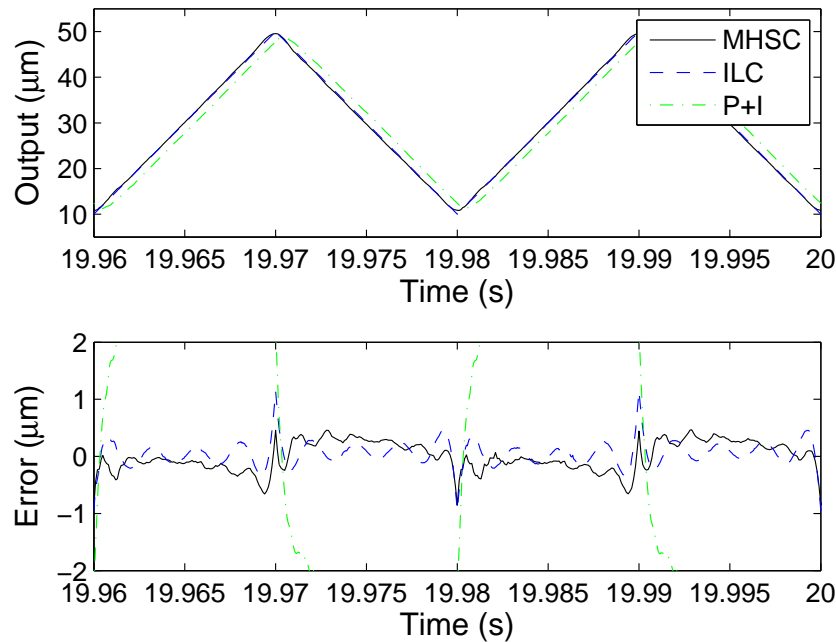


Figure 3.10: Experimental results at 50 Hz for sawtooth reference signal. Two periods are shown.

0.66% for ILC. Even though the reference is fairly slow, the advantage that ILC possesses at low frequencies for the sinusoidal references has been reversed in this test by the MHSC. This proves the effectiveness of the proposed controller at compensating for hysteresis in general systems.

Finally, we investigated the robustness of the system's performance to loading conditions. To prevent damage to the nanopositioner, we limited our experiments to 40% (200 g) of the maximum load recommended by the manufacturer. ILC and a MHSC (accommodating first three harmonics) were used for this study. Table 3.3 shows the results for tracking a 50 Hz signal for the loaded operation, as well as the percent-change from the nominal results presented in Table 3.1. The performance of the MHSC is nearly unchanged from the unloaded case, a point also readily visible in Fig. 3.12. The ILC controller, however, has suffered a notable drop in performance, with double-digit percentage drops in accuracy in the loaded case. However, due to ILC's better performance in the unloaded case, both methods are very close in the raw performance. This result indicates that

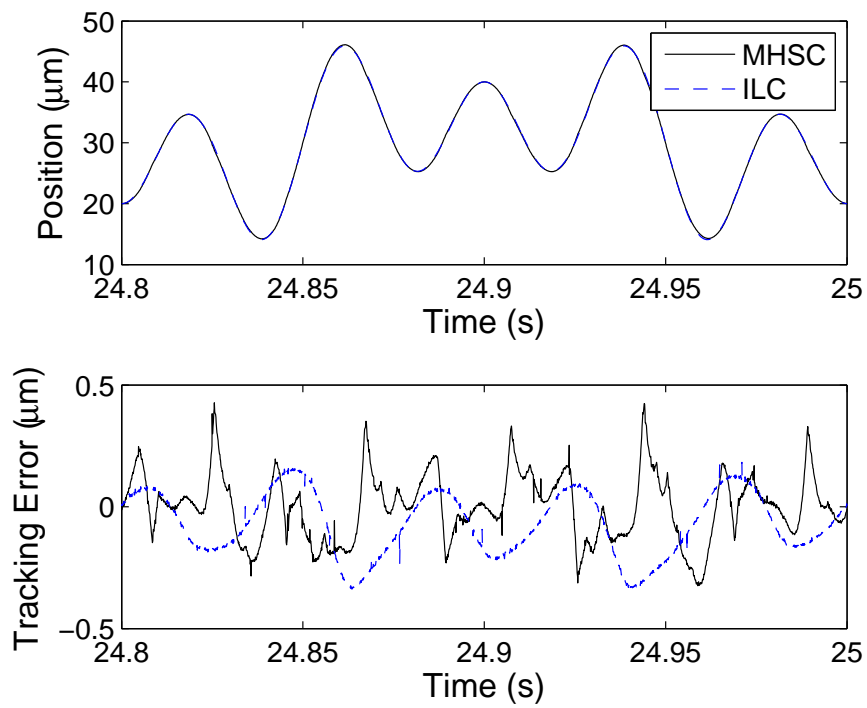


Figure 3.11: Experimental results for a reference trajectory of $y_r = 5 \sin(2\pi 5t - \pi/2) + 5 \sin(2\pi 15t + \pi/2) + 10 \sin(2\pi 25t - \pi/2)$

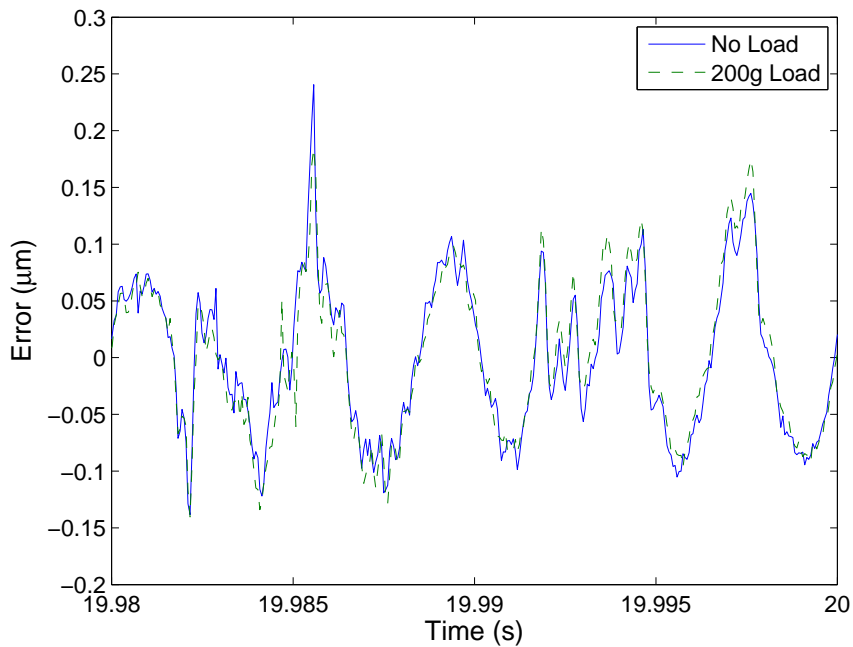


Figure 3.12: Tracking errors for a 50 Hz reference signal, for loaded and unloaded nanopositioner. An MHSC was used in both cases. Note the similarity in the time trajectory of the tracking error.

the MHSC's performance is significantly less tied to modeling accuracy than ILC's, since the net effect of a load is to deviate the plant from its nominal dynamics, which proves the performance robustness properties discussed in Section 3.3.

Table 3.3: Loading performance for MHSC and ILC. First two columns are presented as a percentage of the reference amplitude ($20\mu\text{m}$), second two columns are percent change from the unloaded case.

	MTE	PTE	Δ MTE	Δ PTE
MHSC	0.288	0.940	1.41	-6
ILC	0.308	0.775	18.5	10.7

Chapter 4

Harmonic Analysis of Hysteresis Operators with Application to Control Design for Multi-Harmonic Servocompensators

4.1 Introduction

We now provide a design tool for the MHSC proposed in this dissertation. Consider the expression (3.21), which describes the effect of hysteresis on the closed-loop system at steady state, and let $G_{\alpha e}$ denote the transfer function from $\alpha(t)$ to $e(t)$ of the nominal closed-loop system (2.13), (3.13), and (3.14) where $\varepsilon_d = \max(\|\tilde{\theta}_h\|, \|\tilde{\theta}_d\|) = 0$. If α_d is known, the steady state function for $e(t)$ can be derived from the expression $e(t) = G_{\alpha e}(s)[\alpha_d(t)]$. However, the trajectory of α_d is dependent on the hysteresis operator; specifically, the amplitudes c_k and phases ϕ_k are unknown functions of the system parameters and hysteresis operator. Theoretically, it is possible that these coefficients are prohibitively large; however, we can see from our experimental results that α_d is reasonably small.

Recall from Chapter 3 that the order of the servocompensator can be used directly as a design aid to improve tracking performance. As a control engineer, it is desirable to obtain the minimum order and complexity for the controller to accomplish a given objective. Existing design techniques

for the MHSC consist of repeated iterations of different controller orders until the desired performance is met, which is both *ad hoc* and time consuming. Therefore, it is of interest to evaluate the harmonic components of a hysteresis operator in terms of the hysteresis parameters.

We now present our results on such an algorithm, which evaluates the Fourier coefficients [66] of the output produced by a hysteresis operator in an open-loop system. This algorithm is applicable to both PI and PKP operators, and has two primary components. First, we form the output of the hysterons using a series of pulse signals. The pulse signals are defined through a set of time instants at which the hysteresis behavior switches, and they are determined by a combination of the input signal and operator parameters. Second, we use this formulation to compute the Fourier series of the output. For the example of a play operator subject to a sinusoidal or sawtooth signal, we provide explicit expressions for the coefficients, which are functions of the input amplitude and the hysteron parameters. We will also show that the resulting expressions provide some valuable control design tools for closed-loop systems such as that in Chapter 3.

4.2 Open-Loop Computation of Hysteresis Operator Outputs

Recall that any periodic signal $\sigma(t)$ with period $T \triangleq 2\pi/\omega$ can be written as an infinite summation in the form

$$\sigma(t) = a_0/2 + \sum_{n=1}^{\infty} a_n \cos(\omega nt) + b_n \sin(\omega nt) \quad (4.1)$$

where the coefficients a_n and b_n are defined by the integrals

$$a_n = \frac{2}{T} \int_0^T \sigma(t) \cos(\omega nt) dt \quad (4.2)$$

$$b_n = \frac{2}{T} \int_0^T \sigma(t) \sin(\omega nt) dt \quad (4.3)$$

For a Preisach-like operator, the Fourier series coefficients of its output can be constructed from those of its constituent hysterons. To see this, consider the example of a PI operator. Recall that the output of any play operator is described by its state, which we have defined as $W_{r_i}[v; W(0)](t)$. Say that we have calculated $W_{r_i}[v; W(0)](t)$ in the Fourier series form

$$W_{r_i}[v; W(0)](t) = a_{i0}/2 + \sum_{n=1}^{\infty} a_{in} \cos(\omega n t) + b_{in} \sin(\omega n t) \quad (4.4)$$

Then the Fourier series coefficients of $u(t) = \Gamma[v](t)$ can be calculated from (2.3) as

$$a_0 = \sum_{i=1}^m \theta_i a_{i0}, \quad a_n = \sum_{i=1}^m \theta_i a_{in}, \quad b_n = \sum_{i=1}^m \theta_i b_{in} \quad (4.5)$$

A similar expression can be quickly derived for the PKP operator as well. Therefore, we will focus our attention on computing the Fourier series for the output of an individual hysteron. We will begin with the play operator, defined in (2.1).

4.2.1 Harmonic Analysis of a Play Operator

In order to compute the Fourier series of a play operator's output, we first need an analytical expression for which a Fourier transform can be easily evaluated. We describe the output as a function of the input as well as a series of pulse wave signals P_1 , P_2 , and P_3 , determined by a set of time instants $T_1 = [t_{11}, t_{12}, \dots]$ and $T_0 = [t_{01}, t_{02}, \dots]$. For a general input, we define the output of a play operator $u(t)$ as

$$u(t) = (v(t) + P_1(t))P_2(t) + P_3(t) \quad (4.6)$$

where

$$P_1(t) = -r(\text{sgn}(\dot{v}(t))) \quad (4.7)$$

$$P_2(t) = \begin{cases} 0, & t \in [t_{ij}, t_{oj}), \forall j = 1, 2, \dots \\ 1, & t \in [t_{oj}, t_{i(j+1)}), \forall j = 1, 2, \dots \end{cases} \quad (4.8)$$

$$P_3(t) = \begin{cases} v(t_{ij}) - r(\text{sgn}(\dot{v}(t_{ij}^-))), & t \in [t_{ij}, t_{oj}) \\ 0, & \text{otherwise (o.w.)} \end{cases} \quad (4.9)$$

and $v(t)$ is the input to the operator. We will assume that the time variable has been shifted so that $u(0)$ lies in the linear region of the play operator. The time instants T_i and T_o are determined systematically based on the reference signal and the radius of the play operator. In particular, t_{ij} is the first time satisfying the conditions

$$\dot{v}(t_{ij}) = 0, t_{ij} > t_{o(j-1)}, \text{sgn}(\dot{v}(t_{ij}^-)) \neq \text{sgn}(\dot{v}(t_{ij}^+))$$

This represents the time when the output of the play operator transitions from a linear region into the flat “play” region. In contrast, t_{oj} is the time period when the output moves out of the “play” region, and is the first time satisfying either

$$|v(t_{ij}) - v(t_{oj})| \geq 2r, t_{oj} \geq t_{ij},$$

or

$$\text{sgn}(\dot{v}(t_{ij}^+))v(t_{oj}) < \text{sgn}(\dot{v}(t_{ij}^+))v(t_{ij}), t_{oj} \geq t_{ij}$$

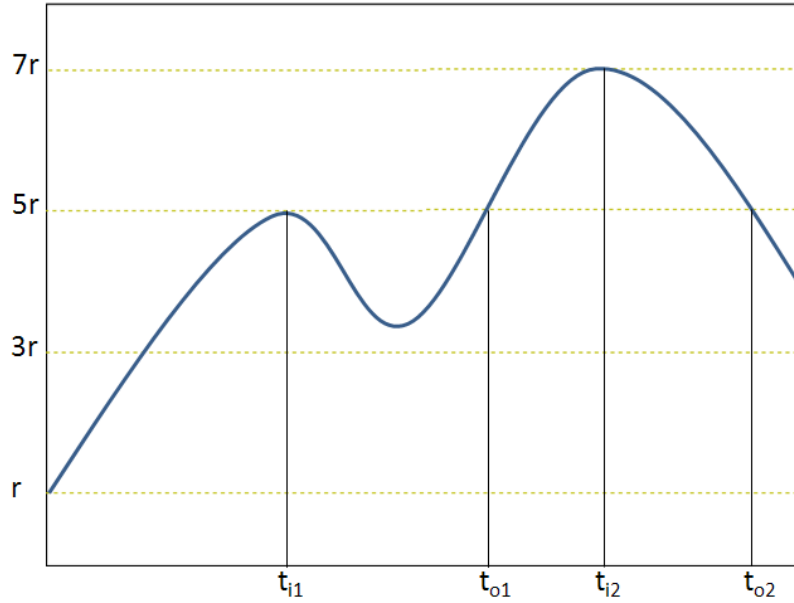


Figure 4.1: A sample curve showing how the time instants T_i and T_o are calculated for a play operator. The variable r is the radius of the play operator, and it is assumed that the input at time zero is $2r$.

Two cases exist for the definition of t_{oj} since there are two ways to exit the play region of the play operator. The first case deals with the output leaving the play region by entering the opposite linear portion from the one it entered. Naturally then, the second case deals with the output leaving the play region by entering the same linear portion as the one it entered from.

Fig. 4.1 shows an example of how the time instants T_i and T_o are calculated for one portion of a periodic signal. The inflection point marked t_{i1} defines the first element of T_i . t_{o1} is defined by the graph returning to the level of $5r$, since the curve did not fall $2r$ from its value at t_{i1} . t_{i2} is the next inflection point after t_{o1} and the third such point plotted on the graph. Finally, t_{o2} is defined by the point where the graph has fallen $2r$ from its value at t_{i2} .

As a further illustration, Fig. 4.2 demonstrates how the play operators output is reconstructed from the input and pulse signals. The reference signal is assumed to be a sinusoid with amplitude of two, and the play operator possesses a radius of 0.3. The vertical dashed lines indicate the time instants for this particular reference and play operator. $P_1(t)$ controls the offset or lag generated

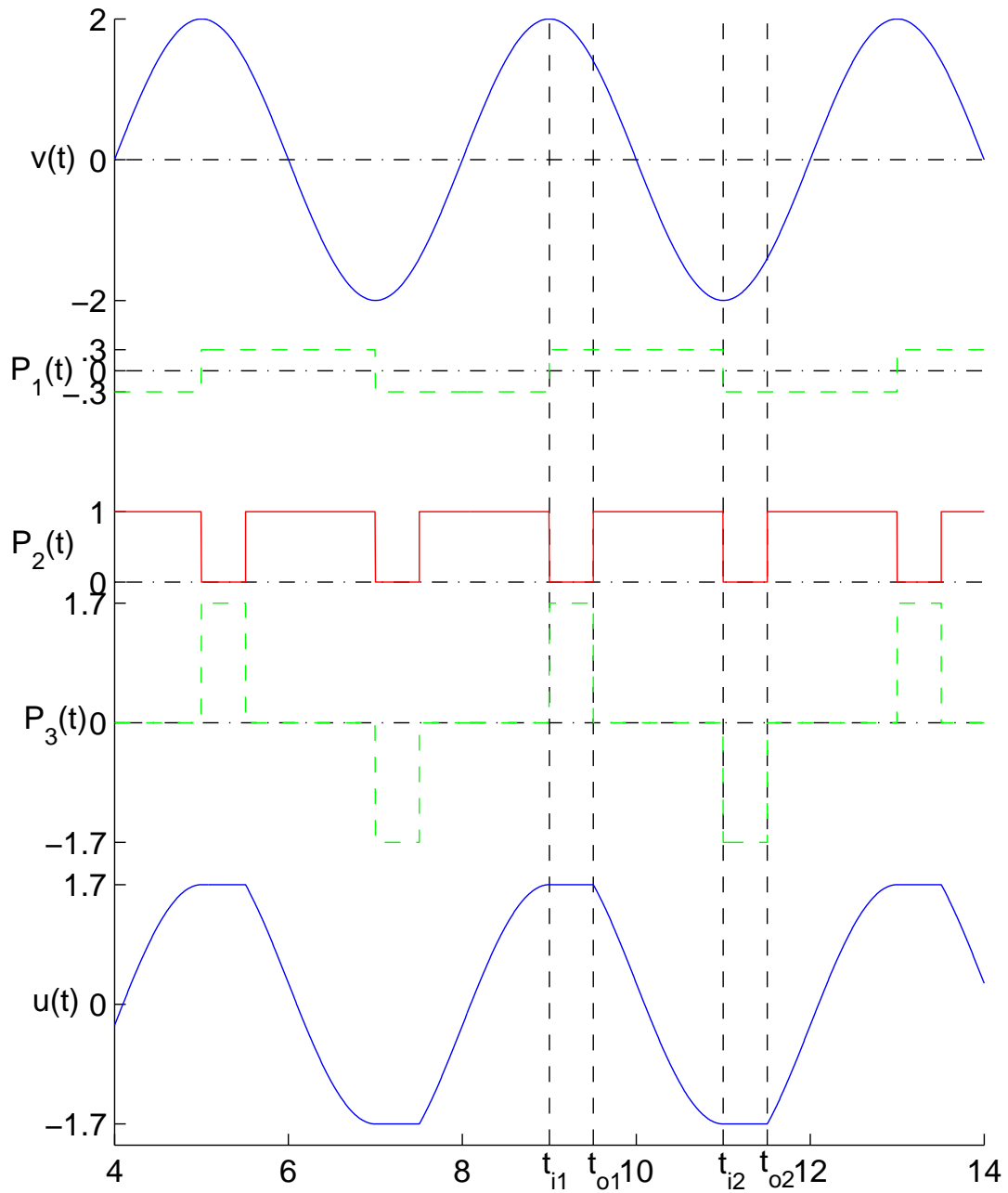


Figure 4.2: Reconstruction of the output $u(t)$ of a play operator. The play radius $r = 0.3$, and the time axis is shared by each signal.

by the play operator in the linear regions. $P_2(t)$ “switches” the output between the play and linear regions of the operator, while $P_3(t)$ “holds” the output when the play operator is in the “play” region.

Having now expressed the output of the play operator in the form (4.6), we can compute the Fourier series of the output $u(t)$. Using (4.6) along with (4.7)-(4.9), we can break up the integrals in (4.2) and (4.3) as

$$a_n = \frac{2}{T} \left[\int_{t_{i1}}^{t_{o1}} (P_3(t)) \cos(\omega nt) dt + \int_{t_{o1}}^{t_{i2}} (v(t) + P_1(t)) \cos(\omega nt) dt + \int_{t_{i2}}^{t_{o2}} (P_3(t)) \cos(\omega nt) dt + \dots \right] \quad (4.10)$$

$$b_n = \frac{2}{T} \left[\int_{t_{i1}}^{t_{o1}} (P_3(t)) \sin(\omega nt) dt + \int_{t_{o1}}^{t_{i2}} (v(t) + P_1(t)) \sin(\omega nt) dt + \int_{t_{i2}}^{t_{o2}} (P_3(t)) \sin(\omega nt) dt + \dots \right] \quad (4.11)$$

The complexity of calculating a_n and b_n depends greatly on the form of $v(t)$ as well as how complex the definitions for the time indices T_i and T_o are in order to describe the signal. However, we can arrive at simple and analytical expressions for some common types of input signals.

4.2.2 Example Calculations for a Sinusoidal Input

We will now present some sample calculations of the Fourier series coefficients for the play operator. For a sinusoidal input, we can derive the final expressions for a_n and b_n of the harmonics as

explicit functions of the amplitude and the play radius. Consider a sinusoidal input

$$v(t) = A \sin(\omega t) \quad (4.12)$$

We assume $A \geq r$, which ensures a contraction property like (3.16); thus the steady-state play output is independent of the initial condition. Sinusoidal signals are easy to deal with utilizing the proposed algorithm because they possess only two inflection points per period, which gives the pulse signals $P_1(t)$, $P_2(t)$, and $P_3(t)$ very simple forms. The first step in the computation of (4.10) is to obtain the time instants T_i and T_o ,

$$t_{ij} = \frac{T}{4} + \frac{(j-1)T}{2} \quad (4.13)$$

$$t_{oj} = \frac{T}{2} - \frac{\sin^{-1}(1 - 2r/A)}{\omega} + \frac{(j-1)T}{2} \quad (4.14)$$

We can then write (4.10) as

$$\begin{aligned} a_n = & \frac{2}{T} \left[\int_{t_{i1}}^{t_{o1}} (A - r) \cos(\omega t) dt \right. \\ & + A \int_{t_{o1}}^{t_{i2}} (\sin(\omega t) + r) \cos(\omega t) dt \\ & + \int_{t_{i2}}^{t_{o2}} -(A - r) \cos(\omega t) dt \\ & \left. + A \int_{t_{o2}}^{T+t_{i1}} (\sin(\omega t) - r) \cos(\omega t) dt \right] \quad (4.15) \end{aligned}$$

This results in two types of integrals to evaluate, whose solutions for $n > 1$ are given by

$$\begin{aligned} \int \cos(\omega t) dt &= \frac{\sin(\omega t)}{\omega} \\ \int \sin \omega t \cos(\omega t) dt &= \frac{\cos((n-1)\omega t)}{2\omega(n-1)} - \frac{\cos((n+1)\omega t)}{2\omega(n+1)} \end{aligned} \quad (4.16)$$

Using these integrations combined with (4.13)-(4.15), we can arrive at a closed-form expression for each individual a_n . The expressions for b_n can be derived in a similar way. Furthermore, because of the form for the limits of integration, we can simplify this expression for $n > 1$. In particular, because of the appearance of \sin^{-1} along with half and quarter periods, simplified expressions can be found devoid of any trigonometric functions. For example, when $n = 3$,

$$a_3 = -\frac{4r(8r^3 - 16Ar^2 + 9A^2r - A^3)}{3A^3\pi} \quad (4.17)$$

and

$$b_3 = -\frac{16r(2r^2 - 3Ar + a^2)\sqrt{r(A-r)}}{3A^3\pi} \quad (4.18)$$

Furthermore, we can compute $c_3 = \sqrt{a_3^2 + b_3^2}$, which simplifies to

$$c_3 = \frac{4r(A-r)}{3A\pi} \quad (4.19)$$

while for $n = 5$,

$$c_5 = \frac{4r(A-r)\sqrt{32r^2 - 32Ar + 9A^2}}{15A^2\pi} \quad (4.20)$$

Fig. 4.3 and 4.4 show the calculated values of c_n as functions of the amplitude A and the play radius r respectively. The even harmonics are always zero due to the odd symmetry of the play operator. Fig. 4.3 shows the relative size of harmonic coefficients trending towards zero with

increasing A . Such a behavior is anticipated, because the hysteresis loop for a fixed play radius appears narrower and narrower as the amplitude of the input is increased. From Fig. 4.4, we can see that the relative amplitude of the harmonics varies greatly with the play radius. In particular, for a play radius $r = A/2$, c_3 is five times as large as c_5 , yet c_5 and c_7 are almost identical in size. But for $r = A/4$, c_5 is over three times the value of c_7 . However, from both Fig. 4.3 and 4.4, we see that higher harmonics are always less significant than lower harmonics. Such graphs can serve as a valuable design tool for systems such as that considered in [67], as we will be able to estimate the relative sizes of the harmonics within the system *a priori*.

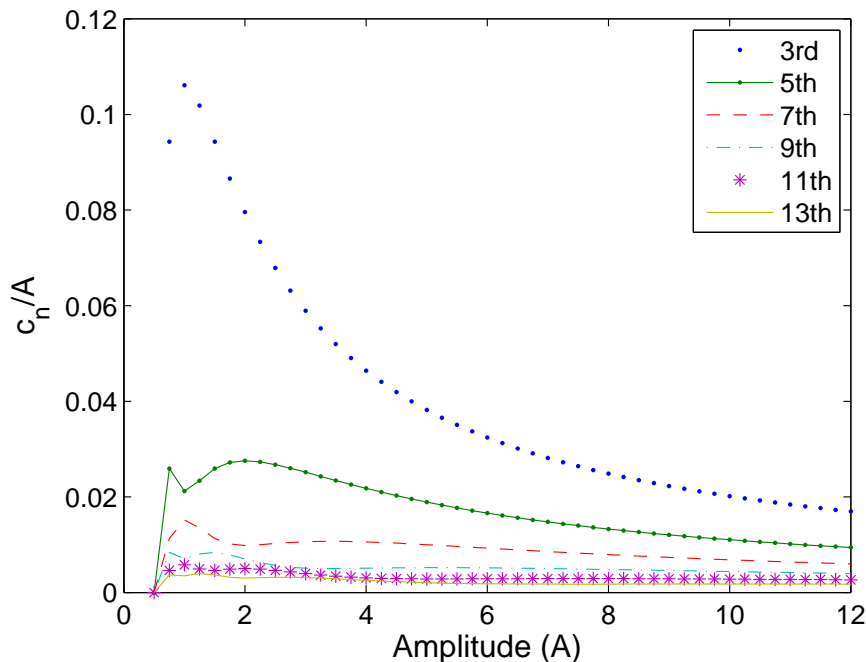


Figure 4.3: Plot of c_n for increasing amplitude A . The play radius is held constant at $r = 0.5$.

4.2.3 Example Calculations for a Raster/Sawtooth Input

We also investigate the application of the algorithm to a raster or sawtooth input signal in combination with a play operator. As we have seen, such inputs are particularly relevant in atomic force

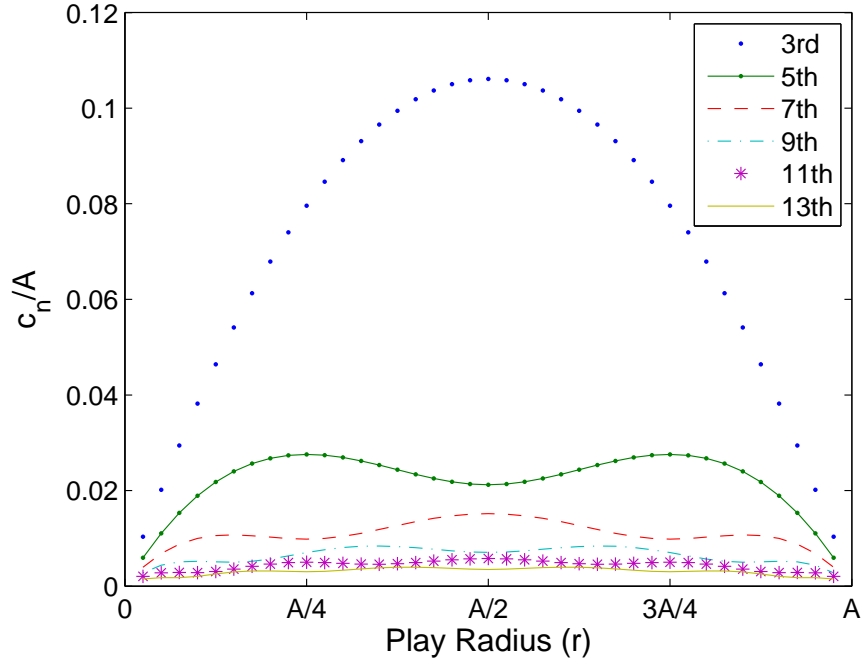


Figure 4.4: Plot of c_n for increasing play radius r . Values of c_n and r are normalized by the input amplitude A .

microscope applications [23]. We can write the input $v(t)$ with amplitude A and period T as

$$v(t) = \begin{cases} \frac{4A}{T}(t - Tn), & \text{if } t \in [-\frac{T}{4} + Tn, \frac{T}{4} + Tn] \\ -\frac{4A}{T}(t - Tn - T/2), & \text{if } t \in [\frac{T}{4} + Tn, \frac{3T}{4} + Tn] \end{cases} \quad (4.21)$$

for $n = 1, 2, \dots$. Similar to sinusoidal inputs, raster signals have only two inflection points per period, allowing us to easily calculate T_i and T_o as

$$t_{ij} = \frac{T}{4} + \frac{(j-1)T}{2}$$

$$t_{oj} = \frac{T(2r+A)}{4A} + \frac{(j-1)T}{2}$$

Using this, we can write (4.28) as

$$\begin{aligned}
a_n = \frac{2}{T} & \left[\int_{t_{i1}}^{t_{o1}} (A - r) \cos(\omega nt) dt \right. \\
& + \int_{t_{o1}}^{t_{i2}} (-4A/T(t - T/2) + r) \cos(\omega nt) dt \\
& + \int_{t_{i2}}^{t_{o2}} -(A - r) \cos(\omega nt) dt \\
& \left. + \int_{t_{o2}}^{T+t_{i1}} (4A/T(t - T) - r) \cos(\omega nt) dt \right] \quad (4.22)
\end{aligned}$$

We can again compute closed-form expressions for both a_n and b_n . In this case, we can derive a simple formula for every c_n ;

$$c_n = \begin{cases} \frac{4A \sqrt{2(\cos(\frac{n\pi T}{a}) + 1)}}{n^2 \pi^2} & n \text{ is odd} \\ 0 & n \text{ is even} \end{cases} \quad (4.23)$$

4.2.4 Harmonic Analysis of a PKP Hysteron

We finally address the application of the proposed algorithm to the PKP hysteron. We will use the same basic setup for reconstructing the output; however, we will need to alter the construction of $u(t)$ due to the form of the PKP operator. In particular, we write

$$u(t) = (-1 + \frac{2(v(t) + P_1(t))}{a})P_2(t) + P_3(t) \quad (4.24)$$

where $P_1(t)$, $P_2(t)$, and $P_3(t)$ are defined by

$$P_1(t) = \begin{cases} -\alpha & \text{sgn}(\dot{v}(t)) > 0 \\ -\beta & \text{sgn}(\dot{v}(t)) < 0 \\ P_1(t^-) & \text{sgn}(\dot{v}(t)) = 0 \end{cases} \quad (4.25)$$

$$P_2(t) = \begin{cases} 0, & t \in [t_{ij}, t_{oj}), \forall j = 1, 2, \dots \\ 1, & t \in [t_{oj}, t_{i(j+1)}), \forall j = 1, 2, \dots \end{cases} \quad (4.26)$$

$$P_3(t) = \begin{cases} -1 + \frac{2(v(t_{ij}) - \alpha)}{a} & \text{sgn}(\dot{v}(t_{ij}^-)) > 0 \text{ and } t \in [t_{ij}, t_{oj}) \\ -1 + \frac{2(v(t_{ij}) - \beta)}{a}, & \text{sgn}(\dot{v}(t_{ij}^-)) < 0 \text{ and } t \in [t_{ij}, t_{oj}) \\ 0, & o.w. \end{cases} \quad (4.27)$$

The definitions above are slightly different from those listed in (4.7)-(4.9). The other major difference between the cases of the PKP hysteron and the play operator is in the definitions of the time instants T_i and T_o . In particular, there are some extra conditions for defining each t_i and t_o . As with the play operator, for the PKP hysteron, t_i can be defined by an inflection point in the input signal $v(t)$. However, we will also use t_i to define times when the input saturates the PKP operator, i.e., t_{ij} is the first time satisfying the condition

$$\dot{v}(t_{ij}) = 0, t_{ij} > t_{o(j-1)}, \text{sgn}(\dot{v}(t_{ij}^-)) \neq \text{sgn}(\dot{v}(t_{ij}^+)),$$

or

$$v(t_{ij}) < \beta, t_{ij} > t_{o(j-1)},$$

or

$$v(t_{ij}) > \alpha + a, t_{ij} > t_{o(j-1)}.$$

Since we have added conditions to the definition of t_i we must also add conditions to the definitions of t_o related to exiting the saturation regions. Therefore, t_{oj} is the first time satisfying the condition

$$|v(t_{ij}) - v(t_{oj})| \geq \alpha - \beta, t_{oj} \geq t_{ij},$$

or

$$\text{sgn}(\dot{v}(t_{ij}^+))v(t_{oj}) < \text{sgn}(\dot{v}(t_{ij}^+))v(t_{ij}), t_{oj} \geq t_{ij},$$

or

$$v(t_{oj}) > \alpha, v(t_{ij}) = \beta, t_{oj} > t_{ij}$$

or

$$v(t_{oj}) < \beta + a, v(t_{ij}) = \alpha + a, t_{oj} > t_{ij}.$$

where the saturation within the PKP hysteron has added the final two conditions. The first two conditions listed serve the same roles they did with the play operator; namely exiting the center “play” region from the opposite or the same side as the signal entered. Once the time indices T_i and T_o are defined, the Fourier coefficients can be calculated in the same manner as they were in

Section 4.2.1, by evaluating the integrals

$$\begin{aligned}
a_n = \frac{2}{T} & \left[\int_{t_{i1}}^{t_{o1}} (P_3(t)) \cos(\omega nt) dt \right. \\
& + \int_{t_{o1}}^{t_{i2}} \left(-1 + \frac{2(v(t) + P_1(t))}{a} \right) \cos(\omega nt) dt \\
& \left. + \int_{t_{i2}}^{t_{o2}} (P_3(t)) \cos(\omega nt) dt + \dots \right] \quad (4.28)
\end{aligned}$$

$$\begin{aligned}
b_n = \frac{2}{T} & \left[\int_{t_{i1}}^{t_{o1}} (P_3(t)) \sin(\omega nt) dt \right. \\
& + \int_{t_{o1}}^{t_{i2}} \left(-1 + \frac{2(v(t) + P_1(t))}{a} \right) \sin(\omega nt) dt \\
& \left. + \int_{t_{i2}}^{t_{o2}} (P_3(t)) \sin(\omega nt) dt + \dots \right] \quad (4.29)
\end{aligned}$$

4.3 Illustration in Controller Design

We will now explore the use of the proposed analysis in the design of controllers like those proposed in Chapter 3. We consider a closed-loop system

$$\begin{aligned}
\begin{bmatrix} \dot{x}(t) \\ \dot{\eta}(t) \end{bmatrix} &= \begin{bmatrix} A & 0 \\ -\mathbf{B}^*c & \mathbf{C}^* \end{bmatrix} \begin{bmatrix} x(t) \\ \eta(t) \end{bmatrix} + \begin{bmatrix} B(u_d + \theta W_r[u_d; W(0)](t)) \\ \mathbf{B}^*y_r(t) \end{bmatrix} \\
u_d(t) &= [K_1, K_2] \begin{bmatrix} x(t) \\ \eta(t) \end{bmatrix} \\
y_r(t) &= a \sin(2\pi t) \quad (4.30)
\end{aligned}$$

where $A = -B = -20\pi$, $c = 1$, $x \in \Re$, and $\theta = 0.1$. This system represents a simplified version of the system considered in Chapter 3. The variable x refers to the state and output of our example plant, while η is the state vector of the servocompensator. The vector \mathbf{B}^* and matrix \mathbf{C}^* are chosen

as a controllable pair where the eigenvalues of \mathbf{C}^* are predetermined harmonics of the reference frequency 2π . As discussed in Chapter 3, an important step in the design of such a controller is the selection of which harmonics will be compensated by the servocompensator. For this simulation, we will consider controllers compensating the (a) the first harmonic, (b) the first and third, and (c) the first, third and fifth harmonics, implying $\eta \in \mathfrak{R}^2$, $\eta \in \mathfrak{R}^4$, and $\eta \in \mathfrak{R}^6$ respectively. The control gains $[K_1, K_2]$ are selected using the well known LQR technique [60], where Q is set to an appropriately sized identity matrix, and $R = 1$. The value of $a = 0.931$ is chosen as the amplitude of u_d necessary for an open-loop sinusoidal input to output a signal of unit amplitude when $r = .5$. We will use two different play radii, $r = A/2$ and $r = A/4$, and investigate the differences in tracking error for the three controllers discussed above.

For such a system, it is desirable to meet a required tracking error target with a minimum-order servocompensator, as increasing the order of the servocompensator increases the computation power needed to accomplish the control task. However, there are no existing guidelines for selecting the order of the compensator, and thus the order of the compensator is the result of a guess-and-check process. Now, based on Fig. 4.4, we are able to make some educated design decisions concerning the order of the servocompensator. When $r = a/2$, we would expect compensating for the third harmonic to have a much greater impact than when $r = a/4$. Likewise, compensating for the fifth harmonic should be more effective when $r = a/4$ as compared to when $r = a/2$.

Fig. 4.5 confirms these expectations. When only the first harmonic is compensated, we notice that the error is significantly higher when $r = a/2$, where the mean tracking error is 4.41×10^{-3} , as compared with $r = a/4$, where the error is 3.26×10^{-3} . A larger play radius can be interpreted as a larger hysteresis effect, which explains this initial difference. Once the third harmonic is compensated, the tracking error in the $r = a/2$ case becomes lower than the $r = a/4$ case, with the

tracking errors being 0.97×10^{-3} against 1.15×10^{-3} . Finally, the situation reverses again when the fifth harmonic is compensated, with the $r = a/4$ case leading $r = a/2$ case, where the errors are 0.43×10^{-3} and 0.61×10^{-3} respectively. These results give us some general guidelines on the selection of the controller order, which can be based on which weights of the PI operator possesses the largest amplitude.

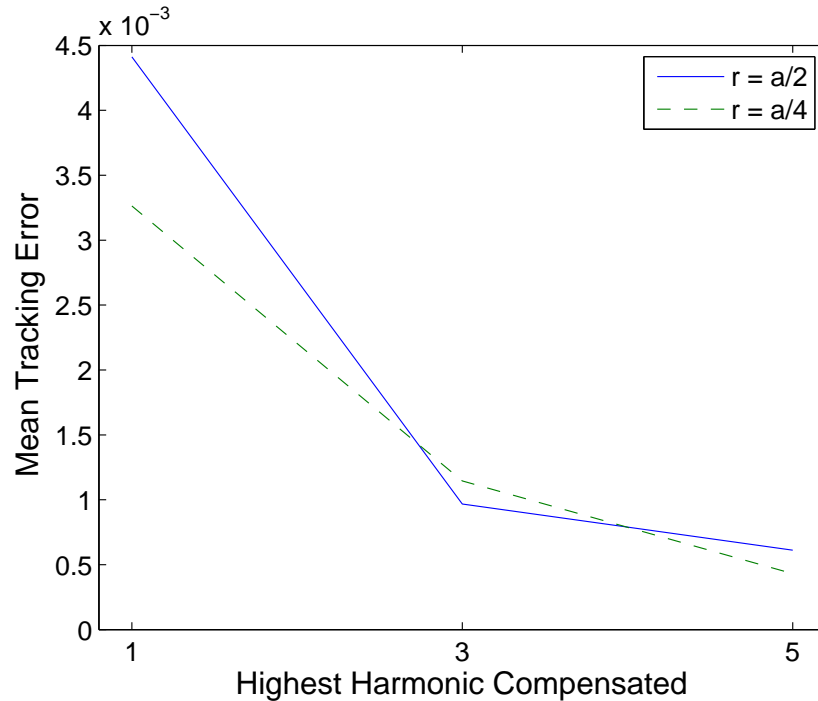


Figure 4.5: Mean tracking errors for various controllers and play radii. Note that the controller gains and structure is unchanged by altering the play radius.

Furthermore, we can use the equations (4.19) and (4.20) to achieve an estimation for precisely how much effect the compensation of each harmonic will have in the closed-loop system. Consider a system (4.30) with $\theta W_r[u_d; W(0)](t)$ replaced by a fictitious external disturbance $\alpha(t)$. Let $\phi(s)$ be the transfer function from $\alpha(t)$ to the tracking error $e(t) = y_r - Cx$, which can be calculated from the state space form of (4.30) [60]. We can then estimate the effect of $\theta W_r[u_d; W(0)](t)$ on the tracking error through the formula $\theta c_i |\phi(j2i\pi)|$, which gives the amplitude of the i th harmonic within $e(t)$ for a given controller defining $\phi(s)$. This formula would be exact, if the play operator

was driven by an open loop sinusoid of amplitude A , instead of $u_d(t)$. However, since the play operator is within the loop, we can expect some error in the estimation.

It is important to note that the weight θ used in these tests is fairly small, with a value of 0.1. Recall that the expressions (4.19) and (4.20) for the Fourier coefficients used in the above simulations were derived under the assumption that the input to the play operator was a pure sinusoidal signal. By having a small θ , the resulting harmonics added to the system by the play operator are fairly small, and thus u_d is fairly close to an ideal pure sinusoid.

Table 4.1: Proposed algorithm's estimations of harmonic amplitude compared with actual values from closed-loop system (4.30). Setup column gives value for play radius used and the harmonic being estimated.

Setup	Predicted	Actual	% Error
3rd, $r = A/2$	$\theta_{c_3} \phi(j6\pi) = 6.77 \times 10^{-3}$	7.00×10^{-3}	-3.3
3rd, $r = A/4$	$\theta_{c_3} \phi(j6\pi) = 5.08 \times 10^{-3}$	5.01×10^{-3}	1.4
5th, $r = A/2$	$\theta_{c_5} \phi(j10\pi) = 1.68 \times 10^{-3}$	1.79×10^{-3}	-6.5
5th, $r = A/4$	$\theta_{c_5} \phi(j10\pi) = 1.29 \times 10^{-3}$	1.35×10^{-3}	-4.7

Table 4.1 compares the estimated harmonic values with the actual values, which are calculated from the simulation tracking error using the Fast Fourier Transform (FFT) function of MATLAB. Four calculations are presented, in which the harmonic being estimated is varied between the 3rd and 5th harmonics and the play radius changed between $r = a/2$ to $r = a/4$. The controller is also changed, compensating the first harmonic when the third harmonic is estimated, and compensating the first and third when the fifth harmonic is estimated. The percent error is calculated using the standard formula: $(\text{Predicted} - \text{Actual}) / \text{Predicted}$. The proposed algorithm is capable of generating a fairly accurate estimation of the amplitude of the harmonics, with the highest error being only 6.5%. This is made more impressive by the fact that there are no other useful tools for such a design problem.

Chapter 5

A Nonlinear Adaptive Servocompensator

5.1 Introduction

In Chapter 3, we demonstrated the effectiveness of servocompensators for solving tracking problems in systems with hysteresis. The design procedure for a servocompensator requires precise knowledge of the reference frequency's internal model to be known *a priori*. However, such detailed knowledge of the reference is not available in advance for many applications. In addition, the controller parameters of the servocompensator must be changed each time the internal model of the reference changes.

Motivated by this, we investigate the use of an adaptive servocompensator, presented in [68], to solve the nanopositioning tracking problem when the frequency is unknown. We will make use of hysteresis inversion to improve the compensator's performance. A high gain stabilizing controller provides robustness to varying loading conditions and other uncertainties in the plant dynamics. We use parameter projection to robustify the method of [68] against a bounded input disturbance. Then, we use similar arguments to that in Chapter 3 to show that, with a well-designed hysteresis inversion, the remaining effect of hysteresis in the steady state can be treated as a periodic exogenous disturbance. This, coupled with the robustness of our adaptive law, permits us to argue that the tracking error is bounded, and its steady state value is related to the size of the exogenous disturbance left over after inversion. We also extend the control method of [68] to accept cases of partially known exosystems.

We confirm our theoretical analysis by experimentation on a commercial nan positioning stage. The performance of the proposed controller is compared to an iterative learning control algorithm [38]. Average tracking error is under 1.8% at 200 Hz for an actuation range of 60% of the stage limit. Tracking results for sawtooth signals are also presented. Since transient behavior is important in practical applications, adaptation convergence speeds are also tested. Adaptation parameters settle within 2 s in response to changes in the reference signal from 75 to 50 to 100 Hz. The controller is shown to be robust to loading conditions from 0 – 20% of maximum load. However, we will also observe that this controller cannot make use of the principles of the MHSC, which motivates us to consider a novel solution for this problem.

5.2 Robust Adaptive Servocompensator Design

5.2.1 System Equations and Error System

Following [68], we consider systems transformable into the normal form,

$$\begin{aligned}
 \dot{z}(t) &= f_0(z(t), x_1(t), w(t)) \\
 \dot{x}_1(t) &= x_2(t) \\
 &\dots \\
 \dot{x}_r(t) &= f_r(z(t), x_1(t), \dots, x_r(t), w(t)) + bu(t) \\
 y(t) &= x_1(t)
 \end{aligned} \tag{5.1}$$

where $x \in \mathfrak{R}^r$ and $z \in \mathfrak{R}^p$. The functions f_0 and f_r are unknown but smooth, with $f_0(0, 0, 0) = 0$, $f_r(0, 0, \dots, 0, 0) = 0$. The constant b is assumed to be positive and bounded. The vector $w \in \mathfrak{R}^\Psi$

is generated by a neutrally stable, linear time-invariant exosystem,

$$\dot{w}(t) = S(\sigma)w(t) \quad (5.2)$$

The matrix $S(\sigma)$ is in general unknown, depending on the unknown parameters $\sigma \in \mathfrak{R}^\Sigma$.

Assumption 6 *The parameter σ is confined to a known compact set κ_σ , which subsequently confines $S(\sigma)$ to a known compact set κ_w .*

The tracking error is given by

$$e(t) = x_1(t) - q(w(t)) \quad (5.3)$$

where $q(w)$ is the reference signal to be tracked. The objective of our control design is to minimize the tracking error e . It should be noted that it is common for the exosystem to be partially known. For example, many reference trajectories will contain a constant bias term. The differences between the partially known case and the fully unknown case will be pointed out at the end of our analysis. Following [57], we make the following assumption to ensure that the tracking problem is well-posed.

Assumption 7 *For every $S \in \kappa_w$, there exists a globally defined solution $\zeta_\sigma(w)$ to the equation*

$$\frac{\partial \zeta_\sigma(w)}{\partial w} S w = f_0(\zeta_\sigma(w), q(w), w) \quad (5.4)$$

This assumption and the triangular structure of (5.1) ensure the existence of a unique, globally defined solution $(z, x, u) = (\zeta_\sigma(w), \vartheta_\sigma(w), c_\sigma(w))$ to the system (5.1), given by

$$\vartheta_{\sigma}(w(t)) = \begin{pmatrix} q(w(t)) \\ L_{S(\sigma)w}q(w(t)) \\ \dots \\ L_{S(\sigma)w}^{r-1}q(w(t)) \end{pmatrix}$$

$$c_{\sigma}(w(t)) = \frac{1}{b} [L_{S(\sigma)w}^r q(w(t)) - f_r(\zeta_{\sigma}(w(t)), \vartheta_{\sigma}(w(t)), w(t))]$$

where $L_{\rho}^l g(\cdot)$ represents the l th Lie derivative [64] of $g(\cdot)$ with respect to ρ .

Assumption 8 *There exists a $j \in \mathbb{N}$, $j \geq \Psi$ and a vector of real numbers $[a_0(\sigma), a_1(\sigma), \dots, a_{j-1}(\sigma)]$ such that the identity*

$$\begin{aligned} L_{S(\sigma)w}^j c_{\sigma}(w(t)) &= a_0(\sigma) c_{\sigma}(w(t)) + a_1(\sigma) L_{S(\sigma)w} c_{\sigma}(w(t)) \\ &+ \dots + a_{j-1}(\sigma) L_{S(\sigma)w}^{j-1} c_{\sigma}(w(t)) \end{aligned}$$

holds for all $(w, \sigma) \in \mathfrak{R}^{\Psi \times \Sigma}$.

Assumption 8 is required to ensure that the necessary control $c_{\sigma}(w)$ can be generated by our internal model controller. Specifically, this implies that there exists a mapping

$$\tau_{\sigma}(w(t)) = \begin{pmatrix} c_{\sigma}(w(t)) \\ L_{S(\sigma)w} c_{\sigma}(w(t)) \\ \dots \\ L_{S(\sigma)w}^{j-1} c_{\sigma}(w(t)) \end{pmatrix}$$

which satisfies

$$\begin{aligned} L_{S(\sigma)w} \tau_\sigma(w(t)) &= \Phi(\sigma) \tau_\sigma(w(t)) \\ c_\sigma(w(t)) &= \Gamma \tau_\sigma(w(t)) \end{aligned} \quad (5.5)$$

Here $\Phi(\sigma) \in \mathfrak{R}^{j \times j}, \Gamma \in \mathfrak{R}^{1 \times j}$ and $(\Phi_\sigma, \Gamma_\sigma)$ is an observable canonical form whose characteristic equation is solved by the vector $[1, -a_{j-1}(\sigma), \dots, -a_1(\sigma), -a_0(\sigma)]$. Furthermore, the spectrum of $\Phi(\sigma)$ contains all the distinct eigenvalues of the exosystem (5.2), and those of any harmonics of the exosystem generated by the system (5.1). Because of this, we will refer to the pair $(\Phi(\sigma), \Gamma)$ as the extended exosystem. The above functions $(\zeta_\sigma(w), \vartheta_\sigma(w), c_\sigma(w), \tau_\sigma(w))$ represent the states of the plant, control signal, and extended exosystem on a zero error manifold. Using these functions we will now form the error system, which will be used in our analysis and controller design. The global change of coordinates

$$\tilde{z}(t) = z(t) - \zeta_\sigma(w(t)), \tilde{x}(t) = x - \vartheta_\sigma(w(t)) \quad (5.6)$$

places (5.1) into the error system form

$$\begin{aligned} \dot{\tilde{z}}(t) &= \tilde{f}_0(\tilde{z}(t), \tilde{x}_1(t), w(t), \sigma) \\ \dot{\tilde{x}}_1(t) &= \tilde{x}_2(t) \\ &\dots \\ \dot{\tilde{x}}_r(t) &= \tilde{f}_r(\tilde{z}(t), \tilde{x}_1(t), \dots, \tilde{x}_r(t), w(t), \sigma) + b[u(t) - c_\sigma(w(t))] \\ e(t) &= \tilde{x}_1(t) \end{aligned} \quad (5.7)$$

Assumption 9 *The zero dynamics of the system (5.7),*

$$\dot{\tilde{z}}(t) = \tilde{f}_0(\tilde{z}(t), \mathbf{0}, w(t), \boldsymbol{\sigma})$$

are exponentially stable, with Lyapunov function $V_1 = \tilde{z}' P_a \tilde{z}$, where P_a is positive definite.

As a final preliminary, we will make another change of coordinates

$$\boldsymbol{\theta}(t) = \tilde{x}_r(t) + k^r b_0 \tilde{x}_1(t) + k^{r-1} b_1 \tilde{x}_2(t) + \cdots + k b_{r-2} \tilde{x}_{r-1}(t) \quad (5.8)$$

where $k > 0$ is a constant design constant, and the polynomial $\lambda^{r-1} + b_{r-2} \lambda^{r-2} + \cdots + b_1 \lambda + b_0$ is Hurwitz. $\boldsymbol{\theta}$ represents a modified tracking error we will use in our control design. This allows us to place the system in the form,

$$\dot{\tilde{z}}_a(t) = F_a(\tilde{z}_a(t), w(t), \boldsymbol{\sigma}, k) + G_a \boldsymbol{\theta}(t) \quad (5.9)$$

$$\dot{\boldsymbol{\theta}}(t) = \phi(\tilde{z}_a(t), \boldsymbol{\theta}(t), w(t), \boldsymbol{\sigma}, k) + b[u - c_\sigma(w(t))] \quad (5.10)$$

where

$$\tilde{z}_a(t) = [\tilde{z}(t), \tilde{x}_1(t), \cdots, \tilde{x}_{r-1}(t)]'$$

$$F_a(\tilde{z}_a(t), w(t), \boldsymbol{\sigma}, k) = \begin{pmatrix} \tilde{f}_0(\tilde{z}(t), \tilde{x}_1(t), w(t), \boldsymbol{\sigma}) \\ \tilde{x}_2(t) \\ \cdots \\ -k^{r-1} b_0 \tilde{x}_1(t) - k^{r-1} b_1 \tilde{x}_2(t) - \cdots - k b_{r-2} \tilde{x}_{r-1}(t) \end{pmatrix}$$

$$G_a = (0, \cdots, 0, 1)'$$

and

$$\begin{aligned}\phi(\tilde{z}_a(t), \theta(t), w(t), \sigma, k) = & \tilde{f}_r(\tilde{z}(t), \tilde{x}_1(t), \dots, \tilde{x}_r(t), w(t), \sigma) \\ & + k^r b_0 \tilde{x}_2(t) + k^{r-1} b_1 \tilde{x}_3(t) + \dots + k b_{r-2} \tilde{x}_r(t)\end{aligned}$$

with \tilde{x}_r replaced by $\theta - k^r b_0 \tilde{x}_1 - k^{r-1} b_1 \tilde{x}_2 - \dots - k b_{r-2} \tilde{x}_{r-1}$.

5.2.2 Controller Design

Our control signal $u(t)$ is composed of two components. First, we use a stabilizing controller, $u_{\text{st}} = -K\theta$, $K > 0$, which will make an invariant manifold of the system globally attractive. Then we will use an internal model controller to ensure that on the invariant manifold the tracking error is zero (in the absence of disturbances). In preparation for adaptation, we design our internal model in the canonical form [69]

$$\dot{\xi}(t) = (F + G\psi_\sigma)\xi(t) \quad (5.11)$$

where $\xi \in \mathfrak{R}^j$ and the pair (F, G) is controllable, with F Hurwitz. $\psi_\sigma \in \mathfrak{R}^{1 \times j}$ defines a state feedback that sends the eigenvalues of $(F + G\psi_\sigma)$ to the eigenvalues of the extended exosystem (5.5). The work of [69] ensures that the Sylvester equation,

$$M_\sigma \Phi(\sigma) - F M_\sigma = G \Gamma \quad (5.12)$$

has a unique, nontrivial solution M_σ . We can now define the vector ψ_σ from the expression $M_\sigma \Phi(\sigma) M_\sigma^{-1} = F + G\psi_\sigma$, implying $\psi_\sigma = \Gamma M_\sigma^{-1}$. The implemented internal model controller

is driven by the error term θ ,

$$\begin{aligned}\dot{\xi}(t) &= (F + G\psi_\sigma)\xi(t) + N\theta(t) \\ u_{\text{im}}(t) &= \psi_\sigma \xi(t)\end{aligned}\tag{5.13}$$

where the vector N will be defined momentarily. The composite control $u(t)$ is then

$$u(t) = u_{\text{st}}(t) + u_{\text{im}}(t) = -K\theta(t) + \psi_\sigma \xi(t)\tag{5.14}$$

We now can see that the extended exosystem (5.5) is immersed into the internal model controller (5.11), with an immersion map defined as

$$\bar{\tau}_\sigma(w) = M_\sigma \tau_\sigma(w)\tag{5.15}$$

satisfying the relations,

$$\begin{aligned}\frac{\partial \bar{\tau}_\sigma}{\partial w} S(\sigma)w &= M_\sigma \Phi M_\sigma^{-1} \bar{\tau}_\sigma(w) \\ c_\sigma(w) &= \Gamma \tau_\sigma(w) \\ &= \psi_\sigma \bar{\tau}_\sigma(w)\end{aligned}$$

The vector N will be designed to render a kind of error coordinate,

$$\xi(t) \rightarrow \chi(t) = \xi(t) - \bar{\tau}_\sigma(w(t)) - \frac{1}{b}G\theta(t)$$

independent of the stabilizing gain K . As discussed in [68], the term $\xi - \bar{\tau}_\sigma$ represents the error

between the current states of the internal model controller and desired states of the controller on the zero error manifold. Including the term $-\frac{1}{b}\theta$ simplifies the resulting equation for χ , which is

$$\dot{\chi}(t) = F\chi(t) + \left(\frac{1}{b}FG + N + GK\right)\theta(t) - \frac{1}{b}G\phi(\tilde{z}_a(t), \theta(t), w(t), \sigma, k) \quad (5.16)$$

We can now simplify our analysis by rendering this equation independent of K by setting $N = -KG$. This allows us to represent the closed loop system as (see [68] for details),

$$\dot{\chi}(t) = F\chi(t) + \frac{1}{b}[FG\theta(t) - G\phi(\tilde{z}_a(t), \theta(t), w(t), \sigma, k)] \quad (5.17)$$

$$\dot{\tilde{z}}_a(t) = F_a(\tilde{z}_a(t), w(t), \sigma, k) + G_a\theta(t) \quad (5.18)$$

$$\dot{\theta}(t) = \phi(\tilde{z}_a(t), \theta(t), w(t), \sigma, k) + b\psi_\sigma\chi(t) + (\psi_\sigma G - bK)\theta(t) \quad (5.19)$$

5.2.3 Robust Adaptive Law

We now consider the case where the internal model of the exosystem (5.2) is unknown. An adaptive law is proposed for the vector ψ_σ , which we will robustify to matched disturbances via parameter projection and show that the tracking error will be bounded. Replacing ψ_σ by $\hat{\psi}_\sigma$ and setting $\tilde{\psi} = (\hat{\psi}_\sigma - \psi_\sigma)$, equations (5.17) - (5.19) become

$$\dot{\chi}(t) = F\chi(t) + 1/b[FG\theta(t) - G\phi(\tilde{z}_a(t), \theta(t), w(t), \sigma, k)] \quad (5.20)$$

$$\dot{\tilde{z}}_a(t) = F_a(\tilde{z}_a(t), w(t), \sigma, k) + G_a\theta(t) \quad (5.21)$$

$$\begin{aligned} \dot{\theta}(t) = & \phi(\tilde{z}_a(t), \theta(t), w(t), \sigma, k) + b\psi_\sigma\chi(t) + (\psi_\sigma G - bK)\theta(t) \\ & + b\tilde{\psi}\xi(t) \end{aligned} \quad (5.22)$$

The adaptive law takes the form

$$\dot{\tilde{\psi}}(t) = \varphi(\xi(t), \theta(t)) \quad (5.23)$$

where we will use a Lyapunov argument to define $\varphi(\xi, \theta)$. The system (5.20)-(5.23) will be referred to as our nominal system. We will now seek a Lyapunov function for the closed-loop system. First, consider the case where ψ_σ is known, and no adaptation is needed. Next, define P from the Lyapunov equation $PF + F'P = -I$, where I denotes an appropriately dimensioned identity matrix. It can now be shown, assuming a high enough gain K and high enough κ , the derivative of the function

$$W(\chi, \tilde{z}_a, \theta) = \chi'(t)P\chi(t) + \kappa \tilde{z}_a'(t)P_a \tilde{z}_a(t) + \frac{1}{2}\theta^2(t) \quad (5.24)$$

satisfies the expression $\dot{W} \leq -\lambda \|(\chi, \tilde{z}_a, \theta)\|^2$, where λ is positive. Throughout the paper, $\|\cdot\|$ denotes the Euclidean norm. This implies that $(\chi, \tilde{z}_a, \theta) = (0, 0, 0)$ is exponentially stable.

Now, consider the closed loop system (5.20)-(5.23). We modify W to be

$$\bar{W}(\chi, \tilde{z}_a, \theta, \tilde{\psi}) = W(\chi, \tilde{z}_a, \theta) + \frac{b}{2}\tilde{\psi}'(t)\gamma^{-1}\tilde{\psi}(t), \gamma > 0 \quad (5.25)$$

Taking the time derivative of \bar{W} yields

$$\dot{\bar{W}} \leq -\lambda \|(\chi, \tilde{z}_a, \theta)\| + b\tilde{\psi}(t)[\theta(t)\xi(t) + \gamma^{-1}\varphi(\xi(t), \theta(t), \tilde{\psi}(t))] \quad (5.26)$$

We now can define the adaptive law by letting

$$\varphi(\xi, \theta, \tilde{\psi}) = -\gamma\theta(t)\xi(t) \quad (5.27)$$

where $\gamma > 0$ is the adaptation gain. This implies that the vector $\tilde{\psi}$ converges to some $\tilde{\psi}^*$, and that the tracking error $e(t) \rightarrow 0$ as $t \rightarrow \infty$.

Remark 4 *If the vector ξ can be shown to satisfy a persistent excitation condition [43], in addition to the error convergence, it can be shown that $\tilde{\psi} \rightarrow 0$ as $t \rightarrow \infty$.*

Now, we will allow a matched disturbance α to be added to the system. This changes the closed-loop system into

$$\dot{\chi}(t) = F\chi(t) + 1/b[FG\theta(t) - G\phi(\tilde{z}_a(t), \theta(t), w(t), \sigma, k)] - G\alpha(t) \quad (5.28)$$

$$\dot{\tilde{z}}_a(t) = F_a(\tilde{z}_a(t), w(t), \sigma, k) + G_a\theta(t) \quad (5.29)$$

$$\begin{aligned} \dot{\theta}(t) = & \phi(\tilde{z}_a(t), \theta(t), w(t), \sigma, k) + b\psi_\sigma\chi(t) + (\psi_\sigma G - bK)\theta(t) \\ & + b\tilde{\psi}\xi(t) + b\alpha(t) \end{aligned} \quad (5.30)$$

$$\dot{\tilde{\psi}}(t) = -\gamma\theta(t)\xi(t) \quad (5.31)$$

To robustify the adaptive law, we will use parameter projection to constrain the estimate $\hat{\psi}_\sigma$ to a convex, compact set. This will allow us to deal with the extra terms resulting from the disturbance α that will appear in (5.26). Our analysis here is adapted from the work in [70].

Assumption 10 *The initial conditions of (5.20)-(5.23), given as $(\chi(0), \tilde{z}_a(0), \theta(0))$, belong to a known compact set $\{X_0, \tilde{Z}_0, \Theta_0\}$*

Because we have assumed $S \in \kappa_\sigma$, there exists some set Ω such that $\psi_\sigma \in \Omega$. We can then

constrain our estimation $\hat{\psi}_\sigma$ to a convex, compact set $\Omega_\delta \supset \Omega$. Let $c_1 = \max(W(\chi, \tilde{z}_a, \theta))$, where $(\chi, \tilde{z}_a, \theta) \in \{X_0, \tilde{Z}_0, \Theta_0\}$, and

$$c_2 = \max_{\psi_\sigma \in \Omega, \hat{\psi}_\sigma \in \Omega_\delta} \frac{1}{2} (\hat{\psi}_\sigma - \psi_\sigma)^T \gamma^{-1} (\hat{\psi}_\sigma - \psi_\sigma) \quad (5.32)$$

Let $c_3 > c_1 + c_2$, which we use to define the set $E \triangleq \{(\chi, \tilde{z}_a, \theta) : W(\chi, \tilde{z}_a, \theta) < c_3\}$. We now aim to show that trajectories starting in the set E stay in this set $\forall t > 0$. Let $d = \max \|\alpha(t)\|$. The derivative of \bar{W} can be written as

$$\dot{\bar{W}} \leq -\lambda \|(\chi, \tilde{z}_a, \theta)\|^2 + b\theta(t)d + \chi(t)d \quad (5.33)$$

Finally, we define the constant

$$k_1 \triangleq \max_{(\theta, \chi) \in E} (b_c \theta + \chi) \quad (5.34)$$

We can now show that there exists a constant ν such that

$$\dot{\bar{W}} \leq -\nu \bar{W} + k_1 d + c_2 \quad (5.35)$$

We can now see that there exists a $d^* \triangleq \nu(-c_2 + c_3)/k_1$, $\dot{\bar{W}} < 0$ on $\{\bar{W} = c_3 : \hat{\psi}_\sigma \in \Omega_\delta\}$. Thus the set $\{\bar{W} \leq c_3 : \hat{\psi}_\sigma \in \Omega_\delta\}$ is positively invariant for all $d < d^*$. This implies that the trajectories are trapped inside the set $E \cap \Omega_\delta$, which implies that all states are bounded. Also, from (5.35) we can see that the tracking error is on the order $O(d + 1/(\gamma))$.

Remark 5 *If γ is replaced by a matrix Y , the above theory also holds, with tracking error on the order $O(d + 1/|\lambda_{\min}(Y)|)$, where $\lambda_{\min}(\cdot)$ denotes the minimum eigenvalue.*

5.2.4 Partially Known Exosystem

We will briefly consider the case where the exosystem is partially known. To handle this, we will split (5.13) into two subsystems, related to the known and unknown portions of the exosystem.

The subsystems form the internal model controller

$$\begin{bmatrix} \xi_0(t) \\ \xi_1(t) \end{bmatrix} = \begin{bmatrix} F_0 + G_0\psi_0 & 0 \\ 0 & F_1 + G_1\psi_1 \end{bmatrix} \begin{bmatrix} \xi_0(t) \\ \xi_1(t) \end{bmatrix} + \begin{bmatrix} N_0 \\ N_1 \end{bmatrix} \theta(t) \quad (5.36)$$

$$u_{\text{im}}(t) = \psi_0 \xi_0(t) + \psi_1 \xi_1(t) \quad (5.37)$$

The eigenvalues of $F_0 + G_0\psi_0$ consist of the known portion of the exosystem (5.2). The existence of (ψ_0, ψ_1) can be shown by partitioning the matrix $\Psi(\sigma)$ into known and unknown portions, and then applying the results of [69] to each portion. To simplify our notation, we define

$$F^* \triangleq \begin{bmatrix} F_0 & 0 \\ 0 & F_1 \end{bmatrix}, G^* \triangleq \begin{bmatrix} G_0 & 0 \\ 0 & G_1 \end{bmatrix}, N^* \triangleq \begin{bmatrix} N_0 & 0 \\ 0 & N_1 \end{bmatrix}$$

We now determine the vectors N_0 and N_1 using equation (5.16), which becomes

$$\begin{bmatrix} \dot{\chi}_0(t) \\ \dot{\chi}_1(t) \end{bmatrix} = F^* \chi(t) + \left(\frac{1}{b} F^* G^* + N^* + G^* K\right) \theta(t) - \frac{1}{b} G^* \phi(\tilde{z}_a(t), \theta(t), w(t), \sigma, k) \quad (5.38)$$

In order to make the above equation independent of K , we can set $N_0 = G_0\theta$, $N_1 = G_1\theta$. We then design the adaptive law in the same way with $\psi \triangleq (\psi_0, \psi_1)$, and use the same Lyapunov functions to show stability and parameter convergence. However, we assume that the value of ψ_0 is known in advance. Thus, (5.26) will be independent of ψ_0 and χ_0 , and the adaptation law will only need to effect ψ_1 . For the remainder of our analysis, we will assume that the exosystem is completely

unknown.

5.3 Analysis of Closed-Loop System including Hysteresis

Having established robustness to disturbances outside those generated by the exosystem (5.2), we will now consider the scenario where the input to the system (5.1) is the output of a hysteresis operator. We now include the hysteresis operator (2.3) into our description of the closed-loop system. After using (2.3) and (2.12) together with (5.20) to (5.23) and (5.27), the complete closed-loop system becomes

$$\begin{aligned}\dot{\chi}(t) = & F\chi(t) + 1/b_c[FG\theta(t) - G\phi(\tilde{z}_a(t), \theta(t), w(t), \sigma, k)] \\ & - G\tilde{\theta}_h'W(t)\end{aligned}\tag{5.39}$$

$$\dot{\tilde{z}}_a(t) = F_a(\tilde{z}_a(t), w(t), \sigma, k) + G_a\theta(t)\tag{5.40}$$

$$\begin{aligned}\dot{\theta}(t) = & \phi(\tilde{z}_a(t), \theta(t), w(t), \sigma, k) + b\psi_\sigma\chi(t) + (\psi_\sigma G - b_c K)\theta(t) \\ & + b_c\tilde{\psi}(t)\zeta(t) + b\tilde{\theta}_h'W(t)\end{aligned}\tag{5.41}$$

$$\dot{\tilde{\psi}}(t) = -\Gamma\theta(t)\zeta(t)\tag{5.42}$$

$$W(t) = \mathcal{W}[u_d; W(0)](t) \triangleq \mathcal{P} \circ \hat{\Gamma}^{-1}[u_d; W(0)](t)\tag{5.43}$$

Note that the above system without hysteresis is identical to the system discussed in [68]. Since that system was shown to admit an asymptotically stable periodic solution, the above system fits into the class of systems discussed in [63]. We can now use this work to show that there is an asymptotically stable periodic solution to the system (5.39) - (5.43), and that this solution is close to the original solution assuming that the inversion error $\tilde{\theta}_h'W$ is small. This argument follows identically to that presented in Chapter 3, and allows us to prove the existence of an asymptotically

stable periodic solution.

5.4 Experimental Results

We will now test the performance of our method via experimentation on our commercial nanopositioning stage shown in Fig. 3.3. Due to the increased complexity of this controller, we were required to reduce the order of the system model considered to a second order linear system, placed in the normal form,

$$\dot{x}(t) = \begin{bmatrix} 0 & 1 \\ -1.795 \times 10^8 & -5696.88 \end{bmatrix} x(t) + \begin{bmatrix} 0 \\ 1.063 \times 10^9 \end{bmatrix} u(t)$$

$$y(t) = [1, 0]x(t)$$

Even doing this, the sampling rate of the system was reduced to 10 kHz, as opposed to the 20 kHz rate used in Chapter 3. Since the positioner can be faithfully modeled without zero dynamics, the error system state \tilde{x} is defined in the usual way as $\tilde{x}_1 = x_2 - y_r(t)$, $\tilde{x}_2 = x_2 - \dot{y}_r(t)$, where $y_r(t)$ is the reference trajectory. The modified error term (5.8) is chosen as $\theta \triangleq \tilde{x}_1 + \tilde{x}_2$. This makes $\tilde{z}_a = \tilde{x}_1$ and $\phi(\tilde{z}_a, \theta, w, p, k) = -1.795 \times 10^8 \tilde{x}_1 - 5696.88(\theta - \tilde{x}_1) + \theta - \tilde{x}_1$. Since all reference trajectories included a bias term, an integral type controller was included into the design scheme in accordance with the results of Section 5.3. The controller's design parameters were chosen as

$$F_0 = -200, G_0 = 200, \psi_0 = 1$$

$$F_1 = \begin{bmatrix} -500 & 500 \\ 0 & -500 \end{bmatrix}, G_1 = \begin{bmatrix} 0 \\ 10 \end{bmatrix}$$

$$K = 0.01, \gamma = -10$$

The vector $\psi = (\psi(1), \psi(2))$ will be our adaptation state, and it is constrained to the convex set

$$\Omega_\delta = \{-200 \leq \psi(i) \leq 200, i = 1, 2\}$$

Note that the above design implies that the servocompensator accommodates a single harmonic only. To facilitate the state feedback design of the above controller, a high gain observer was used to estimate the error states, and thus θ . This observer is linear, and its implementation is described in [68].

There are three features of our control method that we will test with our experiments. First, we will investigate the raw tracking performance for sinusoid and sawtooth reference signals, and compare our results to the iterative control algorithm of [38]. The two relative error metrics we use for comparison are the mean tracking error, computed by taking the mean of $|e(t)|$ over one period of the reference, and peak tracking error, $\max|e(t)|$, once the system has reached steady state. Errors are presented as percentages of the reference amplitude, except in the figures where the actual error in μm is shown. Second, we examine the adaptation performance for changing reference signals. Finally, we show robustness of the method to changing loading conditions by adding a weight to the stage.

Table 5.1 shows the tracking performance for both the adaptive servocompensator (ASC) and iterative learning control (ILC), which was implemented using the model above. For this study, all reference signals had an amplitude of $20 \mu\text{m}$ and bias of $25 \mu\text{m}$. Two samples of the error

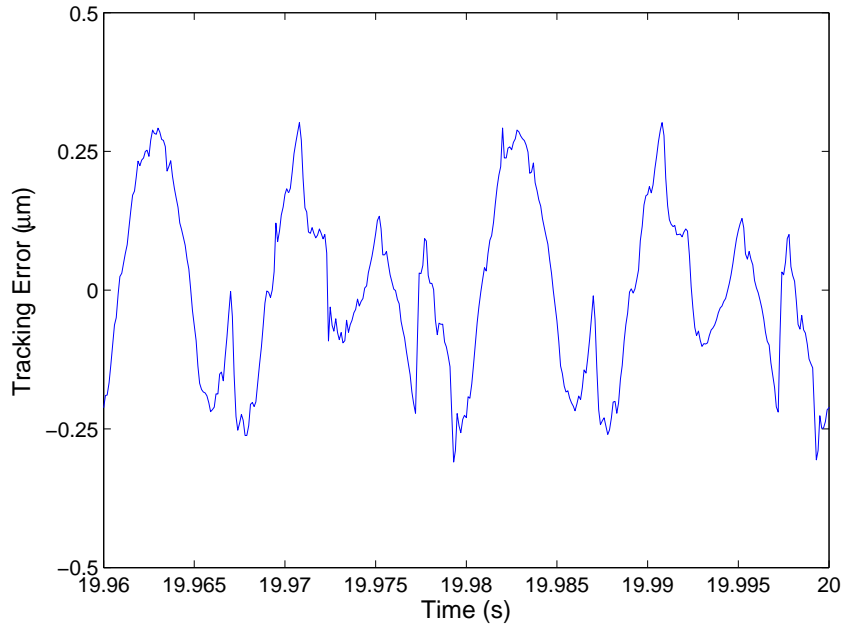


Figure 5.1: Tracking error for a 50 Hz reference signal, with two periods shown. Tracking range is $\pm 20 \mu\text{m}$.

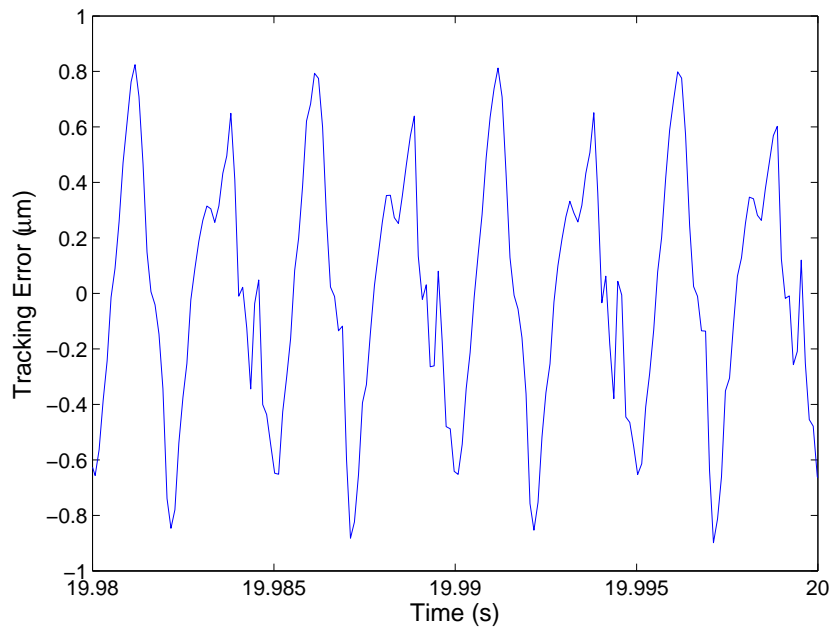


Figure 5.2: Tracking error for a 200 Hz reference signal with four periods shown. Tracking range is $\pm 20 \mu\text{m}$.

signals from the ASC are shown in Figures 5.1 and 5.2. For sinusoids, the performance of the two controllers is comparable. However, the ASC design has several other practical advantages over ILC. ILC algorithms typically require very accurate plant models to ensure convergence, whereas the ASC requires only limited plant knowledge to select the stabilizing gain K . The reference signal can be changed online for the ASC, and after only a short transient the error converges to its steady state value in Table 5.1. Changing the control signal in ILC even slightly requires rerunning the entire learning algorithm. Also, ILC algorithms are difficult to implement on standard control hardware. ILC is well suited to tracking a large bandwidth signal like a sawtooth, so its lead in this test is expected.

Table 5.1: Tracking error in percent of reference amplitude for adaptive servocompensator (ASC) and iterative learning (ILC) controllers

	ASC		ILC	
	Mean Error	Peak Error	Mean Error	Peak Error
Sine, 5 Hz	0.051%	0.31%	0.25%	1.725%
Sine, 25 Hz	0.3405%	0.925%	0.314%	2.091%
Sine, 50 Hz	0.6555%	1.599%	0.7735%	3.95%
Sine, 100 Hz	1.242%	2.96%	.902%	2.45%
Sine, 200 Hz	1.713%	3.75%	2.05%	6%
Sawtooth, 5hz	0.3285%	2.423%	0.1%	0.818%

Next, we test the convergence speed of the adaptive law. Figures 5.3 and 5.4 show the convergence of the tracking error and the parameter $\psi(1)$. The parameter $\psi(2)$ had the same value for each reference signal due to the structure of the pair (F, G) , so its plot was omitted from the presentation. Note, however, that this parameter was still subject to adaptation, and was not assumed to be known. Also, due to some extra data recording that was needed in this experiment, the sampling frequency was lowered from 10 kHz to 9 kHz. This caused the tracking error for the 100 Hz case to increase as compared to the values in Table 5.1. At $t = 1$ s, the controller is turned on and tracks a reference signal of $20 \sin(2\pi 75 t) + 25 \mu\text{m}$. At $t = 15$ s, the reference switches to 10

$\sin(2\pi 50 t)+30 \mu\text{m}$. Finally, at $t = 35\text{s}$, the reference switches to $20 \sin(2\pi 100 t)+25 \mu\text{m}$.

For each reference signal, the parameter error $\tilde{\psi}$ settled to near zero in under two seconds. Tracking error convergence was slightly longer; however this was primarily due to the integral controller portion not responding quickly. Also note that the initial condition of $\psi(1)$ was not close to the final value, confirming the global convergence of the adaptive algorithm. One feature we noted in our experiments is that the adaptive law's convergence speed is dependent on the frequency of the reference. For a slower signal, convergence speeds go down, and the adaptive law takes longer to converge. There are many possible reasons for this, but the most probable is that the integral controller is able to reduce the tracking error at low frequencies to a very small signal. Since the adaptation is driven by the modified tracking error θ , this would result in slower convergence.

Finally, we examine the robustness of our controller to loading conditions. We loaded our actuator with 20 g, 40 g, and 100 g, then ran the system with a reference of $20 \sin(2\pi 10t)+25\mu\text{m}$. The results are presented in Table 5.2. The tracking error was near identical for each load, even in the 100 g case. Note that this corresponds to a change from 0% to 20% of the maximum load allowed for the nanopositioner.

Table 5.2: Tracking error under varying loading conditions

Loading Condition	Mean Error	Peak Error
No Load	0.0817%	0.34%
20g Load	0.0818%	0.34%
40g Load	0.0819%	0.35%
100g Load	0.0821%	0.35%

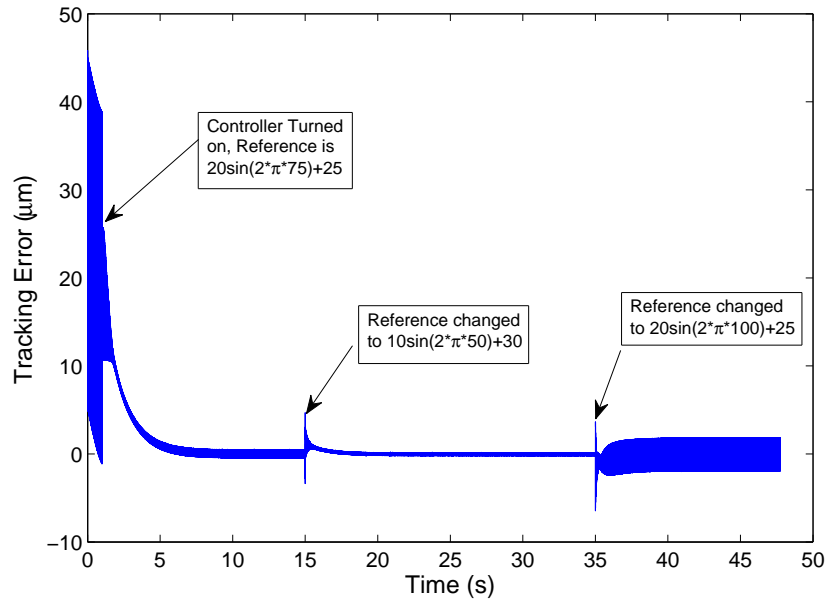


Figure 5.3: Tracking error under a changing reference signal.

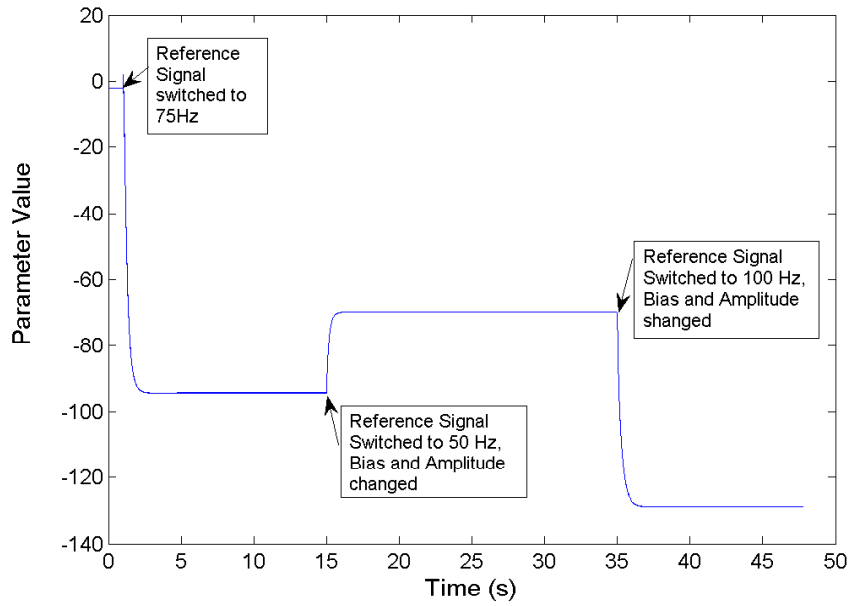


Figure 5.4: Trajectory of $\psi(1)$ under a changing reference signal.

5.5 Shortcomings of the Nonlinear Adaptive Servocompensator in Nanopositioning Problems

The results presented in the previous section clearly indicate that the proposed nonlinear adaptive servocompensator can perform satisfactorily in nanopositioning applications. However, there are some clear drawbacks to the proposed method. In particular, the concept of the multi-harmonic servocompensator could not be applied to this adaptive servocompensator design. As we discussed in the experimental results of Section 5.4, the internal model controller (5.13) was limited to second order. Following the theoretical results of Section 5.3, we attempted to increase the order of this controller in order to compensate for the harmonics generated by hysteresis.

Fig. 5.5 presents the experimental results of this extension. The adaptation variables quickly entered a neighborhood of values that allowed the controller to compensate for the reference trajectory. After this transient, the adaptation variables began to slowly drift. After a lengthy period of slow drift, a series of peaking events, shown in Fig. 5.5, occurred in the adaptation variables. The peaking events in the adaptation variables resulted in a large undesirable transient in the behavior of the system associated with a loud screeching noise emitted by the nanopositioner, and the experiment was immediately terminated. In addition, the adaptation variables were not able to reach a point where any harmonics of the hysteresis could be compensated.

Following this failure, we conducted additional simulation tests on a system without hysteresis, using a small-amplitude sinusoidal matched disturbance possessing a different frequency than that of the reference. A similar phenomenon was observed in these tests. Therefore, we conclude that the peaking events observed in Fig. 5.5 were caused by the fact that the harmonics induced by hysteresis are relatively small. Indeed, the authors of [71] investigated a similar problem theoretically, and discovered that the signals to be compensated by the adaptive servocompensator were required

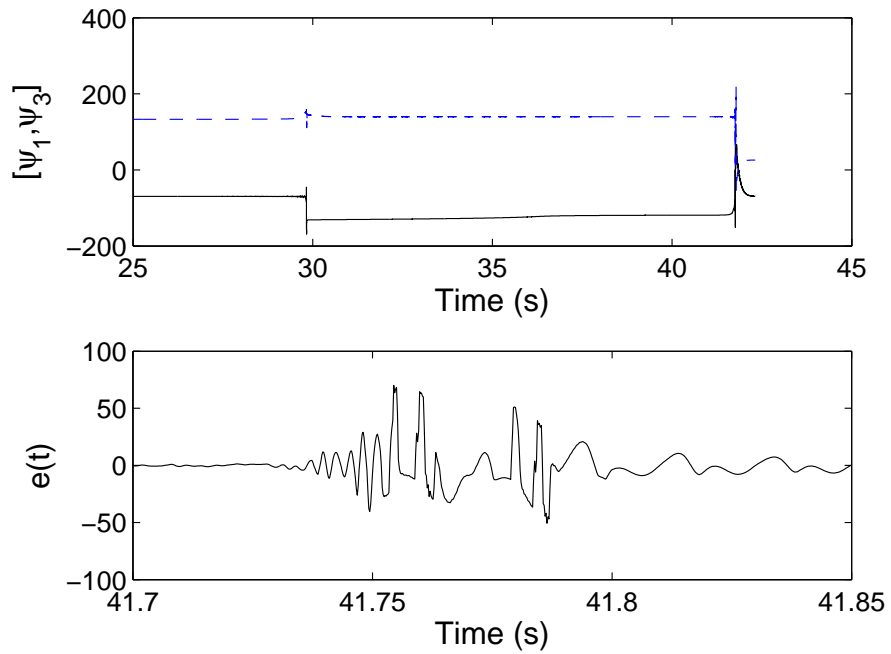


Figure 5.5: Experimental results for adaptive servocompensator implemented with four adaptation variables. $\psi(1)$ and $\psi(3)$ are shown in the top plot. Notice the peaking events in the adaptation variables near 30 and 42 s. The lower plot shows the tracking error during the second peaking event.

to be sufficiently large for the adaptation to succeed. Clearly, there is room for improvement in the design of adaptive servocompensators in systems with hysteresis.

Chapter 6

A Frequency Estimation-Based Indirect Adaptive Servocompensator

6.1 Introduction

In Chapter 5, we observed that because the harmonics created by hysteresis nonlinearities are fairly small when compared to the size of the reference trajectory, traditional nonlinear adaptive servocompensators are not ideal in systems with hysteresis. When sinusoidal or sawtooth waves (a.k.a. raster or triangular waves) are passed through a hysteresis operator, the output signal possesses a spectrum with frequency components at multiples of the reference frequency, a property which we discussed in detail in Chapter 4. If we can estimate the fundamental frequency of the reference signal, we can then use multiples of the estimated frequency to compensate for hysteresis according to the principles discussed in Chapter 3.

We therefore propose a frequency-estimation-based slow adaptation law to create an adaptive servocompensator, which we refer to in this dissertation as an *indirect adaptive servocompensator*, which is well suited to tracking problems like those found in systems with hysteresis. In this Chapter, we will refer to the fundamental frequency of a signal as simply the frequency of the signal. For example, when we refer to an unknown sawtooth signal as having one unknown frequency, we imply that the fundamental frequency of the signal is unknown. The design of this controller is based on a linear system, but we will show that the same design can be used in systems with

hysteresis as well. We will see that the stability proof of this proposed controller requires novel nonlinear analysis, based on a union of phase portrait techniques and linearization. We will also demonstrate that the proposed method can be extended to more general regulation problems, where there are more than one unknown frequencies present in the system.

Several related problems have been addressed in the literature. In particular, both Brown and Zhang [72] and Bodson and Douglas [73] utilize estimation of an unknown frequency and an internal model controller to reject an unknown disturbance. Lu and Brown extended the work of [72] to the case where the disturbance is an exponentially damped sinusoid [74]. Wang *et al.* dealt with this problem in a noisy discrete-time setting, where an additional adaptive controller was included to combat the noise and minimize the output variance [75]. However, each of these works focuses on the case where there is only one unknown frequency, and furthermore, do not analytically explore cases where *harmonic* inputs or disturbances are present.

We will investigate the performance and stability of the indirect adaptive servocompensator in a variety of situations. We will first address the case where there is one unknown frequency, and present a condition on the amplitude of the reference trajectory that will guarantee exponential stability and zero tracking error when harmonic disturbances are present. We will also prove exponential stability when there are two unknown frequencies and show local exponential stability in an n -frequency case. In our stability proof for two unknown frequencies, we will first show that the average system states enter a small region around the desired equilibrium points, and then use local stability of the equilibrium point to draw conclusions about the system behavior. We will then address the performance of the proposed controller in the presence of hysteresis. Finally, we will present our experimental results, which confirm the effectiveness of the proposed controller in nanopositioning applications. In particular, the proposed method outperformed Iterative Learning Control (ILC) [38] for sinusoidal signals at 5, 25, 50, 100 and 200 Hz, and was competitive with

ILC for a sawtooth signal of 5 Hz.

6.2 Problem Formulation and Controller Design

We will consider systems comprised of a linear plant $G_p(s)$, represented in state-space as

$$\begin{aligned}\dot{x}(t) &= Ax(t) + B(u(t) + \alpha(t)) \\ y(t) &= Cx(t)\end{aligned}\tag{6.1}$$

where $u(t)$ is the control signal, and $\alpha(t)$ is a matched disturbance. The control objective is to regulate the tracking error $e(t) = y_r(t) - y(t)$ to zero, where $y_r(t)$ denotes the reference signal to be tracked. We will deal with a variety of reference and disturbance signals in this paper, and the general form we consider is

$$y_r(t) = \sum_{k=1}^m R_{1k} \sin(\zeta_k \omega_1 t + \Phi_{1k})\tag{6.2}$$

$$\alpha(t) = \sum_{i=1}^n \sum_{k=1}^m r_{ik} \sin(\zeta_k \omega_i t + \phi_{ik})\tag{6.3}$$

where the frequencies ω_i , phases Φ_{1k} and ϕ_{ik} , and the amplitudes R_{1i} and r_{ik} are unknown. The constant vector $\zeta = [\zeta_1, \dots, \zeta_m]'$ is assumed to be known *a priori* and is used in the control design. We assume that each ζ_k is a natural number, and that $\zeta_1 = 1$. Note that this class of reference signals also covers $T = 2\pi/\omega_1$ -periodic waveforms approximated by a finite Fourier series. We will then focus on two special cases of (6.2) and (6.3). First, we consider a sinusoidal reference and a harmonic disturbance, which follows from the general setup by letting $n = 1$, $R_{1k} = 0$, $\forall k \neq 1$,

and $\Phi_{11} = 0$:

$$y_r(t) = R_{11} \sin(\omega_1 t) \quad (6.4)$$

$$\alpha(t) = \sum_{k=1}^m r_{1j} \sin(\zeta_k \omega_k t + \phi_{1k}) \quad (6.5)$$

This particular choice of reference and disturbance is motivated by applications such as nanopositioning [76], where at the steady state an input nonlinearity (e.g., hysteresis) introduces a matched disturbance with harmonics at multiples of the frequency of a sinusoidal reference [77]. The second special case of (6.2) and (6.3) we consider consists of a sinusoidal reference and sinusoidal disturbance with unknown and unrelated frequencies, i.e., $m = 1$, $n = 2$, $\Phi_{11} = 0$, and $r_{11} = 0$:

$$y_r(t) = R_{11} \sin(\omega_1 t) \quad (6.6)$$

$$\alpha(t) = r_{21} \sin(\omega_2 t + \phi_{21}) \quad (6.7)$$

This choice of reference and disturbance is indicative of a system perturbed by an external source, which is often considered in tracking problems [78]. The following assumption is typical in the servocompensator literature [53, 55, 57, 68, 69, 79].

Assumption 11 *The plant $G_p(s)$ has no zero at $j\zeta_k \omega_i$, $i = 1, \dots, n$, $k = 1, \dots, m$.*

Fig. 6.1 illustrates the design of the controller. First, based on the internal model principle [53, 55], we design a servocompensator for the aforementioned system. We define the servocompensator $C^i(s)$, with state $\eta^i = [\eta_1^i, \eta_2^i, \dots, \eta_{2m}^i]' \in \mathbb{R}^{2m}$, input $e(t)$, and output $y_c^i \in \mathbb{R}$, as

$$\dot{\eta}^i(t) = \bar{\mathbf{C}}^*(\sigma_i) \eta^i(t) + \bar{\mathbf{B}}^* e(t) \quad (6.8)$$

$$y_c^i(t) = k_\eta^i(\sigma_i) \eta^i(t) + D_c^i(\sigma_i) e(t)$$

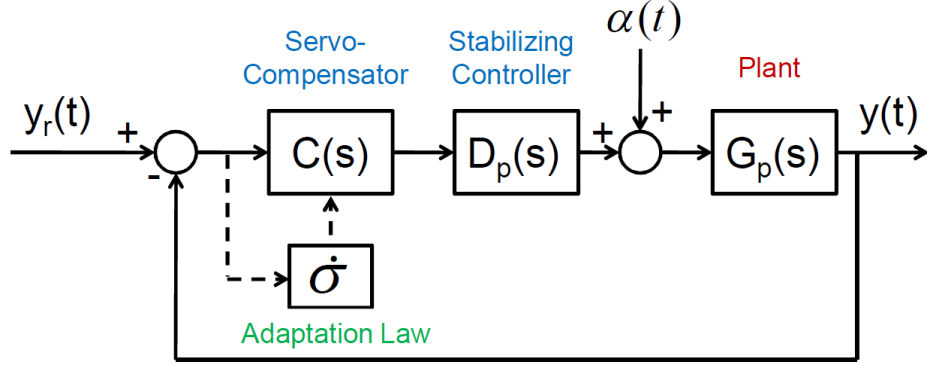


Figure 6.1: Block Diagram of the closed-loop system.

where

$$\bar{\mathbf{C}}^*(\sigma_i) = \begin{bmatrix} \zeta_1 \mathbf{C}^*(\sigma_i) & \cdots & 0 \\ \vdots & \ddots & \vdots \\ \cdots & 0 & \zeta_m \mathbf{C}^*(\sigma_i) \end{bmatrix}, \bar{\mathbf{B}}^* = \begin{bmatrix} \kappa_1 \mathbf{B}^* \\ \vdots \\ \kappa_m \mathbf{B}^* \end{bmatrix}$$

$$\mathbf{C}^*(\sigma_i) = \begin{bmatrix} 0 & \sigma_i \\ -\sigma_i & 0 \end{bmatrix}, \mathbf{B}^* = \begin{bmatrix} 0 \\ 1 \end{bmatrix}$$

σ_i is the estimate of the frequency ω_i , and $\kappa = [\kappa_1, \kappa_2, \dots, \kappa_m]' \in \mathbb{R}^m$, $\kappa_i > 0 \forall i$, $k_\eta^i(\sigma_i) \in \mathbb{R}^{1 \times 2m}$, and $D_c^i(\sigma_i) \in \mathbb{R}$ are design parameters used to stabilize the system. In particular, we will select the design parameters $k_\eta^i(\sigma_i)$, $D_c^i(\sigma_i)$, and κ such that each $C^i(s)$ behaves like a notch filter, similar to what was done in [80]. For example, if $n = m = 1$, then

$$C^1(s) = \frac{s^2 + 2\zeta_c \zeta_1 \sigma_1 s + (\zeta_1 \sigma_1)^2}{s^2 + (\zeta_1 \sigma_1)^2}$$

where $\zeta_c \ll 1$ is the notch parameter. This reduces the effect the compensator has on the overall phase margin of the system, which will allow us to stabilize the system over all possible frequency estimates. We have also left ζ_1 in the above equations despite our assumption that it is equal to 1, in order to make the effect of ζ_j more clear when $n, m \neq 1$. We then utilize n such servocompensators

connected in parallel to realize the compensator $C(s)$ shown in Fig. 6.1. The i superscript is used to denote which frequency estimate $C^i(s)$ uses. Note that if there is only one unknown frequency, $C(s) = C^1(s)$. To clarify the notation, we denote the combined state of the n parallel servocompensators $C(s)$ as $\check{\eta}$. We also denote the vectors of unknown frequencies and their estimates as $\omega = [\omega_1, \dots, \omega_n]'$ and $\sigma = [\sigma_1, \dots, \sigma_n]'$, respectively.

We will also require a stabilizing controller $D_p(s)$, given in the state-space as

$$\dot{\xi}(t) = A_d \xi(t) + B_d \left(\sum_{i=1}^n y_c^i(t) \right) \quad (6.9)$$

$$u(t) = C_d \xi(t) + D_d \left(\sum_{i=1}^n y_c^i(t) \right) \quad (6.10)$$

The output of the stabilizing controller $D_p(s)$ is $u(t)$, the control signal to the plant (6.1). We will also define the state vector $\chi = [x, \check{\eta}, \xi]$ for later use. Since the frequencies are unknown, the vector $\sigma \in \mathfrak{R}^n$ will be updated by an adaptation law, the goal of which is to drive the parameter error $\tilde{\sigma} = \sigma - \omega$ to zero. The estimation of the i th frequency σ_i will be governed by the adaptation law,

$$\dot{\sigma}_i = -\gamma_i \sigma_i(t) e(t) \eta_1^i(t) \quad (6.11)$$

where $1 \gg \gamma_i > 0$ is the adaptation gain, and η_1^i represents the first component of the state vector η^i of the servocompensator $C^i(s)$. The smallness of γ_i is required to facilitate two-time-scale averaging analysis on the system, which will be discussed in Section 6.3. Furthermore, we will select the initial condition of σ to be positive and bounded away from zero. The form of the adaptation law was originally derived from a formal gradient approach, then modified into that in (6.11) to guarantee stability. A very similar adaptation law was proposed by Brown and Zhang in [72].

6.3 Analysis of the Closed-Loop System

We shall analyze the closed-loop system using two-time-scale averaging theory [81, 82]. Two-time-scale averaging allows us to separate the analysis of the closed-loop system into the analysis of two separate subsystems, a fast or boundary-layer system, and a slow or average system. We first establish the stability of the boundary-layer system in Subsection 6.3.1. In the following subsections, we investigate the stability for the average system, and subsequently for the full closed-loop system, for different cases of the reference and disturbance input. Specifically, in Subsection 6.3.2 we prove local exponential stability for the general n -frequency case. In Subsections 6.3.3 and 6.3.4, we establish stronger, global exponential stability results for more specialized cases of one frequency (6.4)-(6.5), and two frequencies (6.6)-(6.7), respectively.

6.3.1 Stability of the Boundary-Layer System

First define the matrices

$$\begin{aligned}\check{C}^*(\sigma) &= \text{diag}(\bar{C}^*(\sigma_1), \bar{C}^*(\sigma_2), \dots, \bar{C}^*(\sigma_n)) \\ k_\eta(\sigma) &= [k_\eta^1(\sigma_1)', k_\eta^2(\sigma_2)', \dots, k_\eta^n(\sigma_n)']' \\ D_c(\sigma) &= \sum_{i=1}^n D_c^i(\sigma_i)\end{aligned}$$

and \check{B}^* as an n -high stack of vectors \bar{B}^* . We now define the boundary-layer system for the general closed-loop system (6.1)-(6.3), (6.8)-(6.11), by setting $\gamma_i = 0, \forall i = 1, 2, \dots, n$ in (6.11). This freezes the value of σ at σ_{bl} . Denoting the state variables of the boundary-layer system as

$\chi_{bl} = [x'_{bl}, \check{\eta}'_{bl}, \check{\xi}'_{bl}]'$, we write the closed-loop boundary-layer system as

$$\begin{aligned} \dot{\chi}_{bl}(t) &= f_{bl}(\chi_{bl}, \sigma_{bl}, t) \\ &= \begin{bmatrix} (A - BD_d D_c(\sigma_{bl})C) & BD_d k_\eta(\sigma_{bl}) & BC_d \\ -\check{B}^* C & \check{C}^*(\sigma_{bl}) & 0 \\ -B_d D_c(\sigma_{bl})C & B_d k_\eta(\sigma_{bl}) & A_d \end{bmatrix} \chi_{bl} \\ &\quad + \begin{bmatrix} BD_d D_c(\sigma_{bl})y_r(t) + B\alpha(t) \\ \check{B}^* y_r(t) \\ B_d D_c(\sigma_{bl})y_r(t) \end{bmatrix} \end{aligned} \quad (6.12)$$

Using frequency-domain techniques, we can use the stabilizing controller (6.9)-(6.10) to establish input-to-state stability (ISS) of the boundary-layer system. Recall that we have selected the output matrices of $C(s)$ to guarantee that it behaves like a notch filter. Therefore, we can design $D_p(s)$ to stabilize the transfer function

$$H_p(s) = \frac{D_p(s)G_p(s)}{1 + D_p(s)G_p(s)} \quad (6.13)$$

Using this controller structure, it can be shown that the system will be ISS-stable for a small enough ζ_c , provided the gain crossover frequency ω_{gc} of $H_p(s)$ is sufficiently far away from σ_{bl} . Note that since the boundary-layer system is linear, ISS implies that the closed-loop system states will converge to the steady-state trajectories exponentially fast for any periodic reference $y_r(t)$ and disturbance $\alpha(t)$. In addition, note that if $\sigma_{bl} = \omega$, the tracking error $e(t)$ will converge to zero.

6.3.2 Averaging Analysis for the Case of n Unknown Frequencies: Local Exponential Stability

We now shift our attention to the slow or average system. This analysis is based on the two-time-scale averaging framework presented in [82], and we will utilize this framework to analyze the closed-loop system for different reference trajectories in Subsections 6.3.2-6.3.4. We begin by considering the case where there are n unknown frequencies, shown in (6.2) and (6.3). We first define θ_i as the average of σ_i , as well as the vector $\theta = [\theta_1, \dots, \theta_n]$. The dynamics of θ_i obey

$$\begin{aligned}\dot{\theta}_i &= F_{av}(\chi_{bl}(\theta, t), \theta_i, t) \\ &= - \lim_{\tau \rightarrow \infty} \frac{\gamma}{\tau} \int_0^\tau \theta_i e(t) \eta_1^i(t) dt\end{aligned}\quad (6.14)$$

where $e(t)$ and $\eta_1^i(t)$ represent the steady-state trajectories of e and η resulting from the boundary-layer system (6.12) with $\sigma_{bl} = \theta$. We will make the following assumption to simplify the form of the equation for the average dynamics $\dot{\theta}$.

Assumption 12 *The combinations $\zeta_f \omega_i$ are unique, i.e., $\zeta_f \omega_i \neq \zeta_g \omega_k$ for all $i, k = 1, \dots, n$; $f, g = 1, \dots, m$, unless $f = g$ and $i = k$.*

This assumption implies that no two unknown frequencies share a harmonic of order below $\max(\zeta)$, and is primarily made to keep the following equations manageable. Define $G_p(s) \triangleq G_n(s)/G_d(s)$, and let

$$\begin{aligned}\bar{C}_i(s) &= \prod_{k=1, k \neq i}^n \prod_{l=1}^m (s^2 + (\zeta_l \theta_k)^2) \\ &\quad \cdot \prod_{l=2}^m (s^2 + (\zeta_l \theta_i)^2)\end{aligned}\quad (6.15)$$

We also define

$$F_i(\zeta_l, \omega_k) = \gamma_i \theta_i^2 \kappa_1 |\bar{C}_i(j\zeta_l \omega_k)|^2 / 2 \quad (6.16)$$

$$\begin{aligned} D(j\zeta_l \omega_k) &= G_d(j\zeta_l \omega_k) C_d(j\zeta_l \omega_k) \\ &\quad + G_n(j\zeta_l \omega_k) C_n(j\zeta_l \omega_k) D_p(j\zeta_l \omega_k) \end{aligned} \quad (6.17)$$

where $C(s) = C_n(s)/C_d(s)$. We also will require following definition,

$$\begin{aligned} H_l(j\omega_k) &= \left[R_{1l}^2 |G_d(j\omega_k)|^2 + r_{1l}^2 |G_n(j\omega_k)|^2 \right. \\ &\quad \left. - 2R_{1l}r_{1l} |G_d(j\omega_k)| |G_n(j\omega_k)| \right. \\ &\quad \left. \cdot \cos(\angle G_p(j\omega_k) + \Phi_{1l} + \phi_{1l}) \right] \end{aligned} \quad (6.18)$$

Note that $H_l \geq (R_{1l} - |G_p|r_{1l})^2 \geq 0$. Using Assumption 12 and the above definitions, we can calculate the form of $\dot{\theta}_i$ (derivation details omitted in the interest of brevity):

$$\begin{aligned} \dot{\theta}_i &= \sum_{l=1}^m \frac{-F_i(\zeta_l, \omega_1) H_l(j\omega_1) (\theta_i^2 - \zeta_l^2 \omega_1^2)}{|D(j\zeta_l \omega_1)|^2} \\ &\quad + \sum_{k=2}^n \sum_{l=1}^m \frac{-F_i(\zeta_l, \omega_k) |G_n(j\zeta_l \omega_k)|^2 r_{kl}^2 (\theta_i^2 - \zeta_l^2 \omega_k^2)}{|D(j\zeta_l \omega_k)|^2} \end{aligned} \quad (6.19)$$

Note that, for every $i, k = 1, \dots, n$ and $l = 1, \dots, m$ there exists a combination θ_i and $\zeta_l \omega_k$ such that $\bar{C}_i(j\zeta_l \omega_k)$ is zero if $\theta_i = \omega_k$, except for the case where $i = k$ and $l = 1$. This fact can be seen by looking at the final product grouping in (6.15), $\prod_{l=2}^m [(s^2 + (\zeta_l \theta_i)^2)]$. In addition, notice that $|\bar{C}_i(j\zeta_l \omega_k)|$ always appears squared. Therefore, using the product rule of differentiation, we can see that any partial derivative of the right-hand side of (6.19) with respect to θ_l , $\forall l = 1, \dots, n$ and evaluated at the equilibrium point $\theta = \omega$ will be zero, except the partial derivative with respect

to θ_i . In addition, this guarantees that when this partial derivative is evaluated at $\theta = \omega$, only the portion of the derivative taken with respect to the term $(\theta_i^2 - \zeta_l^2 \omega_k^2)$ will be non-zero. This can be calculated as

$$\begin{aligned} \left. \frac{\partial \dot{\theta}_i}{\partial \theta_i} \right|_{\theta=\omega} &= \sum_{l=1}^m \frac{-F_i(\zeta_l, \omega_1) H_i(j\omega_1)(2\omega_i)}{|D(j\zeta_l \omega_1)|^2} \\ &\quad + \sum_{k=2}^n \sum_{l=1}^m \frac{-F_i(\zeta_l, \omega_k) |G_n(j\zeta_l \omega_k)|^2 r_{kl}^2 (2\omega_i)}{|D(j\zeta_l \omega_k)|^2} \end{aligned} \quad (6.20)$$

which is always negative over the adaptation variable range. Therefore, the resulting Jacobian of the average system is comprised of negative terms in the diagonal, and zeros everywhere else; thus the average system is exponentially stable for sufficiently small initial conditions $(\theta(0) - \omega)$. We also note that if $\theta = \omega$, the closed-loop system (6.1)-(6.3), (6.8)-(6.11) transformed into error coordinates possesses an equilibrium where $e(t) = 0$. Let $\bar{\chi}$ denote the steady-state solution of the aforementioned closed-loop system when $\sigma(t) \equiv \omega$. Then by Theorem 4.4.3 of [82], the origin of the closed-loop system with coordinates $(\chi(t) - \bar{\chi}(t), \sigma(t) - \omega)$ is locally exponentially stable.

6.3.3 Averaging Analysis for the Case of One Unknown Frequency: Exponential Stability

In this subsection, we will focus on the case where there is one unknown frequency, and present a sufficient condition for the exponential stability of the closed-loop system. We will assume that y_r and α obey (6.4)- (6.5).

Assumption 13 *The plant $G_p(s)$ has no poles at $s = j\omega_1$.*

Theorem 2 *Consider the closed-loop system (6.1), (6.4)-(6.5), and (6.8)- (6.11). Let Assumptions 11 and 13 hold. Let $\bar{\chi}$ denote the steady-state solution of the aforementioned closed-loop system*

when $\sigma(t) \equiv \omega_1$. Then, for all bounded initial conditions $(\chi(0), \sigma(0))$ where $\sigma(0) > 0$, there exist constants $R_r > 0$ (dependent on $\{r_{1l}\}_{l=1}^m$) and $\varepsilon_\gamma > 0$, such that, if $R_{11} > R_r$ and $\gamma < \varepsilon_\gamma$, all states of the closed-loop system are bounded. In addition, the origin of the closed-loop system expressed in the error coordinates $(\chi(t) - \bar{\chi}(t), \sigma(t) - \omega_1)$ is exponentially stable, and the tracking error $e(t)$ converges to zero exponentially fast.

Proof. To prove Theorem 2, we will require exponential stability of both the boundary layer system, established through the controller design in the previous subsection, and exponential stability of the average system. Note that we will be removing the i super and subscripts from signals in this subsection, since there is only one frequency to estimate. Now let

$$\bar{C}(s) = \prod_{k=2}^m (s^2 + (\zeta_k \theta)^2) \quad (6.21)$$

$$(6.22)$$

We will focus on the derivation of $\hat{\theta}$ the case of one unknown frequency outlined in Subsection 6.3.3; the 2 and n frequency derivations follow the same lines with additional details. The controller transfer function is defined by

$$C(s) = \frac{C_n(s)}{C_d(s)} = \prod_{j=1}^m \frac{s^2 + 2\zeta_c \zeta_j \theta s + (\zeta_j \theta)^2}{(s^2 + (\zeta_j \theta)^2)} \quad (6.23)$$

The sensitivity function $S(s)$ is then

$$S(s) = \frac{G_d(s)C_d(s)}{G_d(s)C_d(s) + C_n(s)G_n(s)D_p(s)} \quad (6.24)$$

We also compute $C_{\eta_1}(s)$, defined as the transfer function between $e(t)$ and $\eta_1(t)$ as

$$C_{\eta_1}(s) = \frac{\kappa_1 \theta}{s^2 + \theta^2} \quad (6.25)$$

Using the stability properties of the boundary-layer system, we can see that

$$e(t) = S(s)[y_r(t)] - S(s)G_p(s)[\alpha(t)] \quad (6.26)$$

and, using the structure of $\mathbf{C}^*(\theta)$, that

$$\eta_1(t) = C_{\eta_1}(s)S(s)[y_r(t)] - C_{\eta_1}(s)G_p(s)S(s)[\alpha(t)] \quad (6.27)$$

where the notation $F(s)[g(t)]$ denotes the filtering of $g(t)$ by the transfer function $F(s)$. Plugging (6.26) and (6.27) into (6.14), we can expand the integrand in (6.14) into four terms, resulting in

$$\begin{aligned} \dot{\theta} = & - \lim_{\tau \rightarrow \infty} \frac{\gamma}{\tau} \int_0^\tau \theta \left(S(s)[y_r(t)]C_{\eta_1}(s)S(s)[y_r(t)] \right. \\ & - S(s)[y_r(t)]C_{\eta_1}(s)G_p(s)S(s)[\alpha(t)] \\ & - S(s)G_p(s)[\alpha(t)]C_{\eta_1}(s)S(s)[y_r(t)] \\ & \left. + S(s)G_p(s)[\alpha(t)]C_{\eta_1}(s)G_p(s)S(s)[\alpha(t)] \right) dt \quad (6.28) \end{aligned}$$

Note that each signal comprising (6.28) is periodic with period $T = 2\pi\omega_1$; therefore we can drop the limit and set $\tau = T$. In this calculation, we will encounter a series of integrals of the form

$$\int_0^T |A(j\zeta_A\omega_1)| \sin(\zeta_A\omega_1 t + \phi_A) \cdot |B(j\zeta_B\omega_1)| \sin(\zeta_B\omega_1 t + \phi_B) dt \quad (6.29)$$

where $A(s) = |A(s)|\angle\phi_A$ and $B(s) = |B(s)|\angle\phi_B$ are transfer functions which are formed by terms in the integrand of (6.28). We will see how to compute the final form of $\dot{\theta}$ by focusing on the term $S(s)[y_r(t)]C_{\eta_1}(s)S(s)[y_r(t)]$. For this term, $A(s) = S(s)$, $B(s) = C_{\eta_1}(s)S(s)$, and $\zeta_A = \zeta_B = 1$. Evaluating (6.29) with these values results in

$$\frac{|A(j\omega_1)||B(j\omega_1)| \cos(\phi_A - \phi_B)}{2}$$

However, since $S(s)$ is included in both $A(s)$ and $B(s)$, only the phase of $C_{\eta_1}(s)$ appears; thus it can be shown that,

$$\cos(\phi_A - \phi_B) = \text{sgn}(\tilde{\theta})$$

We can arrive at similar expressions to those above for the remaining integrand terms in (6.28).

Using (6.21) and (6.16) together with our above discussion, we can now compute $\dot{\theta}$ by evaluating

each integral formed in (6.28), and arrive at the expression

$$\begin{aligned}\dot{\theta} = & \frac{-F(1, \omega_1)R_{11}^2|G_d(j\omega_1)|^2(\theta^2 - \omega_1^2)}{|D(j\omega_1)|^2} \\ & + 2F(1, \omega_1)R_{11}r_{11}|G_d(j\omega_1)||G_n(j\omega_1)| \\ & \cdot \frac{(\theta^2 - \omega_1^2)\cos(\angle G(j\omega_1) + \phi_{11})}{|D(j\omega_1)|^2} \\ & + \sum_{l=1}^m \frac{-F(\zeta_l, \omega_1)r_{1l}^2|G_n(j\zeta_l\omega_1)|^2(\theta^2 - (\zeta_l\omega_1)^2)}{|D(j\zeta_l\omega_1)|^2}\end{aligned}$$

The terms $(\theta^2 - \omega_1^2)$ and $(\theta^2 - (\zeta_l\omega_1)^2)$ have appeared due to the effect of the $\cos(\phi_A - \phi_B)$ terms combined with $C_d(s)$. The denominator of (6.25) also cancels one element of $C_d(s)$. The remaining terms of $C_d(s)$ are contained in $\bar{C}(s)$. We can group together the terms with the common factor $(\theta^2 - \omega_1^2)$ to arrive at

$$\begin{aligned}\dot{\theta} = & \frac{-F(1, \omega_1)H(j\omega_1)}{|D(j\omega_1)|^2}(\theta^2 - \omega_1^2) \\ & + \sum_{l=2}^m \frac{-F(\zeta_l, \omega_1)r_{1l}^2|G_n(j\zeta_l\omega_1)|^2(\theta^2 - (\zeta_l\omega_1)^2)}{|D(j\zeta_l\omega_1)|^2}\end{aligned}\tag{6.30}$$

where F and H are defined by suppressing the subscripts in (6.16) and (6.18) respectively. Note that $H(j\omega_1)$ is guaranteed to be non-negative, and is positive (due to Assumptions 11 and 13) if $R_{11} > r_{11}|G_p(j\omega_1)|$, which we will assume for the remainder of our analysis. In addition, notice that $\dot{\theta}$ is positive for $\omega_1 > \theta > 0$, and negative for $\theta > \zeta_m\omega_1$; therefore the initial condition of θ defines an invariant set Σ in which θ resides for all time. We now use Lyapunov analysis to show exponential stability of the average system. We start with the Lyapunov function candidate

$V = \tilde{\theta}^2/2$, where $\tilde{\theta} = \theta - \omega_1$. Using (6.30) and the definition of $H(j\omega_1)$, we can evaluate \dot{V} as

$$\begin{aligned} \dot{V} = & \frac{-F(1, \omega_1)H(j\omega_1)(\theta + \omega_1)}{|D(j\omega_1)|^2} \tilde{\theta}^2 \\ & + \sum_{l=2}^m \frac{-F(\zeta_l, \omega_1)r_{1l}^2|G_n(j\zeta_l\omega_1)|^2(\theta^2 - (\zeta_l\omega_1)^2)}{|D(j\zeta_l\omega_1)|^2} \tilde{\theta} \end{aligned} \quad (6.31)$$

It can be easily seen from (6.31) that if $r_{1l} = 0, \forall l > 1$, there will exist a constant $k > 0$ such that $\dot{V} \leq -kV$. This proves exponential stability of the system if $\alpha(t) = 0$.

We now focus on the case where $r_{1l} \neq 0$. It is important to note that $|\bar{C}(j\zeta_l\omega_1)|$, and thus $F(\zeta_l, \omega_1)$, possesses a term of the form $|\zeta_l\theta - \zeta_l\omega_1| = \zeta_l|\tilde{\theta}|$. Also note that $(\theta^2 - (\zeta_l\omega_1)^2)$ and $\tilde{\theta}$ possess the same sign when $\theta < \omega_1$ or $\theta > \zeta_m\omega_1$. This implies that there exists a constant $c_1 > 0$ such that $\dot{V} \leq -c_1V$ when $\tilde{\theta} \notin [0, \zeta_m\omega_1 - \omega_1]$. We can therefore focus our attention on the set $\tilde{\theta} \in [0, \zeta_m\omega_1 - \omega_1]$. We notice that within this set, $|\tilde{\theta}| = \tilde{\theta}$. Therefore, when $l \neq 1$, we can find a constant $c_f > 0$ to bound $F(\zeta_l, \omega_1)$ in the set $\tilde{\theta} \in [0, \zeta_m\omega_1 - \omega_1]$ as

$$F(\zeta_l, \omega_1) \leq c_f \tilde{\theta}$$

Finally, from (6.30) and the condition $R_{11} > r_{11}|G(j\omega_1)|$, H is strictly increasing with the reference amplitude R_{11} , while $F(\cdot)$ is independent of R_{11} . This allows us to write, for positive constants k_1 and k_2 ,

$$\dot{V} \leq -R_{11}^2 k_1 \tilde{\theta}^2 + c_f k_2 \tilde{\theta}^2 \quad (6.32)$$

where the existence of k_1 and k_2 are guaranteed by the boundedness of θ within the set of interest. Therefore, for a sufficiently large R_{11} , there exists a constant $c_2 > 0$ such that when $\tilde{\theta} \in [0, \zeta_m\omega_1 - \omega_1]$,

$$\dot{V} \leq -c_2V \quad (6.33)$$

Since both c_1 and c_2 are greater than zero, we can use the minimum of these two constants to bound \dot{V} for all $\tilde{\theta}$, and conclude the exponential stability of the average system. Since we have now shown exponential stability of both the average and boundary layer trajectories, we can apply Theorem 4.4.3 of [82], and conclude exponential stability of the trajectory $(\bar{\chi}, \omega_1)$ for a sufficiently small adaptation gain γ , which also implies the boundedness of the state trajectory and the convergence of the tracking error to zero. \square

Remark 6 *Assumption 13 is not typically found in the adaptive control literature; however, it is required in our proof since Theorem 2 shows both the tracking error e and adaptation error $\tilde{\theta}$ converge to zero. If this assumption is not satisfied, stability can still be shown for sufficiently large r_{11} by using r_{11} in the same manner R_{11} was used in the above proof. This is because if $G_d(j\omega_1) = 0$, from (6.18), $H(j\omega_1)$ becomes $r_{11}^2 |G_n(j\omega_1)|^2$.*

Remark 7 *The required size of $R_{11} > R_r$ is determined by the sizes of the constants k_1 and k_2 in (6.32). These constants vary with the frequency ω_1 , plant transfer function $G_p(s)$, stabilizing controller $D_p(s)$, and the size of the disturbance.*

6.3.4 Averaging Analysis for the Case of Two Unknown Frequencies: Exponential Stability

We now present results on the stability of the closed-loop system in the case of two unknown frequencies, (6.6) -(6.7). Without loss of generality, we will assume for our analysis that $\omega_1 < \omega_2$. We will also set $\gamma_1 = \gamma_2 = \gamma$, which will create a very useful symmetry in the dynamics of the average system. As there are now multiple frequency estimates, we will reintroduce the i subscript in order to differentiate between the first and second frequency estimates and frequencies. Using the symmetry of the system, we can compute the dynamics of the average system (using the same

procedure as that outlined in Subsection 6.3.3) as

$$\begin{aligned}\dot{\theta}_1 &= f(\theta_1, \theta_2) \\ \dot{\theta}_2 &= f(\theta_2, \theta_1)\end{aligned}\tag{6.34}$$

where

$$\begin{aligned}f(a, b) &= \frac{-\mathbb{F}(a, b, \omega_1)R_{11}^2|G_d(j\omega_1)|^2(a^2 - \omega_1^2)}{|\mathbb{D}(a, b, \omega_1)|^2} \\ &+ \frac{-\mathbb{F}(a, b, \omega_2)r_{21}^2|G_n(j\omega_2)|^2(a^2 - \omega_2^2)}{|\mathbb{D}(a, b, \omega_2)|^2}\end{aligned}\tag{6.35}$$

$$\mathbb{F}(a, b, \omega_i) = \gamma a^2 \kappa_1 (b^2 - \omega_i^2)^2 / 2\tag{6.36}$$

$$\begin{aligned}\mathbb{D}(a, b, \omega_i) &= G_d(j\omega_i)(a^2 - \omega_i^2)(b^2 - \omega_i^2) \\ &+ [G_n(j\omega_i)D_p(j\omega_i)(a^2 - \omega_i^2 + 2\zeta\omega_i a j) \\ &\cdot (b^2 - \omega_i^2 + 2\zeta\omega_i b j)]\end{aligned}\tag{6.37}$$

where due to the symmetry of the system, we note that $\mathbb{D}(a, b, \omega_i) = \mathbb{D}(b, a, \omega_i)$. We will analyze the system (6.34) using a phase portrait approach. Based on the terms $(a^2 - \omega_1^2)$ and $(a^2 - \omega_2^2)$ in (6.35), we know that the system possesses equilibrium points at $\theta = (\omega_1, \omega_2)$ and $\theta = (\omega_2, \omega_1)$. Because of the symmetric structure of the controller, either of these equilibrium points is desirable from a tracking perspective, as the boundary layer system at either point possess zero tracking error. A second consequence of the terms $(a^2 - \omega_1^2)$ and $(a^2 - \omega_2^2)$ is that, from any positive initial condition θ_0 , the state θ enters the invariant set $(\theta_1, \theta_2) \in [\omega_1, \omega_2] \times [\omega_1, \omega_2] \triangleq \Omega$. This follows from the inequalities $\mathbb{F}(a, b, \omega_i) > 0, \forall a < \omega_1, i = 1, 2$ and $\mathbb{F}(a, b, \omega_i) < 0, \forall a > \omega_2, i = 1, 2$.

Within Ω , we have the following result.

Lemma 2 *Let Assumptions 11 and 13 hold. For any $\theta \in \Omega$, the inner product*

$$\left\langle \begin{bmatrix} \dot{\theta}_1 \\ \dot{\theta}_2 \end{bmatrix}, \begin{bmatrix} -1 \\ 1 \end{bmatrix} \right\rangle$$

is positive if $\theta_2 > \theta_1$, negative if $\theta_2 < \theta_1$, and zero if $\theta_2 = \theta_1$, except for the cases $\theta = (\omega_1, \omega_2)$ or $\theta = (\omega_2, \omega_1)$, where the inner product is zero.

Proof. The inner product can be directly calculated as

$$\begin{aligned} & \left\langle \begin{bmatrix} \dot{\theta}_1 \\ \dot{\theta}_2 \end{bmatrix}, \begin{bmatrix} -1 \\ 1 \end{bmatrix} \right\rangle \\ &= f(\theta_1, \theta_2) - f(\theta_2, \theta_1) \\ &= \frac{\gamma \kappa_1 R_{11}^2 |G_d(j\omega_1)|^2 (\theta_1^2 - \omega_1^2)(\theta_2^2 - \omega_1^2)}{2|\mathbb{D}(\theta_1, \theta_2, \omega_1)|^2} \\ & \quad \cdot [\theta_1^2(\theta_2^2 - \omega_1^2) - \theta_2^2(\theta_1^2 - \omega_1^2)] \\ & \quad + \frac{\gamma \kappa_1 r_{11}^2 |G_n(j\omega_2)|^2 (\theta_1^2 - \omega_2^2)(\theta_2^2 - \omega_2^2)}{2|\mathbb{D}(\theta_1, \theta_2, \omega_2)|^2} \\ & \quad \cdot [\theta_1^2(\theta_2^2 - \omega_2^2) - \theta_2^2(\theta_1^2 - \omega_2^2)] \end{aligned} \tag{6.38}$$

The bracketed terms can be simplified to $[\omega_1(\theta_2^2 - \theta_1^2)]$ and $[\omega_2(\theta_2^2 - \theta_1^2)]$ respectively, which together with Assumptions 11 and 13 completes the proof. \square

There are several consequences of this lemma. The first consequence is that there are no equilibrium points within the interior of Ω , except for on the line $\theta_1 = \theta_2$. However, any equilibrium points on the line must be unstable, since the vector field always points away from the $\theta_1 = \theta_2$ line inside Ω . Second, there are no possible limit cycles within Ω , as the existence of a limit

cycle would require the above inner product to be zero on locations other than the $\theta_1 = \theta_2$ line. These facts, together with the forward invariance of Ω , imply that from any initial condition θ_0 , the trajectory $\theta(t)$ converges to either (ω_1, ω_2) or (ω_2, ω_1) . Furthermore, it can be shown that the points (ω_1, ω_2) or (ω_2, ω_1) are locally exponentially stable. We start from the Lyapunov function candidate

$$V(\theta) = \frac{(\theta_1 - \omega_1)^2}{2} + \frac{(\theta_2 - \omega_2)^2}{2} \triangleq \frac{\tilde{\theta}_1^2}{2} + \frac{\tilde{\theta}_2^2}{2}$$

Consider the set

$$\Delta \triangleq \{\theta : |\tilde{\theta}_1| < \varepsilon_c, |\tilde{\theta}_2| < \varepsilon_c\} \quad (6.39)$$

We will now show exponential stability of the point (ω_1, ω_2) within Δ . Exponential stability of the point (ω_2, ω_1) can be shown by redefining $\tilde{\theta}_1 = \theta_1 - \omega_2$ and $\tilde{\theta}_2 = \theta_2 - \omega_1$, and altering the following equations accordingly. We seek to find an ε_c such that \dot{V} is negative definite within Δ . Assuming that the system is currently within the set Δ , we substitute $\theta_1 = \omega_1 + \tilde{\theta}_1$ and $\theta_2 = \omega_2 + \tilde{\theta}_2$ where $\tilde{\theta}_1, \tilde{\theta}_2 \in [-\varepsilon_c, \varepsilon_c]$. Using these substitutions together with (6.34), we can then bound \dot{V} by

$$\begin{aligned} \dot{V} \leq & \frac{-\tilde{\theta}_1^2 R_{11}^2 \kappa_1}{|\mathbb{D}(\theta_1, \theta_2, \omega_1)|^2} [\gamma_1 \theta_1^2 |G_d(j\omega_1)|^2 - \gamma_2 \theta_2^2 |2\omega_1 + \varepsilon_c| \varepsilon_c] \\ & + \frac{-\tilde{\theta}_2^2 r_{21}^2 \kappa_1}{|\mathbb{D}(\theta_1, \theta_2, \omega_2)|^2} [\gamma_2 \theta_2^2 |G_n(j\omega_2)|^2 - \gamma_1 \theta_1^2 |2\omega_2 + \varepsilon_c| \varepsilon_c] \end{aligned} \quad (6.40)$$

Using Assumptions 11 and 13, we can see that for a sufficiently small ε_c , there exists a $c_0 > 0$ such that $\dot{V} \leq -c_0 V$. Combining the asymptotic stability and local exponential stability, we imply from Theorem 4.4.3 of [82] that the origin of the closed-loop system with coordinates $(\chi(t) - \bar{\chi}(t), \sigma(t) - \omega)$, where $\omega = (\omega_1, \omega_2)$ or $\omega = (\omega_2, \omega_1)$, is exponentially stable. We have thus proved the following theorem.

Theorem 3 *Consider the closed-loop system (6.1), (6.6)- (6.11). Let Assumptions 11 and 13 hold.*

Let $\bar{\chi}$ denote the steady state solution of the aforementioned closed-loop system when $\sigma(t) \equiv \omega$, where $\omega = (\omega_1, \omega_2)$ or $\omega = (\omega_2, \omega_1)$. Then, there exists a sufficiently small γ , such that, for all bounded initial conditions $(\chi(0), \sigma(0))$ where $\sigma(0) > 0$ and $\sigma_1(0) \neq \sigma_2(0)$, all states of the closed-loop system are bounded. In addition, the origin of the closed-loop system with coordinates $(\chi(t) - \bar{\chi}(t), \sigma(t) - \omega)$ is exponentially stable. Furthermore, the tracking error $e(t)$ converges to zero.

Remark 8 *If the initial conditions and controller parameters of each $C_i(s)$ and $\dot{\sigma}_i$ are chosen to be equal, the system will behave as if it is a single controller with a single adaptation law, as there will then be identical compensators connected in parallel with identical states. We refer to this as a degenerative state for the controller. This can be prevented by choosing $\sigma_1(0) \neq \sigma_2(0)$.*

Remark 9 *For systems with non-equal adaptation gains, it can be quickly shown that all possible equilibria in Ω , other than (ω_1, ω_2) and (ω_2, ω_1) , must reside on the $\theta_1 = \theta_2$ line, and the set of these equilibria is the same as that for the case of identical adaptation gains. In addition, it can be shown that the stability properties of those equilibria are the same given different choices of adaptation gains. In other words, no stable equilibria exist in Ω except the desired points (ω_1, ω_2) and (ω_2, ω_1) . However, the existence of limit cycles in this system cannot be excluded as readily as in the identical gain case, and this will be addressed in our future work.*

Fig. 6.2 shows an example phase portrait of the average system (6.34). In addition to the phase portrait, we have plotted the level curves of the $\dot{\theta}_1$ and $\dot{\theta}_2$ equations. For this particular set of system parameters, there are three unstable equilibria on the $\theta_1 = \theta_2$ axis (two saddle points and one unstable node). For this special case of equal adaptation gains, the regions of attraction for the stable points can be explicitly calculated and are divided by the $\theta_1 = \theta_2$ line. For cases where the adaptation gains are not equal, the form of the regions of attraction are more complicated.

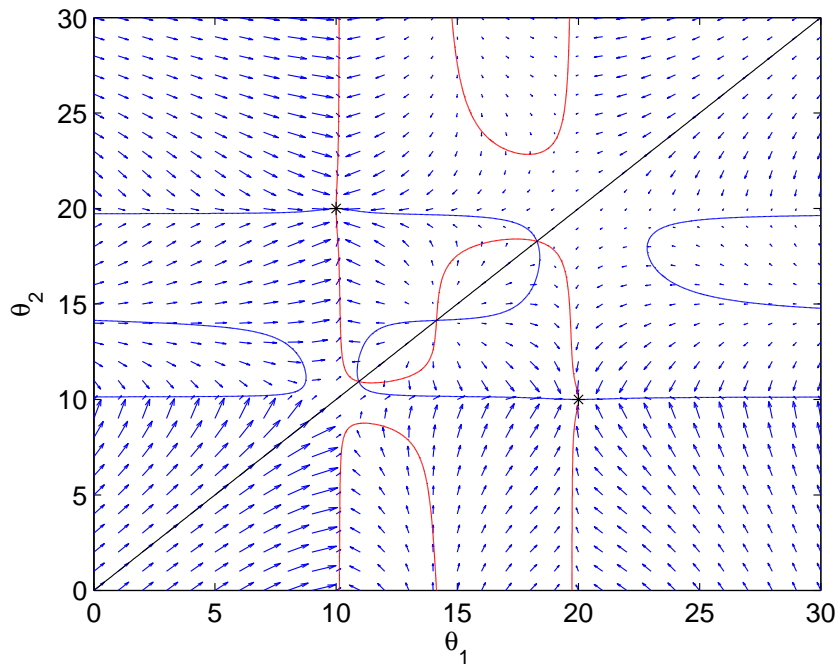


Figure 6.2: Phase portrait of average system for a sample plant and controller. The zero level curves of $\dot{\theta}_1$ (primarily vertical) and $\dot{\theta}_2$ (primarily horizontal) together with the neutral axis $\theta_1 = \theta_2$ are also plotted.

6.4 Analysis of the Closed-Loop System in the Presence of Hysteresis

With the results of Section 5.3 in hand, we are now prepared to discuss the stability of the proposed IASC in systems with hysteresis. Let the linear plant (5.1) be preceded by a Prandtl-Ishlinskii (PI) operator Γ_h , as illustrated in Fig. 6.3. Since we have used θ for the definition of the average of the

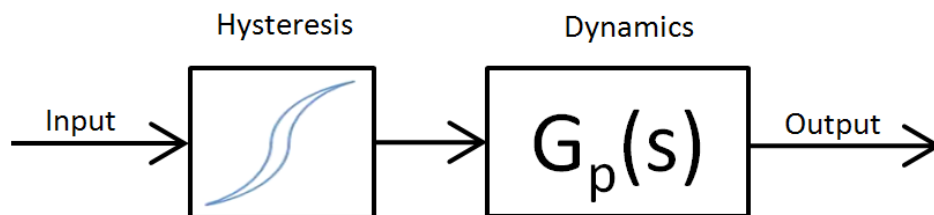


Figure 6.3: Illustration of linear plant preceded by hysteresis operator, commonly used to model piezoelectric-actuated nanopositioners.

adaptation, we will let ϑ_h represent the weights of the hysteresis operator in this section, i.e.

$$\Gamma_h[v; W(0)](t) = \vartheta_h' W(t)$$

We will also include an approximate hysteresis inversion $\hat{\Gamma}_h^{-1}$ in our control structure, based on an estimate $\hat{\vartheta}$ of the weights ϑ . We can then write the inversion error as

$$u_d(t) - u(t) = \tilde{\vartheta}' W(t) \quad (6.41)$$

where $\tilde{\vartheta} = \hat{\vartheta} - \vartheta$. For a sinusoidal reference, we can then describe the resulting closed-loop system via equations (6.1), (6.4), (6.8)- (6.11), and (6.41), where we set $u_d(t)$ equal to $u(t)$ in (6.10). Such a system can, under suitable conditions, be shown to possess a unique, asymptotically stable T -periodic solution as we proved in Chapter 3.

Once we have established that the solutions of closed-loop system are periodic at the steady state, we can use the properties of the servocompensator to analyze its disturbance attenuation properties. Since all signals in the closed-loop system are T -periodic, we can rewrite $\tilde{\vartheta}' W(t)$ using Fourier series expansion as two signals; α , which has the form of the disturbance (6.5), and α_d , which has the form

$$\alpha_d(t) = \sum_{l, l \notin \zeta} r_{1l} \sin(l\omega_1 t + \phi_l)$$

Here $\zeta \in \mathbb{R}^m$ will be considered as a design parameter to determine how many harmonics of the reference are compensated by the servocompensator. Therefore, we can treat the closed-loop system with hysteresis as the closed-loop system considered in Subsection 6.3.3 perturbed by the additional matched disturbance α_d . Note that because of the presence of the adaptation in the servocompensator, further analysis is required to a bound on the tracking error.

Define $X = [(\chi - \bar{\chi})', \sigma - \omega]'$ as the state vector of the nominal closed-loop system (6.1), (6.4), (6.8)-(6.11), transformed into error coordinates. We have already shown that this system is exponentially stable; therefore, from the converse Lyapunov theorem [64], we have that

$$\begin{aligned} c_1 \|X\|^2 &\leq V(X) \leq c_2 \|X\|^2 \\ \dot{V} &\leq -c_3 \|X\|^2, \quad \left\| \frac{\partial V}{\partial X} \right\| \leq c_4 \|X\| \end{aligned}$$

for a positive definite function V and positive constants c_1, \dots, c_4 . Now consider the closed-loop system with the disturbance α_d . Taking a time derivative of $V(X)$ and using the form of $\dot{\theta}$, we arrive at

$$\begin{aligned} \dot{V} &\leq -c_3 \|X\|^2 \\ &\quad + c_4 \|X\| \sum_{k, k \notin \zeta}^{\infty} |C_{\eta_1}(s)S(s)G_p(s)| |S(s)G_p(s)| r_{1k}^2 \Big|_{s=jk\omega_1} \end{aligned} \quad (6.42)$$

The RHS of (6.42) is negative definite for

$$\|X\| > \frac{c_4 \sum_{k, k \notin \zeta}^{\infty} |C_{\eta_1}(s)S(s)G_p(s)| |S(s)G_p(s)| r_{1k}^2}{c_3} \Big|_{s=jk\omega_1}$$

Since $r_{1k}, \forall k \notin \zeta$ is proportional to $\|\tilde{\vartheta}'\|$, for a sufficiently small $\|\tilde{\vartheta}'\|$ and γ , there exists a constant k_3 such that $\|X\| \leq k_3$. By varying the analysis above slightly, we can arrive at a similar bound for the system without hysteresis (i.e. $\alpha(t) \equiv 0$), but the reference signal is an infinite summation of

sinusoids, such as a raster or triangle wave. In such a case,

$$\dot{V} \leq -c_5 \|X\|^2 + c_6 \|X\| \sum_{k, k \notin \zeta}^{\infty} |C_{\eta_1}(s)S(s)| |S(s)| R_{1k}^2 \Big|_{s=jk\omega_1}$$

for some positive constants c_5 and c_6 , and R_{1k} represents the amplitude of the k th harmonic component in the reference.

6.5 Simulation and Experimental Results

In this Section, we present simulation and experimental results that illustrate and support the analytical results in Sections 6.3 and 6.4. Specifically, in Subsection 6.5.1, we show simulation results that demonstrate the influence of reference amplitude on the convergence for the case of one unknown frequency. Subsections 6.5.2 and 6.5.3 contain experimental results that deal with the cases of one and two unknown frequencies, respectively. These experimental results also provide direct support for the analysis in Section 6.4, because of the presence of hysteresis compensation error in the experimental system.

6.5.1 Simulation Results for the Case of One Unknown Frequency

We begin by verifying the analysis presented in Section 6.3.3, namely the restriction on the size of R_{11} . Recall that in order to prove stability of the closed-loop system (6.1), (6.4)-(6.5), and (6.8)-(6.11), we required the reference amplitude R_{11} to be sufficiently large relative to the size of the harmonic disturbances present in the system. In order to verify this, we present Fig. 6.4, which shows the results of a pair of simulations conducted on the vibrational model of our piezoelectric

nanopositioner (3.26), with

$$y_r(t) = R_{11} \sin(\omega_1 t)$$

$$\alpha(t) = 5 \sin(2\omega_1 t)$$

where $\omega_1 = 2\pi 100$, and R_{11} will be used as a variable. The servocompensator was designed accordingly with $\zeta = [1, 2]$. The stabilizing controller $D(s)$ was designed using frequency-domain techniques based on the frequency response of the plant, and was chosen as

$$D_p(s) = \frac{1.3(3.5 \times 10^3)^2}{s^2 + 1.6(3.5 \times 10^3)s + (3.5 \times 10^3)^2} \quad (6.43)$$

This controller was verified to stabilize the boundary layer system (6.12) over the working range of our adaptation variable σ . When the reference amplitude $R_{11} = 11$, we notice that the frequency estimate converges to the desired value of ω_1 . However, when the reference amplitude $R_{11} = 10$, the frequency estimate settles slightly below $2\omega_1$. This also results in a very large difference in tracking error, with essentially zero tracking error ($O(10^{-10})$) when $R_{11} = 11$, but a mean error of 2.45 when $R_{11} = 10$; thus our results from Section 6.3.3 are confirmed, with the value of R_r lying somewhere between 10 and 11.

6.5.2 Experimental Results for the Case of One Unknown Frequency

We will now experimentally demonstrate the effectiveness of the proposed controller on a commercial piezo-actuated nanopositioner (Nano OP-65, from Mad City Labs), whose vibration dynamics are given by (3.26). The hysteresis nonlinearity of the plant was identified using a quasi-static waveform of decreasing amplitude. A least-squares optimization routine was used to identify opti-

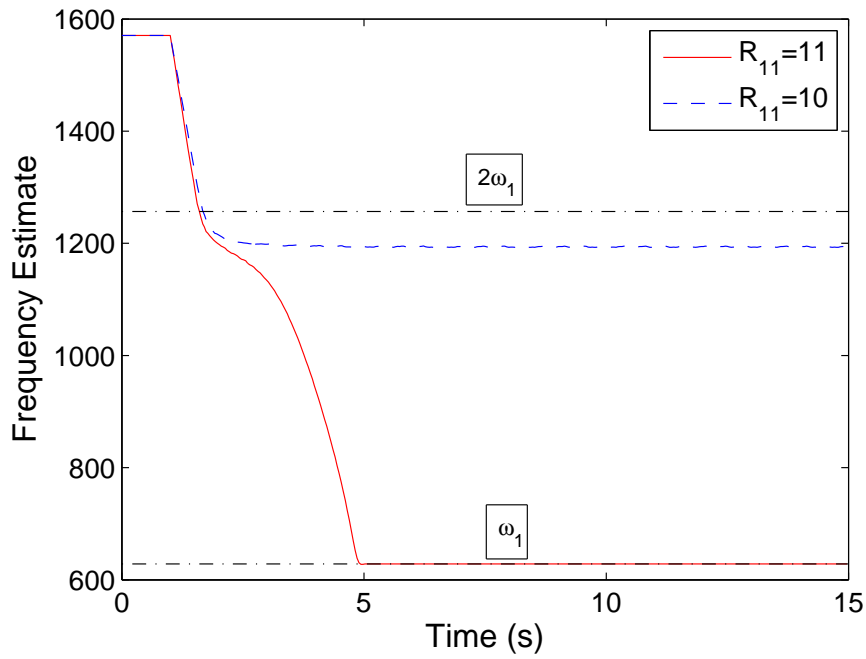


Figure 6.4: Simulation results on the model of the piezoelectric plant. Two simulations are presented, with $R_{11} = 10$ and $R_{11} = 11$.

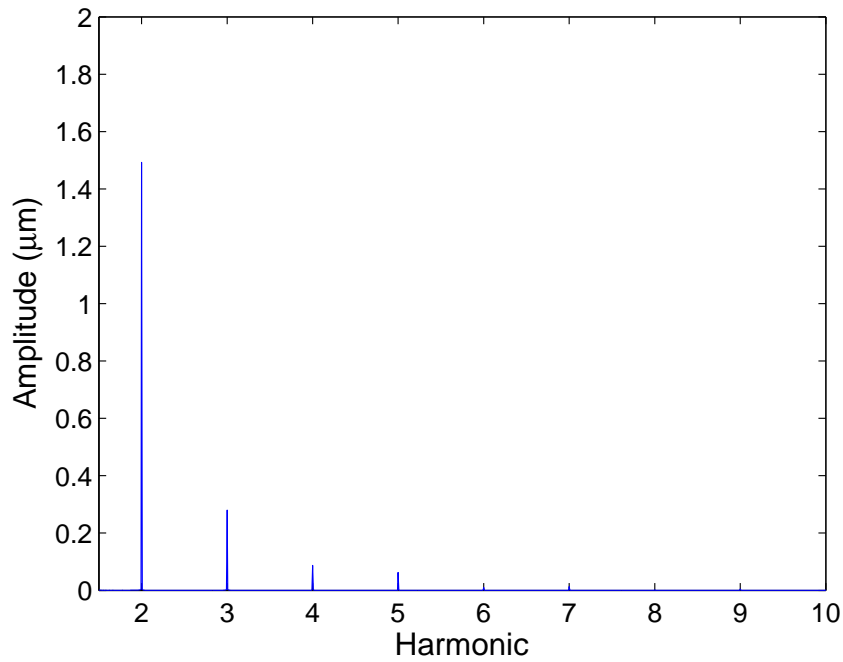


Figure 6.5: Output spectrum for nanopositioner used in experimental studies. Input to power supply is $3 \sin(2\pi 5) + 4 \text{ V}$. Primary harmonic is not shown, but has an amplitude of $25.2 \mu\text{m}$.

mal weights for a modified PI operator with 9 deadzone elements and 8 play operators, which was then used to calculate an approximate hysteresis inversion.

We tested the regulation performance of the proposed method through tracking experiments, using sinusoidal references from 5 to 200 Hz, along with a 5 Hz sawtooth signal. In order to understand the effectiveness of the proposed controller, we will compare the tracking results with an established method in nanopositioning tracking problems, Iterative Learning Control [38]. Our performance metrics will be the mean tracking error, defined as the mean of $|e(t)|$ at steady state, and the peak tracking error, defined by computing $\max |e(t)|$ over one period of the reference, then taking an average of this value over many periods.

For the sinusoidal references, we will employ two versions of our proposed controller; an indirect adaptive servocompensator (ASC) with the design vector $\zeta = [1]$, and a multi-harmonic indirect adaptive servocompensator (MHASC) with $\zeta = [1, 2, 3]$. Both controllers are based on the analysis of Section 6.3.3. The adaptation gains used were $\gamma = 0.003$ for the 5 and 25 Hz cases, $\gamma = 0.001$ for 50 Hz, and $\gamma = 0.0005$ for the 100 and 200 Hz experiments, where we have adjusted the adaptation gains to get similar settling times for each test.

The tracking results are presented in Table 6.1. We notice that the MHASC enjoys a consistent advantage over both the ILC controller and ASC controller. As the frequency of the reference trajectory increases, the ASC begins to overtake the ILC controller in performance, but is significantly behind at low frequency, indicating that the proposed controller's tracking performance is less sensitive to model uncertainties than ILC. At 200 Hz, we notice that the ASC has better mean-error performance than the MHASC, which is highly counter-intuitive. However, this can be explained by the design of the stabilizing controller. With a frequency of 200 Hz, the successive harmonics used in the MHASC mean that the servocompensator has a great effect on the stability margin of the system. For the ASC, with $\sigma = 2\pi 200$, the closed-loop system possesses a phase margin of

around 70° . However, the phase margin of the MHASC at this frequency is 25° . This causes the other harmonics of the hysteresis being amplified, and results in the higher tracking error.

Table 6.1: Tracking error results for proposed controllers (MHASC, ASC) and ILC. Results are presented as a percentage of the reference amplitude ($20 \mu\text{m}$).

	MHASC (%)		ASC (%)		ILC (%)	
	Mean	Peak	Mean	Peak	Mean	Peak
5 Hz	0.12	0.64	0.31	0.92	0.17	0.78
25 Hz	0.14	0.71	0.37	1.01	0.19	0.58
50 Hz	0.21	0.93	0.46	1.14	0.53	1.01
100 Hz	0.39	1.61	0.56	1.76	0.53	1.25
200 Hz	0.94	3.12	0.79	3.33	1.36	3.49

Figures 6.6 and 6.7 offer a closer look at the performance of the different methods at high and low frequencies. As the system approaches the gain crossover frequency near the resonant frequency of the plant, the effect of the hysteresis harmonics are amplified, resulting in the effect of the hysteresis becoming more pronounced. We can clearly observe the more prominent presence of higher harmonics in the 100 Hz signal as compared to the 5 Hz signal.

The second reference we test is a 5 Hz sawtooth signal, with the results shown in Fig. 6.8. We set the design parameter $\zeta = [1, 3, 5, 7, 9, 11]$ in order to approximate for the sawtooth signal, as well as compensate hysteresis. The frequency of the sawtooth wave was limited to 5 Hz, due to concerns with the stabilizing controller. The ILC controller's wide bandwidth nature makes it much better suited to compensating a sawtooth signal than our proposed method, and this results in an mean tracking error of 0.17% for ILC versus 0.28% for our proposed controller. However, the proposed method is still able to effectively compensate the sawtooth signal.

6.5.3 Experimental Results for the Case of Two Unknown Frequencies

We now present our experimental results on the performance of the proposed controller when y_r and α obey (6.6)-(6.7), as considered in Section 6.3.4. In order to simulate disturbances of the

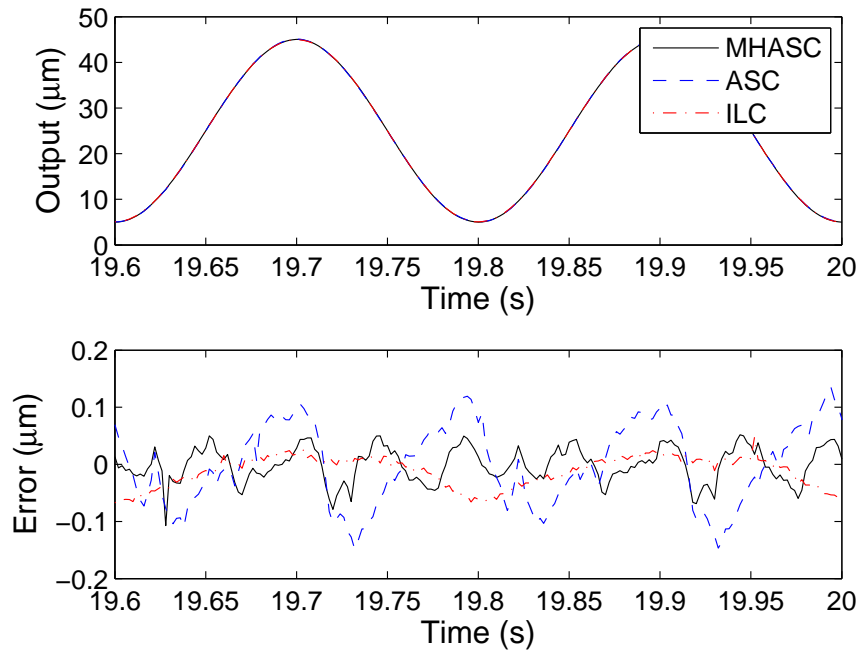


Figure 6.6: Experimental results for a 5 Hz sinusoidal signal.

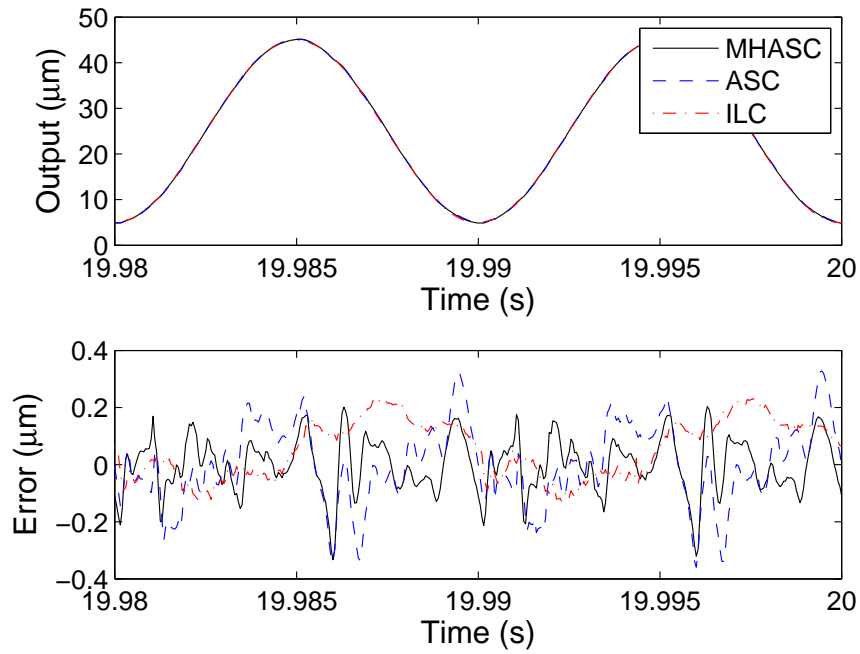


Figure 6.7: Experimental results for a 100 Hz sinusoidal signal.

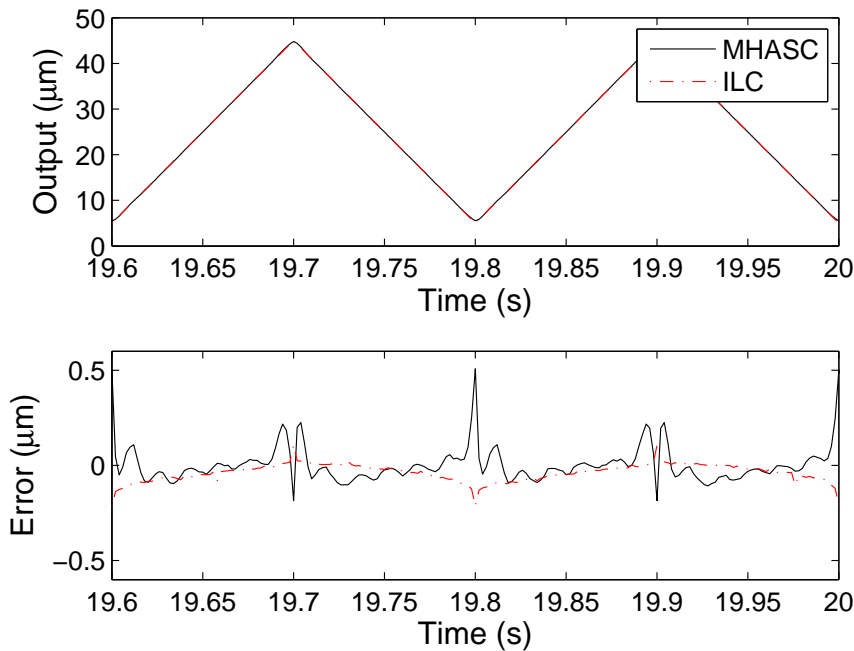


Figure 6.8: Experimental Results for a 5 Hz sawtooth signal.

form in (6.7), we inject a disturbance of $10\sin(2\pi 75t + \pi/2)$ into our Simulink block diagram just before the hysteresis inversion. The reference trajectory is $10\sin(2\pi 25t)$. For the purposes of control design, it is assumed that both frequencies are unknown, and in particular are not treated as known multiples of each other. The adaptation gains used were $\gamma_1 = \gamma_2 = 0.001$.

Fig. 6.9 shows the phase portrait of the adaptation variables for a number of initial conditions. Notice that the neutral line $\sigma_1 = \sigma_2$ is not crossed in any of the experiments. The trajectories of the adaptation variables seem to indicate the presence of three unstable equilibria on the neutral line; two saddles points near the top right and lower left of the figure, and an unstable node in the center of the figure. The trajectories of the system tend to initially converge to a manifold on which one variable is close to a desired frequency, seen in Fig. 6.9 as the horizontal and vertical lines. The system then evolves along this manifold to the stable equilibria. The time evolution of the tracking error and adaptation variables for one set of initial conditions is shown in Fig. 6.10. After the

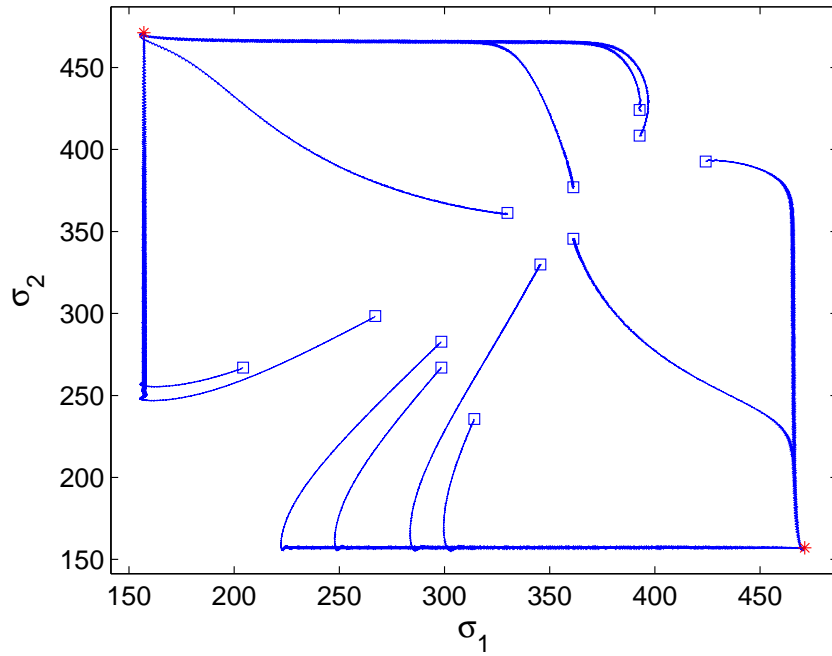


Figure 6.9: Phase portrait of σ_1 and σ_2 for various initial conditions. Desired equilibria are marked by the stars (red, in the lower right and top left), and initial conditions are marked by squares.

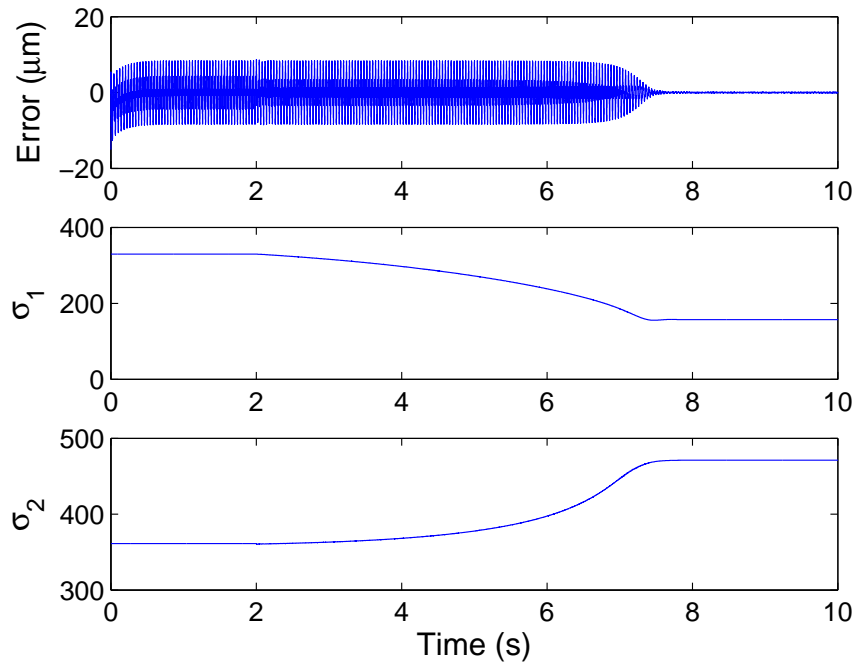


Figure 6.10: Plot of tracking error and adaptation variables vs. time. Adaptation is enabled at 2 s.

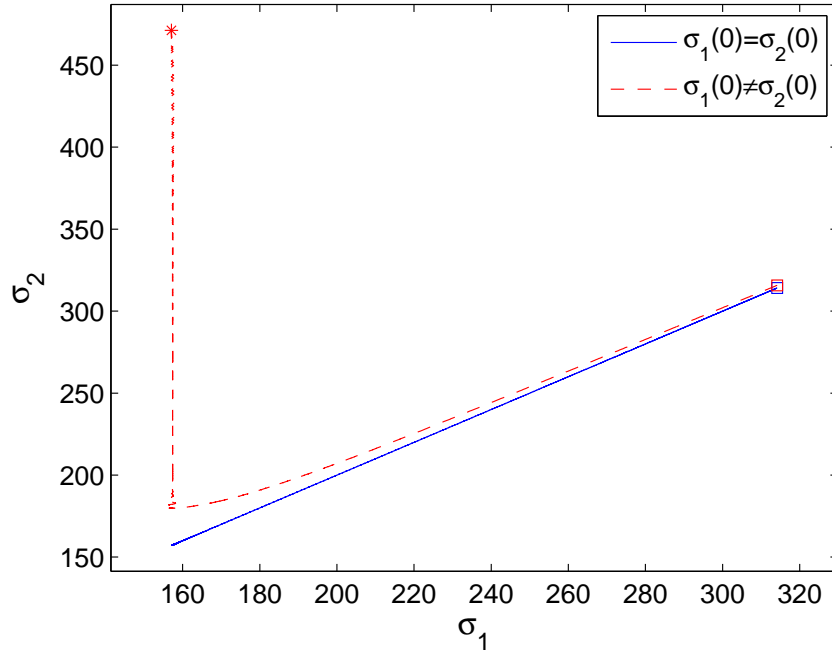


Figure 6.11: Phase portrait for experiments with $\sigma_1(0) = \sigma_2(0) = 2\pi 50$ and $\sigma_1(0) \neq \sigma_2(0)$ ($\sigma_1(0) = 2\pi 50$, $\sigma_2(0) = 2.01\pi 50$.)

adaptation is enabled at 2 s, the adaptation variables converge shortly after 7 s, which correlates with a rapid decrease in the tracking error. These experiments show the robustness of the proposed method to the error in hysteresis compensation.

We also confirm the existence of the degenerate case discussed in Remark 8 for equal adaptation gains. Fig. 6.11 shows the phase portrait of the adaptation variables under two different initial conditions. First, we set the initial conditions to $\sigma_1(0) = \sigma_2(0) = 2\pi 50$, which corresponds to the degenerate state of the system. We notice that the system evolves along the $\sigma_1 = \sigma_2$ line, and then the system converges to an undesirable equilibrium, resulting in a high tracking error. In the second experiment, $\sigma_1(0)$ is unchanged, but $\sigma_2(0) = 2.01\pi 50$. In this case, the system converges to the desired equilibrium point.

Chapter 7

Stability of Systems with Hysteresis without Hysteresis Inversion: an LMI Approach

7.1 Introduction

In this dissertation, our results have focused on controlling systems with hysteresis in tracking problems. In particular, we have proved that the states of the system remain bounded when hysteresis is present in the system. Other results in the literature, such as sliding-mode control [39], adaptive control [33], two-degree-of-freedom control [47], and many more [38, 49] have proved similar results. In addition, our results so far have required the implementation of hysteresis inversion to prove stability of our system with hysteresis. Hysteresis inversion, while normally very effective, can be computationally intensive, and can have some adverse effects on the performance of servocompensator-controlled systems, which we will explore later in this Chapter.

A new wave of research over the past five years has focused on direct analysis of systems with hysteresis, based on the mathematical formulations of the hysteresis operators. These works have provided some analytical results showing the stability of systems with hysteresis and convergence of the tracking error to zero, and importantly, can do so without hysteresis inversion or requiring the hysteresis effect to be small. Such a result was proved in [83], where an LMI framework is utilized to provide sufficient conditions for the stability and tracking error convergence for a PID-controlled second-order system preceded by a modified PI operator. In [84], stability and

tracking error convergence of a non-dynamic plant modeled by a Presiach operator was proved using monotonic properties of the operator. The authors of [85] proved closed-loop stability for a system involving a PID-controlled second-order system preceded by a general hysteresis operator, and provided guidelines on the selection of controller gains.

One weakness of these results is that many are proved for dynamic systems of second order or lower. Similar results for n th-order systems have typically relied on passivity conditions. One of the most well known results in this area is reported in [86], where a Presiach operator is shown to be dissipative. This is then combined with traditional passivity results to show the finite-gain stability of the system. Dissipative properties have also been shown for the PI operator [28] and the Duhem operator [87]. A shortcoming of these results is that they are able to only show boundedness, even for constant reference trajectories. In addition, the conditions required for passivity are not satisfied by many plants and controllers. Outside of passivity focused results, an interesting contribution is from [88], where tight input-output stability bounds are shown for systems with play operators without explicit passivity assumptions. Finally, in [89], stability of an n -dimensional system is proved under an LMI condition; however, this result did not consider any controller, and furthermore, did not show that tracking error could be regulated.

In this Chapter, we discuss the stability and tracking error convergence of a system with hysteresis using a general feedback controller containing an integral action. It is assumed that the hysteresis is modeled by a PI operator. The theory of switched systems, in particular, that of the common Lyapunov function [58], and a linear matrix inequality (LMI) condition will be used to prove that the tracking error and state vector converge exponentially to zero for a constant reference. The principal contribution of this work is to present sufficient conditions (in the form of an LMI) for the regulation of the closed-loop system in terms of the hysteresis parameters, without requiring the hysteresis to be small. As we will see, the presence of an integral action is crucial to the

formulation of our LMI condition. Comparing our LMI results to those achieved in [89] and [83], our framework can handle minimum-phase systems of arbitrary order, along with a wide class of controllers. In particular, we will show the stability of servocompensator-controlled systems with hysteresis without using hysteresis inversion.

We then connect our LMI result to the aforementioned passivity results, by demonstrating that if the system obeys a certain positive real condition, a solution to the LMI problem can be found analytically. In addition, we apply our LMI results to show that servocompensator-based controllers can stabilize systems with hysteresis, without requiring inversion of the hysteresis. Our simulation results then confirm the effectiveness of the LMI condition at predicting the global convergence of the tracking error.

We then verify our results through experiments conducted on a commercial nanopositioner. These experiments focused on comparing the performance of servocompensator-based controllers with and without hysteresis inversion. We first verify the LMI condition presented in the paper, in order to prove stability of the system. Our experimental results indicate that servocompensator-based controllers without hysteresis inversion can achieve half the mean tracking error as that achieved by the same control method with inversion, while also being less computationally intensive.

7.2 Sufficient Conditions for Stability in Systems with Hysteresis

Consider an n -dimensional linear system with transfer function,

$$\mathbb{G}_p(s) = \frac{k(s^m + b_{m-1}s^{m-1} + \dots + b_1s + b_0)}{s^n + a_{n-1}s^{n-1} + \dots + a_1s + a_0}, \quad m \leq n \quad (7.1)$$

with input $u(t)$ and output $y(t)$. We will assume that this transfer function is minimum phase. Our control objective is to regulate the output of the cascade connection of a PI operator (2.3) and $\mathbb{G}_p(s)$, illustrated in Fig. 6.3. In particular, we will design the input $v(t)$ to the hysteresis to stabilize the resulting feedback connection, and also drive y to a constant reference y_r . Recall that it is conventional to include the $r_0 = 0$ term in the definition of the hysteresis operator, even though this term results in simply a linear gain. For our work, we will separate this term from the nonzero radii play operators, thus

$$u(t) = \theta_0 v(t) + \theta_h^T W_h(t) \quad (7.2)$$

We will consider a normal-form state-space representation for the transfer function $\mathbb{G}_p(s)$ [64],

$$\dot{z}(t) = Fz(t) + Gx_1(t) \quad (7.3)$$

$$\dot{x}(t) = A_0x(t) + B(u(t) + \lambda x(t) + \psi z(t)) \quad (7.4)$$

$$y(t) = Cx = x_1(t) \quad (7.5)$$

where $u(t)$ obeys (7.2). The matrices $F \in \mathfrak{R}^{m \times m}$, $G \in \mathfrak{R}^m$, $A_0 \in \mathfrak{R}^{p \times p}$, and $B \in \mathfrak{R}^p$ are given by

$$F = \begin{bmatrix} 0 & 1 & \cdots & 0 \\ 0 & & \ddots & 0 \\ 0 & \cdots & \cdots & 1 \\ -b_0 & -b_1 & \cdots & -b_{m-1} \end{bmatrix}, \quad G = \begin{bmatrix} 0 \\ \vdots \\ 1 \end{bmatrix},$$

$$A_0 = \begin{bmatrix} 0 & 1 & \cdots & 0 \\ 0 & & \ddots & 0 \\ 0 & \cdots & \cdots & 1 \\ 0 & \cdots & 0 & 0 \end{bmatrix}, \quad B = \begin{bmatrix} 0 \\ \vdots \\ k \end{bmatrix}$$

and $\lambda \in \mathfrak{R}^{1 \times p}$, $\psi \in \mathfrak{R}^{1 \times m}$ are row vectors.

Remark 10 *For simplicity but without loss of generality, we will assume in the following equations that $\theta_0 = 1$. This is because the gain of the hysteresis operator can be rolled into the DC gain of the linear dynamics. In order to transform a system where $\theta_0 \neq 1$ into the form considered here, we multiply k in B by θ_0 , and divide the elements of θ_h , λ , and ψ by the same value.*

We will consider a general linear controller to control (7.2), (7.3)-(7.5). The controller includes a dynamic compensator represented in the state-space form,

$$\dot{\eta}(t) = C^* \eta(t) + B^* (x_1 - y_r) \quad (7.6)$$

with $C^* \in \mathfrak{R}^{q \times q}$ and $B^* \in \mathfrak{R}^q$. Here we use the tracking error $x_1 - y_r$ as an input to the controller; however, our analysis could be adjusted to accommodate different inputs. We will also require our

linear controller to contain an integral action,

$$\dot{\sigma}(t) = x_1 - y_r \quad (7.7)$$

Using (7.6) and (7.7), we can define our control signal to the plant/hysteresis operator;

$$v(t) = -K_1 z(t) - K_2 x(t) - K_3 \eta(t) - K_4 \sigma(t) \quad (7.8)$$

where $K_1 \in \mathfrak{R}^{1 \times m}$, $K_2 \in \mathfrak{R}^{1 \times p}$, $K_3 \in \mathfrak{R}^{1 \times q}$, and $K_4 \in \mathfrak{R}$ are constant gains. Applying (7.2) and (7.6)-(7.8) to (7.3)-(7.5) yields,

$$\begin{bmatrix} \dot{z}(t) \\ \dot{x}(t) \\ \dot{\eta}(t) \\ \dot{\sigma}(t) \end{bmatrix} = \begin{bmatrix} F & GC & 0 & 0 \\ -B(K_1 - \psi) & A_0 - B(K_2 - \lambda) & -BK_3 & -BK_4 \\ 0 & B^*C & C^* & 0 \\ 0 & C & 0 & 0 \end{bmatrix} \begin{bmatrix} z(t) \\ x(t) \\ \eta(t) \\ \sigma(t) \end{bmatrix} + \begin{bmatrix} 0 \\ B\theta_h^T W_h[v; W_h(0)](t) \\ -B^*y_r \\ -y_r \end{bmatrix} \quad (7.9)$$

As the PI operator is continuous, the system (7.2), (7.8)-(7.9) is well-posed, and possesses a continuous and unique solution, which was proved in [41]. Next, define the coordinate transforms

$$\tilde{z}(t) = z(t) - [1, \mathbf{0}]^T \frac{1}{b_0} y_r \quad (7.10)$$

$$\tilde{x}(t) = x(t) - C^T y_r \quad (7.11)$$

where $\mathbf{0}$ is an $m - 1$ dimensional row vector of zeros. With these transforms, Eq. (7.9) then becomes

$$\begin{bmatrix} \dot{\tilde{z}}(t) \\ \dot{\tilde{x}}(t) \\ \dot{\eta}(t) \\ \dot{\sigma}(t) \end{bmatrix} = \begin{bmatrix} F & GC & 0 & 0 \\ -B(K_1 - \psi) & A_0 - B(K_2 - \lambda) & -BK_3 & -BK_4 \\ 0 & B^*C & C^* & 0 \\ 0 & C & 0 & 0 \end{bmatrix} \begin{bmatrix} \tilde{z}(t) \\ \tilde{x}(t) \\ \eta(t) \\ \sigma(t) \end{bmatrix} + \begin{bmatrix} 0 \\ B\theta_h^T W_h[v; W_h(0)](t) + Bc_0 y_r \\ 0 \\ 0 \end{bmatrix} \quad (7.12)$$

where c_0 is a constant that depends on the system matrices and control gains, which appears due to the coordinate transform. We will now define

$$\alpha(t) = -K_4 \sigma(t) + \theta_h^T W_h[v; W_h(0)](t) + c_0 y_r \quad (7.13)$$

This definition is made in order to use Lyapunov analysis to show that all states converge to the origin, since the state of the integrator will not necessarily go to zero in a system with hysteresis, even if $y_r = 0$. This transform will also remove the effect of $c_0 y_r$ from (7.12), as y_r is constant. The derivative of $\alpha(t)$ is given by

$$\dot{\alpha}(t) = -K_4 C \tilde{x}(t) + \theta_h^T \dot{W}_h[v; W_h(0)](t) \quad (7.14)$$

where

$$\dot{W}_h[v; W_h(0)](t) = [\dot{P}_{r_1}[v; W_1(0)](t), \dots, \dot{P}_{r_m}[v; W_m(0)](t)]^T \quad (7.15)$$

The derivative of a play operator is in general discontinuous, since the switching between play and linear regions can cause jumps in the value of $\dot{P}_{r_i}[v; W(0)](t)$. Let $\Pi(t)$ denote the set of all play operators $P_{r_i}[v; W(0)](t)$ that lie in a linear region at time t , and let Π^c denote its complement. We therefore have a piecewise expression for \dot{P}_{r_i} , given by

$$\dot{P}_{r_i}[v; W_i(0)](t) = \begin{cases} \dot{v}, & \text{if } i \in \Pi(t) \\ 0, & \text{if } i \in \Pi^c(t) \end{cases} \quad (7.16)$$

where

$$\begin{aligned} \dot{v}(t) = & -K_1[F\tilde{z}(t) + GC\tilde{x}(t)] - K_2[-B(K_1 - \psi)\tilde{z}(t) \\ & + (A_0 - B(K_2 - \lambda))\tilde{x}(t) - BK_3\eta(t) + B\alpha(t)] \\ & - K_3[C^*\eta(t) + B^*C\tilde{x}(t)] - K_4[C\tilde{x}(t)] \end{aligned} \quad (7.17)$$

Let Θ_h be the set of all numbers that can be reached by adding together elements of θ_h . Next, define $\bar{\theta}_h(t) \in \Theta_h$ as the summation of weights for play operators in the linear region, i.e.

$$\bar{\theta}_h(t) = \left[\sum_i \theta_{hi} : i \in \Pi(t) \right] \quad (7.18)$$

Define the state vector

$$\gamma(t) = [\tilde{z}^T(t), \tilde{x}^T(t), \eta^T(t), \alpha(t)]^T$$

Note that \dot{v} can be expressed as a constant vector multiplying the state vector of the system, i.e.

$\dot{v} = K_v \gamma$. Using this definition with (7.13) and (7.14), we transform (7.12) into

$$\dot{\gamma}(t) = \begin{bmatrix} F & GC & 0 & 0 \\ -B(K_1 - \psi) & A_0 - B(K_2 - \lambda) & -BK_3 & B \\ 0 & B^*C & C^* & 0 \\ 0 & -K_4C & 0 & 0 \end{bmatrix} \gamma(t) + \begin{bmatrix} 0 \\ 0 \\ 0 \\ \bar{\theta}_h(t)K_v\gamma(t) \end{bmatrix} \quad (7.19)$$

Alternatively, we write (7.19) in a compact form,

$$\dot{\gamma}(t) \triangleq (\Sigma_0 + \bar{\theta}_h(t)\bar{B}K_v)\gamma(t) \quad (7.20)$$

where

$$\bar{B} = [0, 1]^T$$

where 0 here is an $m + p + q$ dimensional row vector of zeros. As the states γ can be expressed as simple functions of the states of (7.9) and the hysteresis state $W_h(t)$, we know that the solution to the above system is well-posed, and that γ is continuous. Note also that $\bar{\theta}_h(t) \in \Theta_h$, and thus $\bar{\theta}_h$ takes values in a set of finite cardinality; therefore, we can interpret (7.20) as a switched system, where the switching is governed by the states of the play operators in (7.2). The stability of such a

system can be guaranteed through an LMI condition [58],

$$(\Sigma_0 + \bar{\theta}_h \bar{B}K_v)^T P + P(\Sigma_0 + \bar{\theta}_h \bar{B}K_v) < 0, \forall \bar{\theta}_h \in \Theta_h$$

where $P > 0$. Such a condition would imply that $V(\gamma) = \gamma^T P \gamma$ is a common Lyapunov function for (7.20), where $\dot{V} < 0, \forall \gamma \neq 0$. However, since the only element that actually changes is $\bar{\theta}_h$, from the results of [90] a sufficient condition for the existence of such a P is that

$$\begin{aligned} (\Sigma_0 + \min(\Theta_h) \bar{B}K_v)^T P + P(\Sigma_0 + \min(\Theta_h) \bar{B}K_v) < 0, \\ (\Sigma_0 + \max(\Theta_h) \bar{B}K_v)^T P + P(\Sigma_0 + \max(\Theta_h) \bar{B}K_v) < 0 \end{aligned} \quad (7.21)$$

Similarly, if a P can be found such that

$$\begin{aligned} (\Sigma_0 + \min(\Theta_h) \bar{B}K_v)^T P + P(\Sigma_0 + \min(\Theta_h) \bar{B}K_v) + 2\Lambda P < 0, \\ (\Sigma_0 + \max(\Theta_h) \bar{B}K_v)^T P + P(\Sigma_0 + \max(\Theta_h) \bar{B}K_v) + 2\Lambda P < 0 \end{aligned} \quad (7.22)$$

where $\Lambda \in \Re > 0$ then $\dot{V} < -2\Lambda V$, which implies that (7.20) is exponentially stable, and the tracking error converges to zero with decay rate of at least Λ [90].

Remark 11 *One extension of this work would be to consider a modified PI operator (2.16) for the hysteresis model. This operator can be fit into our existing framework by extending the definition of $\bar{\theta}_h$, multiplying the result of the current definition with the summation of the weights of the active deadzone operators.*

7.2.1 Specialization to Positive-Real Systems

By imposing a positive real assumption on the system, we can arrive at a stronger stability result.

Consider the closed-loop system (7.3)-(7.5), (7.7), with

$$v(t) = -K_1 z(t) - K_2 x(t) - K_4 \sigma(t) \quad (7.23)$$

Let the system

$$\begin{aligned} \begin{bmatrix} \dot{\tilde{z}} \\ \dot{\tilde{x}} \end{bmatrix} &= \Sigma^* \begin{bmatrix} \tilde{z} \\ \tilde{x} \end{bmatrix} + \mathbb{B} u^* \\ &\triangleq \begin{bmatrix} F & GC \\ -B(K_1 - \psi) & A_0 - B(K_2 - \lambda) \end{bmatrix} \begin{bmatrix} \tilde{z} \\ \tilde{x} \end{bmatrix} + \begin{bmatrix} 0 \\ Bu^* \end{bmatrix} \end{aligned} \quad (7.24)$$

$$y = \tilde{\zeta}_1 \triangleq \mathbb{C} \begin{bmatrix} \tilde{z} \\ \tilde{\zeta} \end{bmatrix} \quad (7.25)$$

be positive real [64], where \tilde{z} and \tilde{x} are defined as in (7.10)-(7.11), and $u^* \in \mathfrak{X}$ will be defined momentarily. Then, there exists a symmetric positive definite matrix P^* such that

$$P^* \Sigma^* + \Sigma^{*T} P^* = -Q$$

$$P^* \mathbb{B} = \mathbb{C}^T$$

where Q is symmetric and positive definite. This system represents the dynamics portion of our model which has been rendered positive-real by state feedback. This condition is similar to the assumption on the dynamics in [86], where the dynamics of a cascaded controller and a smart material actuator are assumed to be passive. Indeed, for LTI systems, the notions of passivity and

positive realness are interchangeable [91]. Note that the controller is not included in this positive real condition. We will now show that under this positive real condition, and with only integral control, the LMI (7.22) must have a solution.

Let u^* be defined as

$$u^*(t) = \alpha(t) = -K_4\sigma(t) + \theta_h^T W_h[v; W_h(0)](t) + c_0 y_r$$

where the integrator output σ is governed by

$$\dot{\sigma}(t) = \mathbb{C}[\tilde{z}^T, \tilde{x}^T]^T$$

Using this definition together with (7.23) and (7.24), we notice that we can recover the closed-loop system defined in (7.19) (excluding the terms related to η). Let $\tilde{\chi} = [\tilde{z}^T, \tilde{x}^T]^T$ and consider the Lyapunov function candidate

$$V(\tilde{\chi}, \alpha) = \beta \tilde{\chi}^T(t) P^* \tilde{\chi}(t) + 1/2 \alpha^2(t) \tag{7.26}$$

$$= \begin{bmatrix} \tilde{\chi}(t) \\ \alpha(t) \end{bmatrix}^T \begin{bmatrix} \beta P^* & 0 \\ 0 & 1/2 \end{bmatrix} \begin{bmatrix} \tilde{\chi}(t) \\ \alpha(t) \end{bmatrix} \tag{7.27}$$

where α is defined as in (7.13). The derivative of V can be written as (using (7.24)),

$$\begin{aligned}
\dot{V}(\tilde{\chi}, \alpha) &= \beta \tilde{\chi}^T(t) P^* [\Sigma^* \tilde{\chi}(t) + \mathbb{B} \alpha(t)] + \beta [\Sigma^* \tilde{\chi}(t) + \mathbb{B} \alpha(t)]^T P^* \tilde{\chi}(t) \\
&\quad - \alpha(t) K_4 \mathbb{C} \tilde{\chi}(t) + \alpha(t) \theta_h^T \dot{W}_h[v; W_h(0)](t) \\
&= -\beta \tilde{\chi}^T(t) Q \tilde{\chi}(t) + \alpha(t) \tilde{\chi}^T(t) [\beta 2P^* \mathbb{B} - K_4 \mathbb{C}^T] \\
&\quad + \alpha(t) \bar{\theta}_h(t) (-K^* \Sigma^* \tilde{\chi}(t) - K^* \mathbb{B} \alpha(t) - K_4 \mathbb{C} \tilde{\chi}(t))
\end{aligned} \tag{7.28}$$

where $K^* = [K_1, K_2]$. Let β be defined as

$$\beta = K_4/2 \tag{7.29}$$

and let $\mathbb{F} = -K^* \Sigma^* - K_4 \mathbb{C}$. We can then rewrite \dot{V} in the matrix form

$$\dot{V}(\tilde{\chi}, \alpha) = -1/2 \begin{bmatrix} \tilde{\chi}(t) \\ \alpha(t) \end{bmatrix}^T \begin{bmatrix} K_4 Q & \bar{\theta}_h(t) \mathbb{F}^T \\ \bar{\theta}_h(t) \mathbb{F} & 2\bar{\theta}_h K^* \mathbb{B} \end{bmatrix} \begin{bmatrix} \tilde{\chi}(t) \\ \alpha(t) \end{bmatrix} \tag{7.30}$$

Define $\zeta = [\tilde{\chi}^T, \alpha]^T$, and

$$X = \begin{bmatrix} K_4 Q & \bar{\theta}_h(t) \mathbb{F}^T \\ \bar{\theta}_h(t) \mathbb{F} & 2\bar{\theta}_h K^* \mathbb{B} \end{bmatrix}$$

Let S equal the Schur compliment of X , i.e.

$$S = 2\bar{\theta}_h(t) K^* \mathbb{B} - \bar{\theta}_h(t)^2 F [K_4 Q]^{-1} F^T \tag{7.31}$$

It is well known that X is positive definite if and only if both $K_4 Q$ and $S \in \mathfrak{R}$ are positive definite.

Assuming that $\bar{\theta}_h > 0$, we can lower bound S with the expression

$$S \geq \left[2K^*\mathbb{B} - \frac{1}{K_4\lambda_{\min}(Q)} \|\theta_h\|_1 F^T F \right] \bar{\theta}_h(t) \quad (7.32)$$

Note that this equation is independent of the solution to the Lyapunov equation P^* ; therefore, if K^* is such that $K^*\mathbb{B} > 0$, we can always find a Q (and therefore a P^*) such that S is positive definite for all $\bar{\theta}_h > 0$. This implies that X is positive definite, and therefore there must exist a sufficiently small Λ such that $X > \Lambda P$, and therefore that P and Λ satisfy the LMI condition (7.22).

We can now compare our results here with the passivity results achieved in [86] and in similar references such as [87]. In [86], dissipativity (a generalization of passivity) of the presiach operator is shown between the input and derivative of the output of the operator. In both our results here and the results achieved in [86], by assuming the dynamics are positive real or passive, the properties of the hysteresis operator under consideration allow us to prove stability of the system without any further restrictions on the hysteresis. The principal difference is that because dissipativity can only be shown from the input to the derivative of the output of a hysteresis operator, passivity-based results cannot prove that the tracking error converges to zero, even for constant reference signals. However, our results require that $K^*\mathbb{B} > 0$ and $K_4 > 0$, which may not be satisfied for all positive real systems.

7.3 Stability of Servocompensators in Systems with Hysteresis without Hysteresis Inversion

With our LMI condition in hand, we can now prove the stability of the servocompensator controlled closed-loop system with hysteresis, without including hysteresis inversion. The servocompensator

fits into the controller framework described in (7.6), where C^* is neutrally stable, with eigenvalues located on the imaginary axis. B^* is chosen to ensure that the pair (C^*, B^*) is controllable. We now assume that the reference signal is generated by a neutrally stable exosystem,

$$\dot{w}(t) = Sw(t) \tag{7.33}$$

$$y_r(t) = Ew(t) \tag{7.34}$$

Let us assume that y_r is periodic with period T . We next set up the error coordinate transform,

$$\tilde{z}(t) = z(t) - z^*(t) \tag{7.35}$$

$$\tilde{x}_1(t) = x_1(t) - y_r(t)$$

$$\vdots$$

$$\tilde{x}_n(t) = x_n(t) - y_r^{(n-1)}(t) \tag{7.36}$$

where $z^*(t)$ is the steady state solution of

$$\dot{z}^*(t) = Fz^*(t) + Gy_r(t) \tag{7.37}$$

and the notation $f^{(i)}(t)$ denotes the i th derivative with respect to time. This transform changes the γ dynamics into

$$\dot{\gamma}(t) = \begin{bmatrix} F & GC & 0 & 0 \\ -B(K_1 - \psi) & A_0 - B(K_2 - \lambda) & -BK_3 & B \\ 0 & B^*C & C^* & 0 \\ 0 & -K_4C & 0 & 0 \end{bmatrix} \gamma(t) + \begin{bmatrix} 0 \\ -By_r^{(n)}(t) \\ 0 \\ \bar{\theta}_h BK_v \gamma(t) + c_0 y_r^{(1)}(t) \end{bmatrix} \quad (7.38)$$

Let us assume that we have identified a P such that (7.22) is satisfied for a given Λ . We can then use $V(\gamma) = \gamma^T P \gamma$ as a Lyapunov function candidate, the derivative of which obeys

$$\dot{V}(\gamma) = -2\Lambda V(\gamma) + 2\gamma^T P [0, -B^T y_r^{(n)}(t), 0, c_0 y_r^{(1)}(t)]^T \quad (7.39)$$

$$\begin{aligned} &< -2\Lambda \lambda_{\min}(P) \|\gamma\|^2 \\ &+ 2\lambda_{\max}(P) \|\gamma\| \| [0, -B^T y_r^{(n)}(t), 0, c_0 y_r^{(1)}(t)] \| \end{aligned} \quad (7.40)$$

where $\|\cdot\|$ denotes the Euclidian norm. We can see from this equation that there must exist a sufficiently large γ such that $\dot{V} < 0$; therefore γ enters a bounded positively invariant set and γ remains bounded for all t . However, the disturbance rejection properties of the servocompensator will allow us to draw some further conclusions regarding the performance of the system if we impose a periodicity assumption.

Assumption 14 *The steady-state trajectory of $\gamma(t)$ is T -periodic.*

Remark 12 *Though theoretical results are lacking, many experimental results reported in the literature have shown that systems with hysteresis seem to possess T -periodic solutions when driven by T -periodic references, regardless of whether inversion is used or not [39, 47]. Therefore, we are presented with a tradeoff in our theoretical results between guaranteeing periodicity of the solutions when inversion is used, and ineffectiveness of the servocompensator when inversion is not used.*

Utilizing Assumption 14, we can now investigate the steady state tracking error, $\tilde{x}_1(t)$. Letting $T = 2\pi/\omega$, we can write $\tilde{x}_1(t)$ in a series form as

$$\tilde{x}_1(t) = \sum_{i=1}^{\infty} R_i \sin(i\omega t + \phi_i) \quad (7.41)$$

Let us assume that the matrix C^* in our servocompensator (7.6) has been chosen such that its eigenvalues are located at $\pm jk\omega$, $k \in \rho$, where ρ is a finite-element vector of whole numbers. Because $\tilde{x}_1(t)$ is the input to (7.6), the servocompensator's error regulation properties will force all components of $\tilde{x}_1(t)$ whose internal models are contained in C^* to have zero amplitude at the steady state. Therefore, $R_i = 0, \forall i \in \rho$ in (7.41).

7.4 Simulation Example: Verification of the LMI condition

We now demonstrate the feasibility and effectiveness of our LMI condition with a simulation example. Let us consider a linear system,

$$\mathbb{G}_p(s) = \frac{\omega_n^2}{s^2 + 2\zeta\omega_n s + \omega_n^2} \quad (7.42)$$

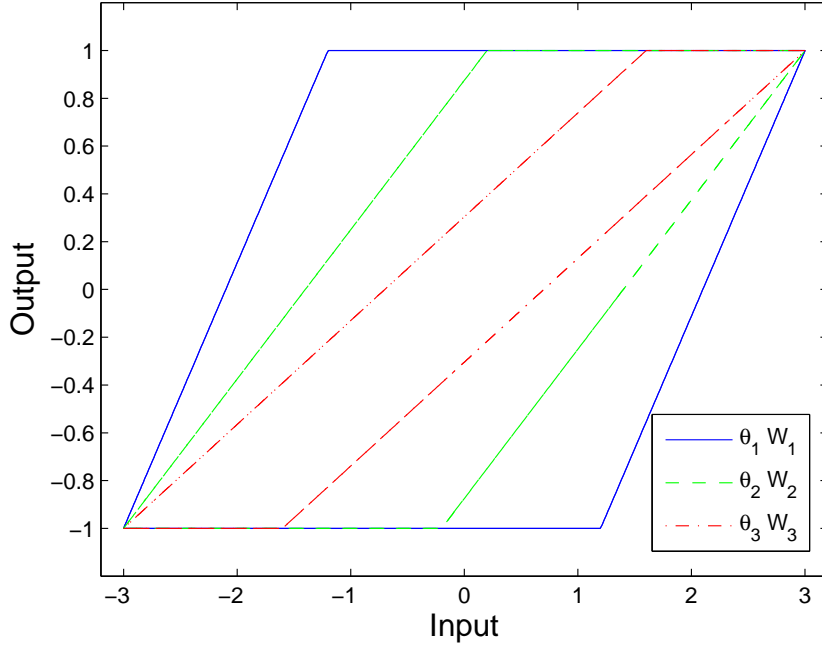


Figure 7.1: Hysteresis loops for play operators with equalized relative gains, where r is equal to 0.7, and $\mu = 3$.

where $\zeta = 0.5$ and $\omega_n = 1$. $\mathbb{G}_p(s)$ is preceded by a PI operator with $\mathbf{r} = [0, r, 2r, 3r]$, where r will be considered as a variable. The weights θ of the operator will be considered a function of r . In particular, for the play operator P_{r_i} , $1 \leq i \leq 3$, θ_i will obey

$$\theta_i(r_i) = \frac{2}{2\mu - 2r_i} \quad (7.43)$$

where we introduce μ as a design parameter. This choice of θ_i is chosen to make sure the relative gains of the play operators remain constant. By this, we mean that for any $r_i < \mu$, if the input v to $P_{r_i}[v; W_i(0)](t)$ is cycled periodically from $v_{\min} = -\mu$ to $v_{\max} = \mu$, then $\theta_i P_{r_i}[v_{\max}; W_i(0)](t) = 1$. We have illustrated this idea in Fig. 7.1 for $\mu = 3$. The exception to this rule will be θ_0 , which we

will fix at one. This cascade of a PI operator and $\mathbb{G}_p(s)$ will be controlled by an integral controller,

$$\dot{\sigma}(t) = y(t) - y_r \quad (7.44)$$

$$v(t) = -0.25\sigma(t) \quad (7.45)$$

where $y(t)$ is the output of $\mathbb{G}_p(s)$, and y_r is a constant reference signal. Since our LMI results prove global stability, we will set y_r to be 100. The system described above can be easily fit into the LMI framework (7.22), with

$$\Sigma_0 + \min(\bar{\Theta}_h(r))B^*K_v = \begin{bmatrix} 0 & 1 & 0 \\ -\omega_n^2 & -2\zeta\omega_n & 1 \\ -0.25 & 0 & 0 \end{bmatrix},$$

$$\Sigma_0 + \max(\bar{\Theta}_h(r))B^*K_v = \begin{bmatrix} 0 & 1 & 0 \\ -\omega_n^2 & -2\zeta\omega_n & 1 \\ -0.25(1 + \|\theta_h(r)\|_1) & 0 & 0 \end{bmatrix}$$

where $\|\cdot\|_1$ denotes the 1-norm.

To test the viability of our proposed method, we will now begin to increase the value of r until our LMI condition either becomes infeasible, or produces a result that cannot guarantee stability. Increasing the value of r makes the hysteresis loops wider, meaning that the control becomes less and less effective at compensating the system. When $r = 0.74$, both LMIs (7.21) and (7.22) return results that cannot guarantee stability. We then simulate our system, increasing r each simulation until the tracking error no longer converges to zero. We then denote this value of r as r_{\max} . For our setup described here, $r_{\max} = 0.8$, with the system entering a limit cycle rather than converging to zero. Our LMI framework is therefore fairly effective, as it is able to guarantee stability up to

92.5% of r_{\max} .

One behavior worth noting is that the value of r_{\max} observed in simulation can vary with the value of y_r . For example, if $y_r = 3$, r can be increased to 0.89 before instability occurs. This would indicate that there is a region of attraction for this system, inside which the tracking error converges to zero. This indicates that the conservatism of our LMI condition is dependent on the value of the reference input y_r .

7.5 Applications to Nanopositioning Control

We now confirm our theoretical results with experiments. We performed a series of tracking experiments on a commercial nanopositioner (shown in Fig.3.3), and compared the results under different control schemes. Online control implementation and data collection was provided by a dSPACE platform (DS1104). The nanopositioner was modeled using the same techniques as those presented in Section 3.4.1, as a cascade of dynamics and a modified PI operator. The radii of the modified PI operator were not changed from those in Section 3.4.1, however the weights were re-identified as

$$\hat{\theta}_h = [0.694, 0.196, 0.041, 0.050, 0.040, \\ 0.050, 0.023, 0.054]$$

for the play operator, and the weights of the deadzones were

$$\hat{\theta}_d = [1.056, 0.650, 0.327, 0.432, 9.130, \\ -1.138, -0.154, -0.787, -0.296]$$

Our vibrational dynamics were modeled by a 4th-order transfer function,

$$\mathbb{G}_p(s) = \frac{4.7 \cdot 10^{17}}{s^4 + 1.6 \cdot 10^4 s^3 + 6.6 \cdot 10^8 s^2 + 5.0 \cdot 10^{12} s + 8.3 \cdot 10^{16}} \quad (7.46)$$

In order to improve computation accuracy we used a balanced state-space realization [65] of the system (7.46). This results in the model

$$\begin{aligned} \dot{x}(t) = & 1.0 \times 10^4 \begin{bmatrix} -0.024 & 1.614 & -0.126 & 0.061 \\ -1.614 & -0.266 & 0.721 & -0.161 \\ -0.126 & -0.721 & -1.060 & 1.677 \\ -0.061 & -0.161 & -1.677 & -0.221 \end{bmatrix} x(t) \\ & + \begin{bmatrix} 76.47 \\ 240.4 \\ 242.7 \\ 83.37 \end{bmatrix} u(t) \\ y(t) = & \begin{bmatrix} 76.47 & -240.4 & 242.7 & -83.37 \end{bmatrix} x(t) \end{aligned} \quad (7.47)$$

Note that, while this nominal dynamics model will be used for controller design, the actual dynamics model of the nanopositioner would have unity gain at DC. This is a consequence of the way the hysteresis is modeled; the DC gain of the system is effectively incorporated into the hysteresis model. This was discussed in Remark 10. Indeed, the dynamics models used in previous chapters were scaled to unity gain for this reason. After identifying our modified PI operator, the minimum gain of the hysteresis operator was found to be 4.69, with a maximum of 13.36, while the gain of

the plant (7.47) is 5.62. Let the equation

$$\dot{x}_u(t) = A_u x_u(t) + B_u u(t) \quad (7.48)$$

$$y_u(t) = C_u x_u(t) \quad (7.49)$$

denote the canonical form of the dynamics (7.47) with unity gain, i.e. $y(t) = 5.62 y_u(t)$. We can then fit our nanopositioning system into the form considered in (7.3)-(7.5) by letting $m = 0$ and $p = 4$, where

$$A_0 + B\lambda = A_u, B = B_u, C = C_u \quad (7.50)$$

Based on the definitions of (7.50) and Remark 11, $\bar{\theta}_h$ for the modified PI operator considered takes values in the interval $[4.69/5.62, 13.36/5.62] = [0.83, 2.38]$. The boundaries of this interval form the values of $\min(\bar{\theta}_h)$ and $\max(\bar{\theta}_h)$.

Our experiments focused on tracking sinusoidal signals of the form

$$y_r(t) = 20 \sin(2\pi\omega t) + 30 \mu\text{m} \quad (7.51)$$

where $\omega = 5, 25, 50, 100, 200$. We utilized MHSC and SHSC designed for use both with and without hysteresis inversion. A Luenberger observer, based on the model in (7.47), was implemented to emulate state feedback. Because $u(t)$ is unavailable, the control signal $v(t)$ was used in this observer. The controller gains are chosen using the robust Riccati equation method (3.11), based on the nominal dynamics model (7.47), a method which was also used in [76]. Let $v(t) = [K_2, K_3, K_4]\gamma(t)$ denote the control synthesized by this method. We can then use the LMI toolbox of MATLAB to solve for the matrix P in (7.22), yielding $\Lambda = 4.44$. We also utilize Iterative

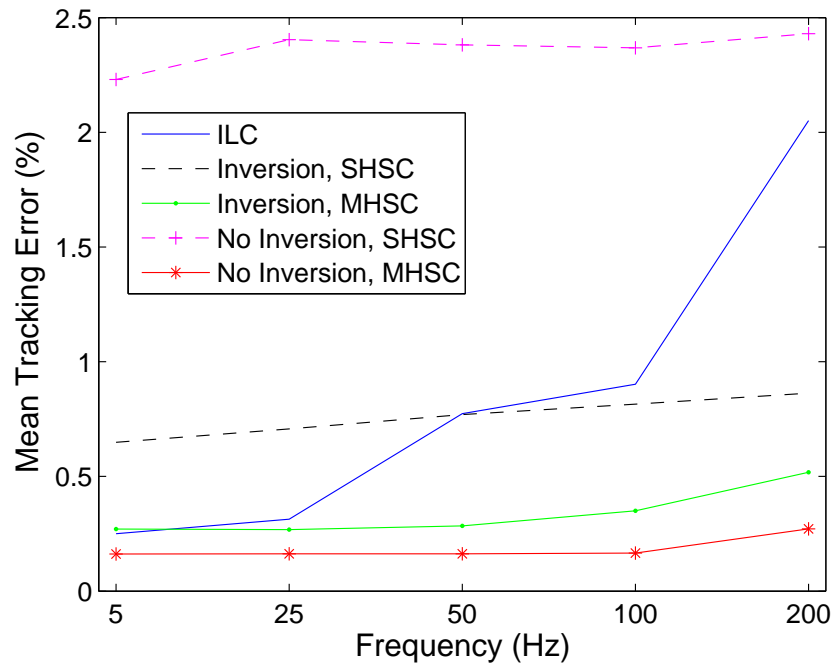


Figure 7.2: Mean tracking error for controllers used in experimental trials. SHSC refers to compensation of only the reference harmonic, and MHSC refers to compensation of the first, second, and third harmonics of the reference.

Learning Control [38] for comparison purposes in our tests.

Fig. 7.2 shows the resulting tracking error of the MHSC and SHSC with and without inversion, together with the Iterative Learning Control (ILC) results. One trend observed in all of the servocompensator-based controllers is that their performance is substantially more robust to increasing frequency than ILC. This is particularly true for the servocompensators that do not use inversion, which see very little variation in their performance until the reference reaches 200 Hz. We immediately note that the SHSC without inversion is the worst-performing controller; this is contrasted by the performance of the MHSC without inversion, which is the best-performing controller.

This seeming contradiction can be explained by looking into the frequency spectra of the error signals, provided in Fig. 7.3. We can see from this graph that the frequency components of

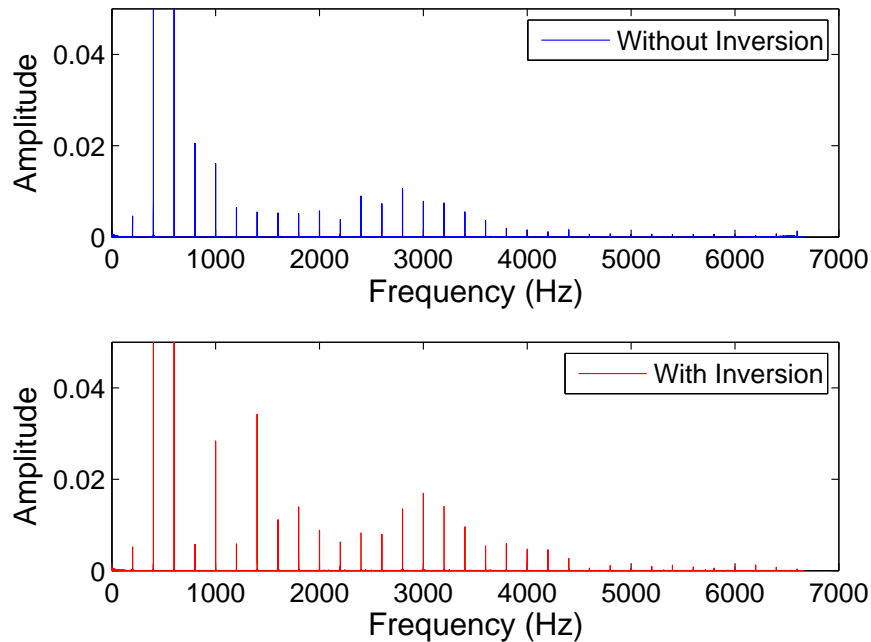


Figure 7.3: Frequency spectrum of the tracking error with SHSC with and without inversion. Bump near 3 kHz is caused by the resonance peak of the nanopositioner.

the tracking error above 600 Hz are larger when inversion is used as compared to when it is left out. The modified PI operator attempts to approximate the hysteresis with non-smooth play and deadzone operators. Therefore, we expect more high frequency components to be introduced into the system using inversion than when inversion is left out. The performance difference between the controllers is explained by the amplitude of the second and third harmonics, which are much larger without inversion than with inversion. However, once the MHSC is used, these harmonics are compensated and removed from the system, meaning that the overall tracking error is greatly reduced, especially when inversion is not used. In addition, the removal of the hysteresis inversion greatly reduces the computational requirements of the controller. For example, the MHSC without hysteresis inversion averaged a computation time of $28 \mu\text{s}$ per sampling period, while the MHSC with inversion required $45 \mu\text{s}$ of computation time. This is a significant savings, especially since the controller possesses half the mean tracking error when the inversion is removed.

Chapter 8

Properties of Self-Excited Limit Cycles in a System with Hysteresis

8.1 Introduction

For systems with hysteresis, most existing work aims to provide sufficient conditions under which a given controller structure guarantees stability of the system in question. A natural question therefore is to consider the behavior of the system when these conditions are not satisfied; alternatively, what effects do hysteresis nonlinearities have on the steady-state solutions of the system? For example, consider our LMI result presented in Chapter 7. A necessary condition for the existence of a matrix P solving either (7.21) or (7.22) is that each subsystem is Hurwitz, since (7.21) and (7.22) are in the form of Lyapunov equations. However, what would happen if one or more of these subsystems were unstable?

Several authors have remarked that hysteresis can lead to unwanted oscillations, perhaps most notably in the work of [33]. Further investigations into these oscillations are limited. One result is in [92], where conditions are presented under which the method of harmonic balance predicts the existence of periodic solutions in systems with relay hysteresis. The authors of [93] utilized the describing function method to predict the existence of a limit cycle in a Terfenol-D-based actuator, and demonstrated its existence in experiments. These works focused fundamentally on the question of existence, and did not investigate any properties of the limit cycles in detail. There is also some

additional work on limit cycles in systems with relay hysteresis [94], which was driven primarily by researchers in the field of electronic circuits in the 60's.

In this Chapter, we offer an in-depth exploration into the properties of self-excited limit cycles occurring in a particular class of systems with hysteresis. We first observe that using rejection-focused design techniques can lead to steady-state self-excited limit cycles in the system. We then investigate the properties of these limit cycles, focusing on a linear plant controlled by an integral controller, where a play operator [32] is present in the feedback loop. We focus our attention on odd symmetric limit cycles within the system. A Newton-Raphson algorithm is formulated to calculate the limit cycles, and using the odd symmetry of the operator, we are then able to prove that linear relationships exist between several properties of the limit cycles and the parameters of the system. These results are verified in simulation, where we also demonstrate the effectiveness of the Newton-Raphson algorithm at predicting the solutions of the system.

8.2 Motivating Example: Issues with Rejection-focused methods

Let us consider a scalar system preceded by a play operator and a unity gain controlled using integral control and feedback. This represents a basic cascade of a Prandtl-Ishlinskii hysteresis operator with dynamics. The system is written as,

$$\begin{aligned}
 \dot{x}(t) &= ax(t) + v(t) + \theta_h W_r[v; 0](t) \\
 \dot{\sigma}(t) &= x(t) \\
 v(t) &= -k_1 x(t) - k_2 \sigma(t)
 \end{aligned} \tag{8.1}$$

where r is the play radius and θ_h is a weighting term. For our simulations, we will let $K = [k_1, k_2] = [1, 1]$, and set $a = 1.5$ with $\theta_h = 1$. One technique used in rejection-focused control methods is to consider the hysteresis as a linear gain coupled with a bounded, time-varying uncertainty, as was done in [49]. For (8.1), this linear gain is equal to the coefficient of v added with the weight θ . Based on this idea, we reformulate the closed-loop system as

$$\begin{bmatrix} \dot{x}(t) \\ \dot{\sigma}(t) \end{bmatrix} = \begin{bmatrix} a - 2k_1 & -2k_2 \\ 1 & 0 \end{bmatrix} \begin{bmatrix} x(t) \\ \sigma(t) \end{bmatrix} + \begin{bmatrix} S_r[v; 0](t) \\ 0 \end{bmatrix} \quad (8.2)$$

where $S_r[v; 0](t)$ is a stop nonlinearity [28] which takes values in the bounded region $[-r, r]$. In particular, for monotone input v ,

$$S_r[v; 0](t) = \min\{r, \max\{-r, v(t) - v(0) + S_r[v; 0](0)\}\}$$

We can compute the eigenvalues of this system through the roots of the equation

$$\det(sI - A) = s^2 - (a - 2k_1)s + 2k_2 \quad (8.3)$$

where

$$A = \begin{bmatrix} a - 2k_1 & -2k_2 \\ 1 & 0 \end{bmatrix}$$

These eigenvalues have negative real parts for $k_1 > a/2$ and $k_2 > 0$, both of which are satisfied for our choice of K . Therefore the trajectories of the system remain bounded, since (8.2) is an exponentially stable linear system driven by a bounded input. However, when the play operator in

(8.1) is in the play region, the \dot{x} equation becomes

$$\dot{x}(t) = (a - k_1)x(t) - k_2\sigma(t) + k_r$$

where k_r is a constant value determined by the current state of the play operator. Using this, the eigenvalues of the closed-loop system obey

$$\det(sI - A) = s^2 - (a - k_1)s + k_2 \quad (8.4)$$

where

$$A = \begin{bmatrix} a - k_1 & -k_2 \\ 1 & 0 \end{bmatrix}$$

Since $a - k_1 = 0.5$, the system dynamics are unstable when the operator lies in the play region. Fig. 8.1 shows the behavior of (8.1) for varying play radii. We clearly see that the system enters a limit cycle for each value of the play radius. This occurs because the controller gains K are not chosen to account for the nonlinear behavior of the hysteresis. Furthermore, these limit cycles are self-excited, in that there is no external input driving the system. Clearly, such oscillations in the system are not ideal, even though the system state does remain bounded. However, the properties of these limit cycles are interesting in their own right.

8.3 Self-Excited Limit Cycles in a System with Hysteresis

We now investigate the properties of the limit cycles observed in Fig. 8.1. Consider a linear system preceded by a play operator and a unity gain controlled using integral control and state feedback

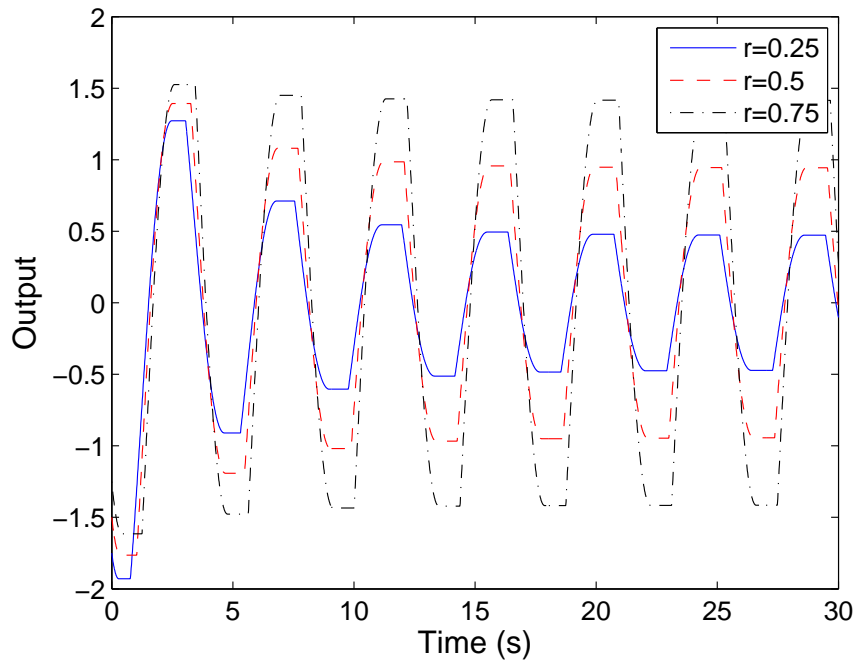


Figure 8.1: Hysteresis state for systems that are unstable when the hysteresis is in the play region, with varying play radii.

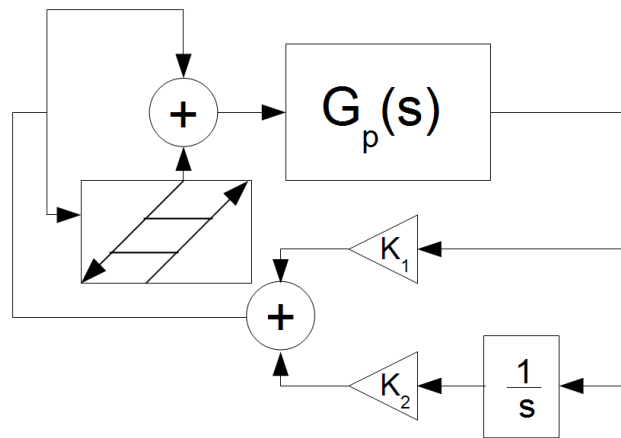


Figure 8.2: Closed-loop system described in (8.5).

as illustrated in Fig. 8.2;

$$\begin{aligned}
\dot{x}(t) &= Ax(t) + B(v(t) + W_r[v; 0](t)) \\
\dot{\sigma}(t) &= Cx(t) \\
v(t) &= -K_1x(t) - K_2\sigma(t)
\end{aligned} \tag{8.5}$$

where $x \in \mathfrak{R}^n$, $\sigma \in \mathfrak{R}$, $A \in \mathfrak{R}^{n \times n}$, $B \in \mathfrak{R}^n$, $C \in \mathfrak{R}^{1 \times n}$, $K_1 \in \mathfrak{R}^{1 \times n}$, and $K_2 \in \mathfrak{R}$. Notice from Fig. 2.1 and (2.1) that there are two basic modes in which the state of a play operator can reside. The first is the linear region, in which $u(t) = v(t) \pm r$. The second mode of operation is the play region, where $u(t)$ is constant, represented in (2.1) by the term $u(0)$. We will make use of the linear and play region terminology throughout this Chapter. Furthermore, we will also refer to the leftmost linear branch in Fig. 2.1 as the descending region, and the rightmost linear branch as the ascending region.

The well-posedness of (8.5) follows from the arguments in [41]. We now begin our analysis of (8.5) by providing a coordinate transform in order to place (8.5) into a switched system form, as in Chapter . Let us define

$$\alpha(t) = -K_2\sigma(t) + W_r[v; 0](t) \tag{8.6}$$

The derivative of α requires us to define the derivative of a play operator, which is in general discontinuous. Let Π denote the set of all closed intervals of $t \in \mathfrak{R}$ in which $W_r[v; 0](t)$ lies in a linear region, and let Π^c denote its complement. We therefore have a piecewise continuous

definition for \dot{W}_r , given by

$$\dot{W}_r[v;0](t) = \begin{cases} \dot{v}, & \text{if } t \in \Pi \\ 0, & \text{if } t \in \Pi^c \end{cases}$$

where

$$\begin{aligned} \dot{v}(t) &= -K_1[(A - BK_1)x(t) + B\alpha(t)] - K_2[Cx(t)] \\ &= [-K_1(A - BK_1) - K_2C]x(t) - K_1B\alpha(t) \end{aligned} \quad (8.7)$$

Note that this derivative is continuous everywhere except when the play operator exits the play region. Using (8.6)-(8.7), we can derive a switched system form for (8.5):

$$\begin{aligned} \dot{\gamma}(t) &= A_{i(t)}\gamma(t), \quad i = 1, 2 \quad (8.8) \\ A_1 &= \begin{bmatrix} A - BK_1 & B \\ -CK_2 & 0 \end{bmatrix}, \quad A_2 = \begin{bmatrix} A - BK_1 & B \\ -2CK_2 - K_1(A - BK_1) & -K_1B \end{bmatrix} \end{aligned}$$

where $\gamma = [x^T, \alpha]^T$, and r is the play radius. The matrix A_1 characterizes the systems behavior in the play region of the hysteresis, while A_2 does so for the linear region of the hysteresis. To describe the switching behavior of $i(t)$, we will define the operator

$$i(t) = \Omega[W_r[v;0](t)](t) \quad (8.9)$$

where $\Omega[W_r[v;0](t)] = 1$ when W_r is in the play region, and $\Omega[W_r[v;0](t)] = 2$ when W_r is in the linear region. From simulations of (8.8), we observe that if the control gains are chosen such that

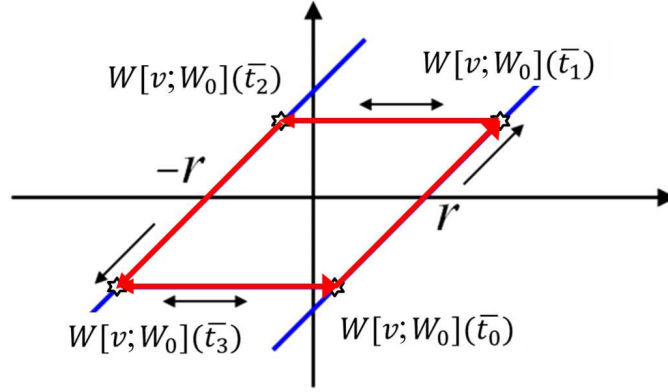


Figure 8.3: Illustration of the state of the play operator P_r during a sine-like limit cycle. The stars indicate times when the system dynamics switch.

A_1 is unstable and A_2 is Hurwitz, the trajectories of (8.8) converge to a limit cycle. Furthermore, the limit cycle we observe is sine-like, in that it is both odd-symmetric and changes the sign of its derivative twice a period. Based on these observations, we will develop a Newton-Raphson algorithm to calculate the sine-like solutions of the limit cycle.

8.3.1 Computation of the Limit Cycles

Our search for the solution of the limit cycles begins from a state γ_0 at \bar{t}_0 such that the play operator is in the ascending linear section. Let \bar{t}_1 denote the time when the play operator enters the play region from the linear region; this will be denoted as the first switching time. Similarly, we define \bar{t}_2, \bar{t}_3 , and \bar{t}_4 as the second, third and fourth switching times. Since the system starts in the linear region, $i(0) = 2$, $i(\bar{t}_1^+) = 1$, $i(\bar{t}_2^+) = 2$, and so on. Furthermore, based on our assumption of sine-like limit cycles, $\gamma(\bar{t}_4) = \gamma(0)$; therefore $\bar{t}_4 - \bar{t}_0$ is the period of the limit cycle. From the description of the play operator, for any sine-like limit cycle, the control $v(t)$ at these switching times obeys the

equations,

$$\dot{v}(\bar{t}_1) = 0 \quad (8.10)$$

$$v(\bar{t}_1) - v(\bar{t}_2) = 2r \quad (8.11)$$

$$\dot{v}(\bar{t}_3) = 0 \quad (8.12)$$

$$v(\bar{t}_3) - v(\bar{t}_4) = -2r \quad (8.13)$$

Furthermore, symmetry allows us to only consider the conditions (8.10) and (8.11). We will let $t_1 = \bar{t}_1 - \bar{t}_0$ and $t_2 = \bar{t}_2 - \bar{t}_1$; these values will be referred to as the switching *intervals*. We can then translate these equations into functions of γ_0 . From (8.10) and the definitions of v and A_2 , we can quickly arrive at

$$H_1(\gamma_0, t_1) \triangleq \bar{K} e^{A_2 t_1} \gamma_0 = 0 \quad (8.14)$$

where $\bar{K} = [-K_1(A - BK_1) - K_2C, -BK_1]$. Since W_r is constant in the play region, from (8.11) and (8.6) we can derive

$$H_2(\gamma_0, t_1, t_2) \triangleq [-K_1, 1][I - e^{A_1 t_2}]e^{A_2 t_1} \gamma_0 = 2r \quad (8.15)$$

where I is an appropriately dimensioned identity matrix. Finally, because we are seeking sine-like limit cycles, we also have the constraint equation

$$\Sigma^T(\gamma_0, t_1, t_2) \triangleq (I + e^{A_1 t_2} e^{A_2 t_1}) \gamma_0 = 0 \quad (8.16)$$

which is derived from the forward-time solution of the switched system from $t = \bar{t}_0$ to $t = \bar{t}_2$. We now present the following lemma, which addresses the symmetry of the dynamics of the system.

Lemma 3 *Let γ_0 be the state of (8.8) when the system enters the ascending branch from the play region, and let $\gamma(\bar{t}_2)$ denote the state of (8.8) when it enters the descending linear region. Assume that the system switches once between states γ_0 and $\gamma(\bar{t}_2)$. Then, if the system lies at $-\gamma_0$ at $t = \bar{t}_0$ in the descending region, the state of the system when the system enters the ascending region is $-\gamma(\bar{t}_2)$.*

Proof. Based on equations (8.10) and (8.11), we know that γ_0 and $\gamma(\bar{t}_2)$ must obey

$$\begin{aligned}\gamma(\bar{t}_1) &= e^{A_2 t_1} \gamma_0, \quad \gamma(\bar{t}_2) = e^{A_1 t_2} \gamma(\bar{t}_1) \\ 0 &= \bar{K} e^{A_2 t_1} \gamma_0\end{aligned}\tag{8.17}$$

$$2r = [-K_1, 1][I - e^{A_1 t_2}] \gamma(\bar{t}_1)\tag{8.18}$$

where t_1 and t_2 are the switching intervals. Now consider the behavior starting from $-\gamma(0)$. Then,

$$\begin{aligned}\gamma(\bar{t}_1^*) &= -e^{A_2 t_1^*} \gamma_0, \quad \gamma(\bar{t}_2^*) = e^{A_1 t_2^*} \gamma(\bar{t}_1^*) \\ 0 &= -\bar{K} e^{A_2 t_1^*} \gamma_0\end{aligned}\tag{8.19}$$

$$-2r = [-K_1, 1][I - e^{A_1 t_2^*}] \gamma(\bar{t}_1^*)\tag{8.20}$$

where \bar{t}_1^* and \bar{t}_2^* are the switching times and t_1^* and t_2^* are the switching intervals for the system when it is initialized at $-\gamma_0$. Note the minus sign on the $2r$ term in (8.20). This is because we are entering the opposite region of the play operator from the original case, and therefore this switching condition would be derived from (8.13) instead of (8.11). Comparing (8.17) with (8.19),

we notice that the sole difference is the presence of the negative sign, which cannot affect whether $\dot{v} = 0$. Therefore, t_1^* is equal to t_1 , implying $\gamma(\bar{t}_1^*) = -\gamma(\bar{t}_1)$. Using this in (8.20) yields

$$[-K_1, 1][I - e^{A_1 t_2^*}] \gamma(\bar{t}_1^*) = -2r$$

$$[-K_1, 1][I - e^{A_1 t_2^*}] \gamma(\bar{t}_1) = 2r$$

Since we have recovered (8.18), we know that $t_2^* = t_2$, which completes the proof. \square

Remark 13 *This lemma shows that as long as a γ_0 can be found such that $\gamma_0 = -\gamma(\bar{t}_2)$, the system possesses a sine-like limit cycle. However, this result is proved under the assumption that the sign of \dot{v} does not change in the interval $[\bar{t}_1, \bar{t}_2]$, which implies there is only one switching between \bar{t}_0 and \bar{t}_2 . Proving that this does indeed occur is part of our ongoing future work.*

Equations (8.14)-(8.16) yield $n + 3$ equations with $n + 3$ unknowns, $\gamma_0 = [x_0^T, \alpha_0]^T$, t_1 , and t_2 . We will refer to solving this set of simultaneous equations as the *limit cycle problem*. Due to the nonlinearity of these equations, we will utilize the well-known Newton-Raphson method to find a solution to the limit cycle problem. Denote our unknowns as $\Phi = [\gamma_0^T, t_1, t_2]^T$. We can then define

$$\mathcal{P}(\Phi) = [\Sigma^T(\Phi), H_1(\Phi), H_2(\Phi)]^T \quad (8.21)$$

We can now apply the Newton-Raphson method to obtain a solution to the above equation using the iterative formula

$$\Phi^{i+1} = \Phi^i + J^{-1}(\Phi^i) \mathcal{P}(\Phi^i) \quad (8.22)$$

where

$$J(\Phi) = \begin{bmatrix} \frac{\partial \Sigma}{\partial \gamma_0} & \frac{\partial \Sigma}{\partial t_1} & \frac{\partial \Sigma}{\partial t_2} \\ \frac{\partial H_1}{\partial \gamma_0} & \frac{\partial H_1}{\partial t_1} & \frac{\partial H_1}{\partial t_2} \\ \frac{\partial H_2}{\partial \gamma_0} & \frac{\partial H_2}{\partial t_1} & \frac{\partial H_2}{\partial t_2} \end{bmatrix} \quad (8.23)$$

These partial derivatives can be readily calculated in closed-form based on (8.14)-(8.16). Note that the only dependence on γ_0 within these equations is the linear term. We can then take the partial derivatives one element at a time. For example, let γ_{0i} denote the i th element of γ_0 . Then,

$$\frac{\partial \Sigma}{\partial \gamma_{0i}} = (I + e^{A_1 t_2} e^{A_2 t_1}) [0^{1 \times (i-1)}, 1, 0^{1 \times (n+1-i)}]' \quad (8.24)$$

where i can range from 1 to $n + 1$. Therefore,

$$\frac{\partial H_1}{\partial \gamma_{0i}} = \bar{K} e^{A_2 t_1} [0^{1 \times (i-1)}, 1, 0^{1 \times (n+1-i)}]' = 0 \quad (8.25)$$

$$\frac{\partial H_2}{\partial \gamma_{0i}} = [-K_1, 1] [I - e^{A_1 t_2}] e^{A_2 t_1} [0^{1 \times (i-1)}, 1, 0^{1 \times (n+1-i)}]' = 2r \quad (8.26)$$

To compute the partial derivatives with respect to the switching times t_1 and t_2 , we make use of the formula,

$$\frac{de^{At}}{dt} = Ae^{At} = e^{At}A$$

The remaining partial derivatives in J can then be calculated as

$$\begin{aligned}\frac{\partial \Sigma}{\partial t_1} &= (I + e^{A_1 t_2} e^{A_2 t_1} A_2) \gamma_0 \\ \frac{\partial \Sigma}{\partial t_2} &= (I + A_1 e^{A_1 t_2} e^{A_2 t_1}) \gamma_0 \\ \frac{\partial H_1}{\partial t_1} &= \bar{K} A_2 e^{A_2 t_1} \gamma_0 \\ \frac{\partial H_1}{\partial t_2} &= 0 \\ \frac{\partial H_2}{\partial t_1} &= [-K_1, 1][I - e^{A_1 t_2}] e^{A_2 t_1} A_2 \gamma_0 \\ \frac{\partial H_2}{\partial t_2} &= [-K_1, 1][I - A_1 e^{A_1 t_2}] e^{A_2 t_1} \gamma_0\end{aligned}$$

The limit cycle is then characterized by the solution of the equation,

$$\mathcal{P}(\Phi^*) = 0 \tag{8.27}$$

Note that Φ^* completely characterizes the behavior of the limit cycles, as once the switching times and initial conditions are known, the closed-form solution of the limit cycle can be computed from successive solutions of the two (switching) linear systems.

8.3.2 Properties of the Limit Cycles

While the solution of the limit cycle problem Φ^* must be calculated numerically, we can utilize the equations (8.14)-(8.16) to prove some properties of the limit cycles corresponding to the solution Φ^* . First, we will see how the solution Φ^* varies with the play radius r .

Proposition 1 *Let the solution of the limit cycle problem with $r = r^*$ be denoted by $\Phi_{r^*} = [\gamma_0^{*T}, t_1^*, t_2^*]^T$.*

Then, if $r = r^ c_1$, where $c_1 > 0$, $\Phi_r = [c_1 \gamma_0^{*T}, t_1^*, t_2^*]^T$ is a solution to the limit cycle problem.*

Proof. We begin by directly computing (8.15) evaluated at $\Phi_r = [c_1 \gamma_0^{*T}, t_1^*, t_2^*]^T$ with $r = r^* c_1$, which can be written as

$$[-K_1, 1][I - e^{A_1 t_2^*}]e^{A_2 t_1^*} c_1 \gamma_0^* = 2r^* c_1 \quad (8.28)$$

By dividing both sides by c_1 , we arrive at the solution of $H_2(\Phi_{r^*})$. Since the left-hand sides of (8.14) and (8.16) are linear with respect to the initial state, the c_1 term can be immediately divided out, proving $[c_1 \gamma_0^{*T}, t_1^*, t_2^*]^T$ solves the limit cycle problem. \square

Proposition 1 shows that there is a linear relationship between the play radius r and the amplitude of the limit cycles generated in (8.8)-(8.9). Next, we can show that the bias of the limit cycles can be set to non-zero values. Consider the system

$$\begin{aligned} \dot{x}(t) &= Ax(t) + B(v(t) + W_r[v; 0](t)) \\ \dot{\sigma}(t) &= Cx(t) - y_r \\ v(t) &= -K_1 x(t) - K_2 \sigma(t) \end{aligned} \quad (8.29)$$

where y_r is a constant reference. The only difference between the above equation and our original system is the presence of the term y_r . Let us assume that

$$\text{rank} \left(\begin{bmatrix} A & B \\ C & 0 \end{bmatrix} \right) = n + 1$$

This is a well known necessary and sufficient condition for the existence of a steady-state solution to systems with constant references when integral control is used. Let $\bar{x} \in \mathfrak{R}^n$ and $\bar{\sigma} \in \mathfrak{R}$ be such

that

$$0 = (A - BK_1)\bar{x} - BK_2\bar{\sigma}, \quad 0 = C\bar{x} - y_r \quad (8.30)$$

Defining $\bar{v} = -K_1\bar{x} - K_2\bar{\sigma}$, we can see that (8.30) reduces to

$$\begin{bmatrix} A & B \\ C & 0 \end{bmatrix} \begin{bmatrix} \bar{x} \\ \bar{v} \end{bmatrix} = \begin{bmatrix} 0 \\ y_r \end{bmatrix}$$

Therefore, our assumption guarantees the existence and uniqueness of \bar{x} and $\bar{\sigma}$. Next, define the coordinates

$$\tilde{x} = x - \bar{x}, \quad \tilde{\sigma} = \sigma - \bar{\sigma} \quad (8.31)$$

Note that since y_r , \bar{x} and $\bar{\sigma}$ are constants, the closed-loop system can be written as (using (8.30)),

$$\begin{aligned} \dot{\tilde{x}}(t) &= (A - BK_1)\tilde{x}(t) + B(-K_2\tilde{\sigma}(t) + W_r[v; 0](t)) \\ \dot{\tilde{\sigma}}(t) &= C\tilde{x} \end{aligned} \quad (8.32)$$

This is the same form as that considered in (8.5). Therefore, the system (8.29) and (8.9) possesses the same limit cycle as (8.8)-(8.9), with the exception of a constant shift in the coordinates α and x . We present this result as the following proposition.

Proposition 2 *Let $\Phi_0 = [\gamma_0^T, t_1, t_2]^T$ denote the solution of the limit cycle problem for (8.8)-(8.9). Then, $\Phi^* = [(x_0 + \bar{x})^T, \alpha_0 - K_2\bar{\sigma}, t_1^*, t_2^*]^T$ is a solution to the limit cycle problem for the system (8.29) and (8.9).*

Finally, we consider a special case of the system (8.5), where we assume x to be a scalar and whose derivative obeys

$$\dot{x}(t) = ax(t) + (v(t) + W_r[v;0](t))$$

We then select the control to be $v(t) = [k_p a, a^2/2]\gamma(t)$, where $k_p \in (0.5, 1)$. The eigenvalues of the systems then linearly scale with increasing a . The system matrices are then

$$\dot{\gamma}(t) = A_{i(t)}\gamma(t), \quad i = 1, 2 \quad (8.33)$$

where

$$A_1 = \begin{bmatrix} (1 - k_p)a & 1 \\ -a^2/2 & 0 \end{bmatrix}, \quad A_2 = \begin{bmatrix} (1 - k_p)a & 1 \\ -a^2 - k_p(1 - k_p)a^2 & -k_p a \end{bmatrix}$$

We can now show that the frequency of the limit cycles is linearly related to the parameter a . Let us focus on the system in the linear region of operation, i.e., $\dot{\gamma}(t) = A_2\gamma(t)$. The characteristic equation of this system is

$$s^2 - \text{Tr}(A_2)s + \text{Det}(A_2) = 0 \quad (8.34)$$

with

$$\text{Tr}(A_2) = (1 - 2k_p)a, \quad \text{Det}(A_2) = a^2$$

where Tr and Det denote the trace and determinant respectively. Let us consider the state x as the output of this second-order system, and formulate a canonical form transformation. Let $\chi_1 = x$ and

$\chi_2 = \dot{x}$. This transforms the system equations based on A_2 with our specified control gains into

$$\dot{\chi}_1(t) = \chi_2(t) \quad (8.35)$$

$$\dot{\chi}_2(t) = -a^2\chi_1(t) + (1 - 2k_p)a\chi_2(t) \quad (8.36)$$

Next, let $\eta_1 = a\chi_1$, and let $\eta_2 = \chi_2$. The $\dot{\eta}$ equations are then

$$\dot{\eta}_1(t) = a\eta_2(t) \quad (8.37)$$

$$\dot{\eta}_2(t) = -a\eta_1(t) + (1 - 2k_p)a\eta_2(t) \quad (8.38)$$

Finally, let the time variable $t = a\tau$, which implies that

$$\frac{d}{d\tau} = \frac{1}{a} \frac{d}{dt}$$

Equation (8.37) now becomes

$$\frac{d\eta_1}{d\tau}(\tau) = \eta_2(\tau) \quad (8.39)$$

$$\frac{d\eta_2}{d\tau}(\tau) = -\eta_1(\tau) + (1 - 2k_p)\eta_2(\tau) \quad (8.40)$$

which is independent of a . The same transform can be applied to the system governed by the A_1 matrix, which then also becomes independent of a . The resulting system equations in these

transformed coordinates are

$$\dot{\eta}(\tau) = A_{\eta_i}\eta(\tau), i = 1, 2$$

$$A_{\eta_1} = \begin{bmatrix} 0 & 1 \\ -1/2 & (1 - k_p) \end{bmatrix}, A_{\eta_2} = \begin{bmatrix} 0 & 1 \\ -1 & (1 - 2k_p) \end{bmatrix} \quad (8.41)$$

We can then apply equations (8.14)-(8.16) to (8.41), whose solution will be independent of a . By reversing the coordinate transforms on resulting solution, we see that the effect of increasing a is to scale down the amplitude and scale up the frequency of the resulting oscillations. Equivalently, the switching intervals t_1 and t_2 are scaled by $1/a$. This result allows us to present the following proposition.

Proposition 3 *Consider the system (8.33). Let the solution of the limit cycle problem with $a = a^*$ be denoted by $[\gamma_0^{*T}, t_1^*, t_2^*]^T$. Then, if $a = a^*c_1$, where $c_1 > 0$, $1/c_1[\gamma_0^{*T}, t_1^*, t_2^*]^T$ is a solution to the limit-cycle problem.*

8.3.3 Stability of Self-Excited Limit Cycles

We will now investigate the stability of the resulting limit cycles. Note that the solution of (8.8) evolving according to Φ^* obeys the Poincare mapping,

$$\gamma_0^* = \Psi(\gamma_0^*) \triangleq e^{A_1 t_2^*} e^{A_2 t_1^*} e^{A_1 t_2^*} e^{A_2 t_1^*} \gamma_0^* \quad (8.42)$$

The (local) stability of this mapping is determined by linearizing the mapping about the fixed point γ_0^* ; if the eigenvalues have magnitude less than 1, then the solution is locally stable [95]. Note that t_1^* and t_2^* are in fact dependent on the state γ_0^* ; therefore in linearizing the system, the dependence

of the switching times on the state γ must be considered. To do this, we define the mappings

$$\Psi_1(\gamma) = e^{A_2 t_1} \gamma, \quad \Psi_2(\gamma) = e^{A_1 t_2} \gamma$$

We also define

$$\kappa = [-K_1, 1][I - e^{A_1 t_2}]$$

It can then be shown using [95] that the differential of these maps can be computed as,

$$d\Psi_1(\gamma) = \left(I - \frac{A_2 \gamma \bar{K}^T}{(\bar{K}^T A_2 \gamma)} \right) e^{A_2 t_1} \quad (8.43)$$

$$d\Psi_2(\gamma) = \left(I - \frac{A_1 \gamma \kappa^T}{\kappa^T A_1 \gamma} \right) e^{A_1 t_2} \quad (8.44)$$

We can then calculate the differential of the Poincare map as

$$d\Psi(\gamma^*) = [d\Psi_2(\gamma^*(\bar{t}_1)) d\Psi_1(\gamma_0^*)]^2 \quad (8.45)$$

where $\gamma^*(\bar{t}_1) = e^{A_2 t_1} \gamma_0^*$. Note that though these mappings are dependent on Φ^* ; however, we have suppressed this dependence in our notation for clarity in the definition of the differential. Since, for any square matrix A with eigenvalues λ , the eigenvalues of A^2 are equal to λ^2 , we need only compute the eigenvalues of the matrix $d\Psi_2(\gamma^*(\bar{t}_1)) d\Psi_1(\gamma_0^*)$. This is the limit of our analytical results, as we do not possess an analytical form for γ_0^* . However, this condition can be quickly verified for any system using the numerical results of Section 8.3.1.

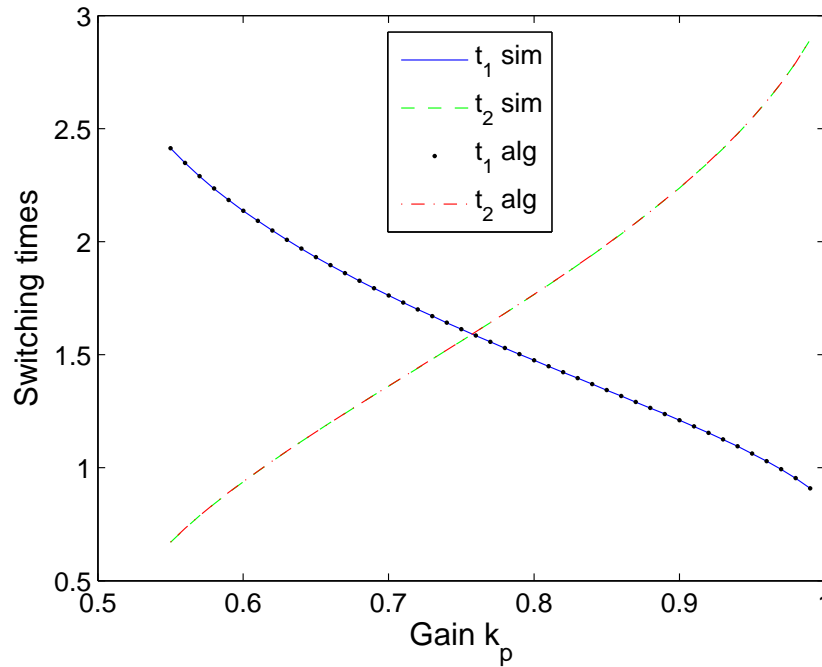


Figure 8.4: Switching times computed from algorithm and simulation, versus gain k_p .

8.4 Simulation Results

We now continue our examination of the limit cycles through simulation. These simulations are performed on a system obeying (8.33), where $a = 1$, and $r = 0.5$. First, we explore the variation of the solution to the limit cycle problem Φ^* with respect to the controller gain k_p . The effect of the gain k_p on the limit cycle solution is difficult to determine analytically; we instead explore its effect in simulation. Simultaneously, we verify the capability of the proposed Newton-Raphson method in computing the limit cycles by comparing its results to those observed in simulation.

Fig. 8.4 shows the switching times of the limit cycle as computed by both the Newton-Raphson algorithm and directly from simulation of the dynamics. The range of k_p considered was 0.55 to 0.99. There are several features of note on this figure. First, we are able to confirm the algorithm's effectiveness at computing the solution to the limit cycle with a scalar plant, as the simulation results agree very closely with the algorithm results. Second, looking at Fig. 8.4, we see that as

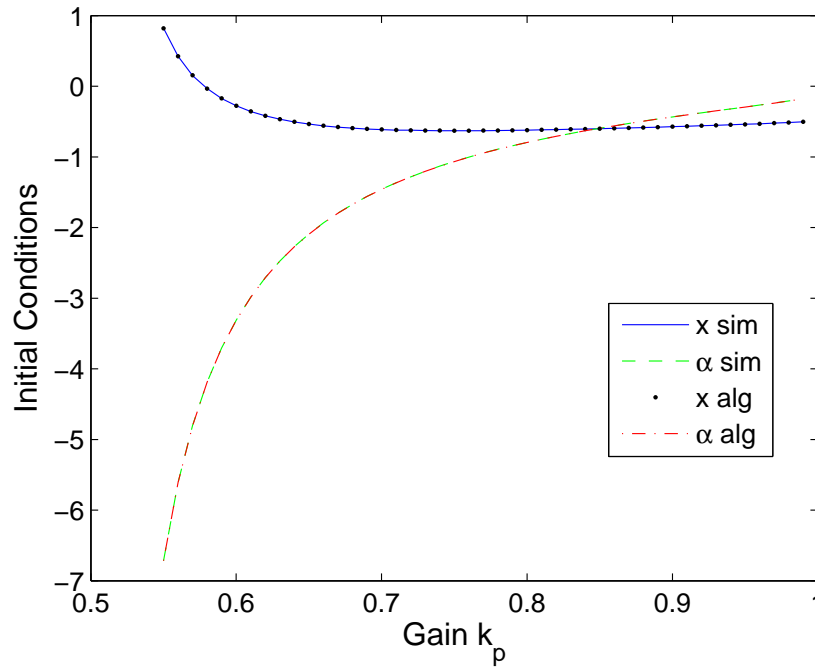


Figure 8.5: Limit cycle solutions computed from algorithm and simulation, versus gain k_p .

k_p approaches 1, the system spends more and more time in the play region (denoted t_2) versus the linear region (denoted t_1). This is because the eigenvalues in the linear region are significantly faster than those in the play region when k_p is high, meaning the system must spend more time in the play region to keep the system in steady state. Accordingly, smaller values of k_p results in the system spending more time in the linear region than the play region.

Fig. 8.5 shows the variation of the limit cycle solutions with k_p . Again, we see that the simulation and algorithm calculations are in tight agreement. Fig. 8.5 also indicates that as k_p approaches 0.5, the limit cycle solutions rapidly grow in size. This signals a rapid growth in the amplitude of the limit cycles for k_p , with the system becoming unstable for $k_p > 0.5$. Furthermore, Fig. 8.6 shows that the amplitude of the oscillations is strongly correlated with the size of α_0 .

Propositions 1-3 show that the bias, amplitude, and frequency of the limit cycles generated in the closed-loop system are related to the parameters of the system or, in the case of the bias,

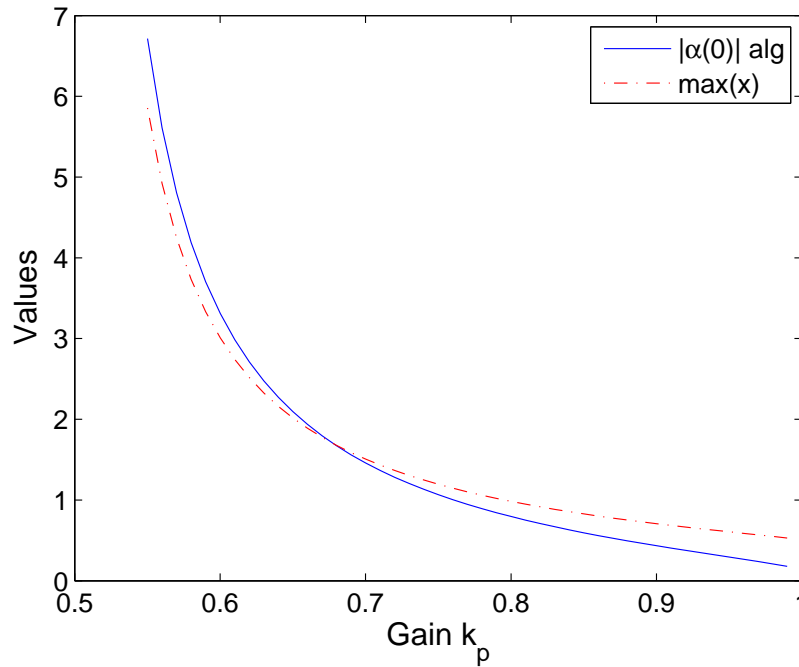


Figure 8.6: Peak amplitude of limit cycles versus absolute value of the limit cycle solutions α_0 .

to an external input. Our next set of simulations verify our ability to tune the properties of these oscillations, in particular, the frequency and amplitude of these limit cycles. We will demonstrate this property by running our system with two different sets of parameters, and then scaling or shifting one of the resulting solutions so that it equals the other. The oscillator (8.8) is first run with $W_0 = \sigma(0) = 0$, $x(0) = 1$, $a = 5$, $k_p = 0.75$, and $r = 0.5$. This solution is used as a base to construct the limit cycles obtained from different parameter sets. In particular, we look at tuning the amplitude of the oscillations by changing the play radius r . The play radius was increased to $r = 1$, and the simulation was rerun yielding what we call the true solution. We then multiplied the base solution by the ratio of the two radii, which is 2, to construct the scaled solution.

Figs. 8.7 and 8.8 compare the true and scaled solutions. From Fig. 8.7, we see a slight phase shift between the oscillations, which is caused by differences in the transient behaviors of the systems. This phase difference can be computed with Fourier analysis, which can then be used to

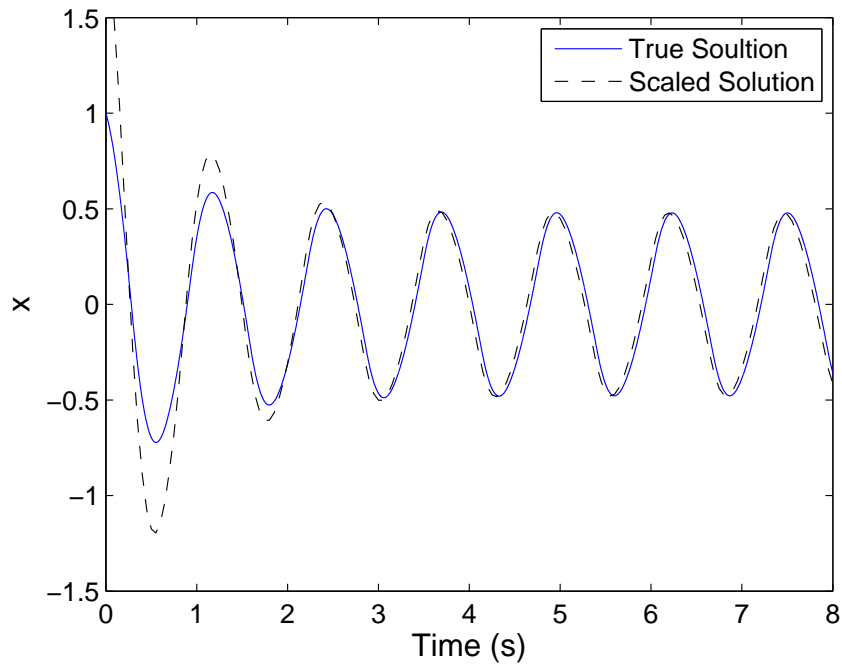


Figure 8.7: True solution and Scaled solution for $r = 1$. Note the phase difference created by the different transient behavior.

compute the appropriate time offset to move the signals into phase, as was done in Fig. 8.8. This figure confirms our theoretical expectations, with the oscillations matching up exactly.

We then explore tuning the oscillations through manipulation of the parameter a . The same solution was used for the base as in the Figs. 8.7 and 8.8, and the true solution was generated from (8.8) with $a = 10$. Fig. 8.9 shows the comparison between the true and scaled solutions at the steady state, once the phase offset is correctly included. Again, we see the agreement between the two solutions.

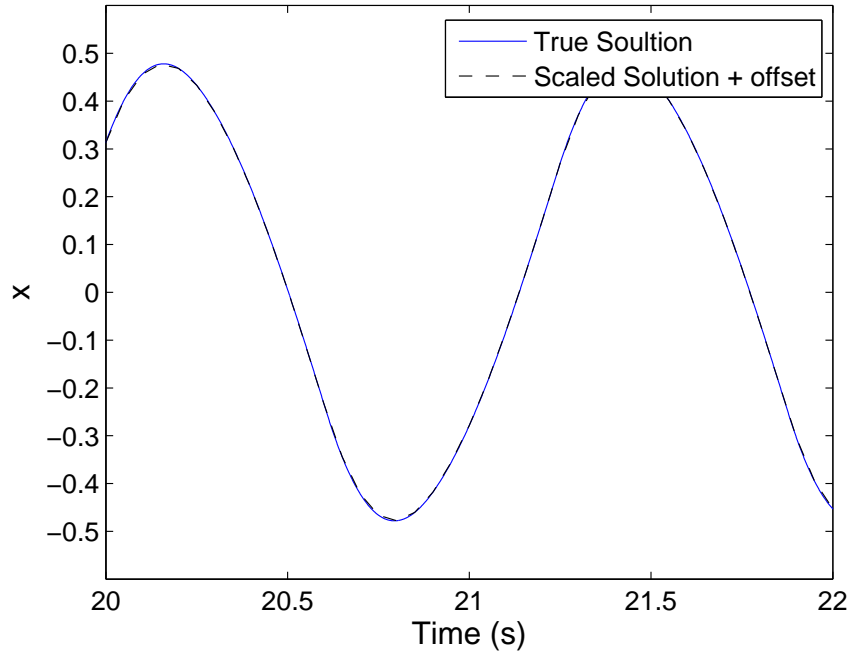


Figure 8.8: True solution and Scaled solution for $r = 1$ at steady state, with phase offset included.

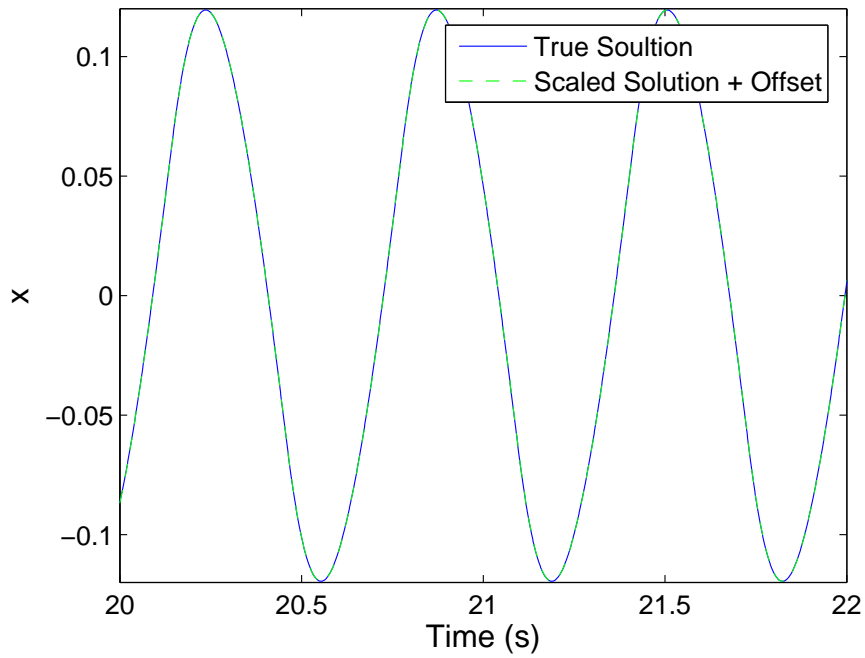


Figure 8.9: True solution and Scaled solution for $a = 10$ at steady state, with phase offset included.

Chapter 9

Conclusions and Future Work

9.1 Conclusions

Systems with hysteresis have been explored for over a century, but have recently garnered tremendous attention due to developments in smart materials. Motivated by the performance demands of technologies such as Scanning Probe Microscopy, we have explored the application of servocompensators to systems with hysteresis. Such controllers bridge the conceptual gap observed in the literature between rejection-focused controllers and inversion-focused controllers.

We first discussed the design of robust servocompensators, and proposed their use in a system modeled by a cascade of a modified PI operator and uncertain linear dynamics. By utilizing hysteresis inversion together with the robust servocompensator, we were able to prove the asymptotic stability and periodicity of the closed-loop system at steady state. The periodicity of the solution then allowed us to prove that a multi-harmonic servocompensator could directly attenuate the effect of hysteresis at steady state. These results were then confirmed through experiments conducted on a commercial nanopositioner, where we observed that the multi-harmonic servocompensator could significantly outperform existing methods in nanopositioning control, such as Iterative Learning Control and Proportional-Integral control.

Next, we performed harmonic analysis on hysteresis operators. In particular, we showed that the output of PKP and play operators can be formulated as a Fourier series, and presented sample calculations for sinusoidal and sawtooth signals. For play operators, we demonstrated that the

coefficients of the Fourier series are polynomial functions of the radius of the play operator and amplitude of the input.

After confirming the potential of the multi-harmonic servocompensator for controlling systems with hysteresis, we then began to address shortcomings in the approach. The first shortcoming we addressed was the requirement that the frequency of the reference trajectory was required *a priori* for the design of the servocompensator. A frequency-estimation based adaptive servocompensator, which we referred to as an indirect adaptive servocompensator, was proposed to solve this problem. We began by demonstrating the failings of existing adaptive servocompensator designs for our problem. As an alternative, we then presented a slow-adaptation based adaptive law coupled with a frequency-domain stabilizing controller. The stability of this controller was then proved using the theory of two-time-scale adaptation. Several combinations of reference trajectories and disturbances were considered, including some not directly applicable to nanopositioning applications. We then confirmed the stability and effectiveness of the indirect adaptive servocompensator through simulations and experiments, including showing some interesting properties regarding the behavior of the adaptation law.

We next addressed the requirement that hysteresis inversion be included in the controller to prove the stability of the closed-loop system. We saw that if an integral action was present in the controller, a coordinate transform could be defined in order to place the system into a switched system form, where the switching is governed by the states of the hysteresis operator. A common Lyapunov approach was then taken which, together with an LMI condition, allowed us to prove the stability and tracking error convergence of the closed-loop system when constant references were considered. These results allowed us to prove the boundedness of the system when a servocompensator was used to control the system. By removing the requirement of hysteresis inversion, we were able to experimentally demonstrate that the multi-harmonic servocompensator without using

hysteresis inversion can produce half the tracking error as the multi-harmonic servocompensator when inversion is used.

Motivated by observations made during our research into the LMI condition, we then investigated circumstances where a system with hysteresis could stabilize to a self-excited limit cycle. In particular, we explored the properties of self-excited limit cycles in an integral-controlled system with backlash. We proposed a Newton-Raphson algorithm capable of calculating the solutions of the limit cycles. We also demonstrated that the amplitude, frequency, and bias of the limit cycles possess linear relationships with parameters in the system.

9.2 Future Work

There remain several open problems for future work. Our LMI result proved the stability of our system with hysteresis when controlled by a servocompensator; however, periodicity of the solutions cannot be proven. In Chapter 7, we assumed the periodicity of solutions in order to demonstrate the effectiveness of the servocompensator, and justified this assumption based on experimental results observed in the literature together with our earlier results in Chapter 3. Proving that this assumption does indeed hold would represent a strong contribution to the field of systems with hysteresis.

A second contribution would involve devising a method of selecting the control gains in order to satisfy the LMI conditions presented in Chapter 7. Our current results serve as an analysis tool, where we can verify the stability of a system with hysteresis. However, there are no currently available methods to select the control gains in order to guarantee that the LMIs are satisfied. In addition, the current LMI framework cannot incorporate state observers, and instead must rely on state feedback.

We also note that in this work, we have used a finite-dimensional, classical or modified PI operator to model the hysteresis, and have assumed that the model uncertainties are limited to the weights of the operator. Conceivably, there will be a mismatch between the hysteresis nonlinearity in a physical system and what can be modeled with a classical/modified PI operator. While this type of modeling error can be reduced by increasing the numbers of play (and deadzone) elements in the PI model along with using sound practices in parameter identification, it is of interest to understand the impact of such modeling error. In particular, one could consider a small, unknown, hysteresis operator $\delta[v]$ that represents the difference between the actual hysteresis and the identified PI operator. Since the operator $\delta[\cdot]$ and the rest of the closed-loop system form feedback connections, one interesting approach to potentially analyzing such systems would be to generalize the small gain theorem [64] to the hysteretic setting.

There are also a number of smaller contributions that could be made to extend the work of this dissertation. Preliminary simulations seem to indicate that it is possible to extend the stability results for the n frequency case of the indirect adaptive servocompensator to include stability in the large. In addition, alternative stabilizing controllers could be designed to improve the performance of the multi-harmonic indirect adaptive servocompensator at high frequencies. An analytical proof for the existence of limit cycles of the system considered here would be a strong contribution. We briefly discussed in Remark 13 how such a proof could be conducted. It is also of interest to gain understanding on whether (8.27) admits a unique solution, as our computational examples have suggested.

BIBLIOGRAPHY

BIBLIOGRAPHY

- [1] J. Muir, "On the recovery of iron from overstrain," *Philosophical Transactions of the Royal Society of London Series A*, vol. 193, pp. 1–46, 1900.
- [2] S. Devasia, E. Eleftheriou, and S. O. R. Moheimani, "A survey of control issues in nanopositioning," *IEEE Transactions on Control Systems Technology*, vol. 15, pp. 802–823, 2007.
- [3] F. Gibson Baily, "The Hysteresis of Iron and Steel in a Rotating Magnetic Field," *Philosophical Transactions of the Royal Society of London Series A*, vol. 187, pp. 715–746, 1896.
- [4] F. Preisach, "über die magnetische nachwirkung," *Zeitschrift für Physik*, vol. 94, pp. 277–302, 1935.
- [5] L. Prandtl, "Ein gedankenmodell zur kinetischen theorie der festen krper," *ZAMM - Journal of Applied Mathematics and Mechanics / Zeitschrift fr Angewandte Mathematik und Mechanik*, vol. 8, no. 2, pp. 85–106, 1928. [Online]. Available: <http://dx.doi.org/10.1002/zamm.19280080202>
- [6] M. A. Krasnoselskii and A. V. Pokrovskii, "Periodic oscillations in systems with relay nonlinearities," *Akademiia Nauk SSSR, Doklady*, vol. 216, pp. 733–736, 1974.
- [7] M. Krasnoselskii and A. Pokrovskii, *Systems with Hysteresis*. Berlin-Heidelberg-New York-Paris-Tokyo: Springer Verlag, 1989.
- [8] R. C. Smith, *Smart Material Systems*. Philadelphia, PA: Society for Industrial and Applied Mathematics, 2005. [Online]. Available: <http://link.aip.org/link/doi/10.1137/1.9780898717471>
- [9] C. J and C. P, "Piezoelectric and allied phenomena in rochelle salt," *Comput Rend Acad Sci*, vol. 91, pp. 294–297, 1880.
- [10] W. J. Buehler and F. E. Wang, "A summary of recent research on the nitinol alloys and their potential application in ocean engineering," *Ocean Engineering*, vol. 1, no. 1, pp. 105 – 120, 1968. [Online]. Available: <http://www.sciencedirect.com/science/article/pii/002980186890019X>

- [11] Z. Chen, X. Tan, and M. Shahinpoor, "Quasi-static positioning of ionic polymer-metal composite (IPMC) actuators," in *Proceedings of the 2005 IEEE/ASME International Conference on Advanced Intelligent Mechatronics*, 2005, pp. 60 – 65.
- [12] X. Tan and J. S. Baras, "Modeling and control of hysteresis in magnetostrictive actuators," *Automatica*, vol. 40, no. 9, pp. 1469–1480, 2004.
- [13] N. Kwok, Q. Ha, T. Nguyen, J. Li, and B. Samali, "A novel hysteretic model for magnetorheological fluid dampers and parameter identification using particle swarm optimization," *Sensors and Actuators A: Physical*, vol. 132, no. 2, pp. 441 – 451, 2006. [Online]. Available: <http://www.sciencedirect.com/science/article/pii/S0924424706002019>
- [14] H. S. Majumdar, A. Bandyopadhyay, A. Bolognesi, and A. J. Pal, "Memory device applications of a conjugated polymer: Role of space charges," *Journal of Applied Physics*, vol. 91, no. 4, pp. 2433 –2437, 2002.
- [15] *World Piezoelectric Device Market*. Acmite Market Intelligence, 2011.
- [16] P. Eaton, A. Ragusa, C. Clavel, C. T. Rojas, P. Graham, R. V. Durn, and S. Penads, "Glyconanoparticle-dna interactions: An atomic force microscopy study," *IEEE Transactions on NanoBioscience*, vol. 6, no. 4, pp. 309–318, 2007.
- [17] V. V. Srinivasu and W. J. Perold, "Observation of shapiro-steps in afm-plough micron-size ybco planar constrictions," *IEEE Transactions on Applied Superconductivity*, vol. 6, no. 4, pp. 309–318, 2007.
- [18] N.-K. Chang and S.-H. Chang, "Determining mechanical properties of carbon microcoils using lateral force microscopy," *IEEE Transactions on Nanotechnology*, vol. 7, no. 2, pp. 197–201, 2008.
- [19] Z. Chen and X. Tan, "A control-oriented and physics-based model for ionic polymer–metal composite actuators," *IEEE/ASME Transactions on Mechatronics*, vol. 13, no. 5, pp. 519 –529, 2008.
- [20] H. Lei, C. Lim, and X. Tan, "Modeling and inverse compensation of dynamics of base-excited ionic polymer-metal composite sensors," *Journal of Intelligent Material Systems and Structures*, 2012, under review.
- [21] P. G. de Gennes, K. Okumura, M. Shahinpoor, and K. Kim, "Mechanoelectric effects in ionic gels," *Europhysics Letters*, vol. 50, no. 4, pp. 513 – 518, 2000.

- [22] R. Iyer and X. Tan, "Control of hysteretic systems through inverse compensation: Inversion algorithms, adaptation, and embedded implementation," *IEEE Control Systems Magazine*, vol. 29, no. 1, pp. 83–99, 2009.
- [23] D. Croft, G. Shed, and S. Devasia, "Creep, hysteresis, and vibration compensation for piezoactuators: Atomic force microscopy application," *Journal of Dynamic Systems, Measurement, and Control*, vol. 123, no. 1, pp. 35–43, 2001.
- [24] G. V. Webb, D. C. Lagoudas, and A. J. Kurdila, "Hysteresis modeling of sma actuators for control applications," *Journal of Intelligent Material Systems and Structures*, vol. 9, no. 6, pp. 432–448, 1998.
- [25] D. Davino, C. Natale, S. Pirozzi, and C. Visone, "Phenomenological dynamic model of a magnetostrictive actuator," *Physica B: Condensed Matter*, vol. 343, no. 1-4, pp. 112 – 116, 2004.
- [26] M. A. Janaideh, S. Rakheja, and C.-Y. Su, "A generalized Prandtl-Ishlinskii model for characterizing the hysteresis and saturation nonlinearities of smart actuators," *Smart Materials and Structures*, vol. 18, pp. 1–9, 2009.
- [27] A. Visintin, *Differential Models of Hysteresis*. New York: Springer-Verlag, 1994.
- [28] M. Brokate and J. Sprekels, *Hysteresis and Phase Transitions*. New York: Springer-Verlag, 1996.
- [29] I. Mayergoyz, *Mathematical Models of Hysteresis*. New York: Springer-Verlag, 1991.
- [30] C. Natale, F. Velardi, and C. Visone, "Identification and compensation of Preisach hysteresis models for magnetostrictive actuators," *Physica B: Condensed Matter*, vol. 306, no. 1-4, pp. 161 – 165, 2001.
- [31] R. Iyer, X. Tan, and P. Krishnaprasad, "Approximate inversion of the Preisach hysteresis operator with application to control of smart actuators," *IEEE Transactions on Automatic Control*, vol. 50, no. 6, pp. 798 – 810, 2005.
- [32] K. Kuhnen, "Modeling, identification and compensation of complex hysteretic nonlinearities - A modified Prandtl-Ishlinskii approach," *European Journal of Control*, vol. 9, no. 4, pp. 407–418, 2003.
- [33] G. Tao and P. V. Kokotovic, "Adaptive control of plants with unknown hystereses," *IEEE Transactions on Automatic Control*, vol. 40, no. 2, pp. 200–212, 1995.

- [34] P. Ge and M. Jouaneh, "Tracking control of a piezoceramic actuator," *IEEE Transactions on Control Systems Technology*, vol. 4, no. 3, pp. 209–216, 1996.
- [35] X. Tan and J. S. Baras, "Adaptive identification and control of hysteresis in smart materials," *IEEE Transactions on Automatic Control*, vol. 50, no. 6, pp. 827–839, 2005.
- [36] J. Schfer and H. Janocha, "Compensation of hysteresis in solid-state actuators," *Sensors and Actuators A: Physical*, vol. 49, no. 1-2, pp. 97 – 102, 1995.
- [37] S. Salapaka, A. Sebastian, J. P. Cleveland, and M. V. Salapaka, "High bandwidth nanopositioner: A robust control approach," *Review of Scientific Instruments*, vol. 73, no. 9, pp. 3232–3241, 2002.
- [38] Y. Wu and Q. Zou, "Iterative control approach to compensate for both the hysteresis and the dynamics effects of piezo actuators," *IEEE Transactions on Control Systems Technology*, vol. 15, no. 5, pp. 936–944, 2007.
- [39] S. Bashash and N. Jalili, "Robust adaptive control of coupled parallel piezo-flexural nanopositioning stages," *IEEE/ASME Transactions on Mechatronics*, vol. 14, pp. 11–20, 2009.
- [40] A. Cavallo, C. Natale, S. Pirozzi, and C. Visone, "Effects of hysteresis compensation in feedback control systems," *IEEE Transactions on Magnetics*, vol. 39, no. 3, pp. 1389 – 1392, 2003.
- [41] X. Tan and H. K. Khalil, "Two-time-scale averaging of systems involving operators and its application to adaptive control of hysteretic systems," in *Proceedings of the 2009 American Control Conference*, 2009, pp. 4476–4481.
- [42] J. H. Ahrens, X. Tan, and H. K. Khalil, "Multirate sampled-data output feedback control with application to smart material-actuated systems," *IEEE Transactions on Automatic Control*, vol. 54, no. 11, pp. 2518–2529, 2009.
- [43] P. A. Ioannou and B. Fidan, *Adaptive control tutorial*. Society for Industrial and Applied Mathematics, Philadelphia, Pa. :, 2006.
- [44] X. Chen, T. Hisayama, and C.-Y. Su, "Pseudo-inverse-based adaptive control for uncertain discrete time systems preceded by hysteresis," *Automatica*, vol. 45, pp. 469–476, 2008.
- [45] H. C. Liaw and B. Shirinzadeh, "Neural network motion tracking control of piezo-actuated flexure-based mechanisms for micro-/nanomanipulation," *IEEE/ASME Transactions on Mechatronics*, vol. 14, no. 5, pp. 517–527, 2009.

- [46] X. Tan and O. Bennani, “Fast inverse compensation of preisach-type hysteresis operators using field-programmable gate arrays,” in *American Control Conference, 2008*, 2008, pp. 2365–2370.
- [47] C. Lee and S. M. Salapaka, “Fast robust nanopositioning: A linear-matrix-inequalities-based optimal control approach,” *IEEE/ASME Transactions on Mechatronics*, vol. 14, no. 4, pp. 414–422, 2009.
- [48] Q. Zou, K. K. Leang, E. Sadoun, M. J. Reed, and S. Devasia, “Control issues in high-speed AFM for biological applications: Collagen imaging example,” *Asian Journal of Control*, vol. 6, no. 2, pp. 164–178, 2004.
- [49] J. Zhong and B. Yao, “Adaptive robust precision motion control of a piezoelectric positioning stage,” *IEEE Transactions on Control Systems Technology*, vol. 16, pp. 1039–1046, 2008.
- [50] Z.-J. Yang, S. Hara, S. Kanae, K. Wada, and C.-Y. Su, “An adaptive robust nonlinear motion controller combined with disturbance observer,” *IEEE Transactions on Control Systems Technology*, vol. 18, no. 2, pp. 454–462, 2010.
- [51] J. Yi, S. Chang, and Y. Shen, “Disturbance-observer-based hysteresis compensation for piezoelectric actuators,” *IEEE/ASME Transactions on Mechatronics*, vol. 14, no. 4, pp. 454–462, 2009.
- [52] M. Edardar, X. Tan, and H. K. Khalil, “Sliding-mode tracking control of piezo-actuated nanopositioners,” in *Proceedings of the 2012 American Control Conference*, 2012.
- [53] E. J. Davison, “The output control of linear time-invariant multivariable systems with unmeasurable arbitrary disturbances,” *IEEE Transactions on Automatic Control*, vol. 17, no. 5, pp. 621–630, 1972.
- [54] ———, “The robust control of a servomechanism problem for linear time-invariant multivariable systems,” *IEEE Transactions on Automatic Control*, vol. 21, pp. 25–34, 1976.
- [55] B. Francis and W. Wonham, “The internal model principle for linear multivariable regulators,” *Applied Mathematics and Optimization*, vol. 2, pp. 170–194, 1975.
- [56] B. A. Francis, “The linear multivariable regulator problem,” *SIAM Journal of Control and Optimization*, vol. 15, pp. 486–505, 1977.
- [57] A. Isidori and C. I. Byrnes, “Output regulation of nonlinear systems,” *IEEE Transactions on Automatic Control*, vol. 35, no. 2, pp. 131–140, 1990.

- [58] R. Decarlo, M. Branicky, S. Pettersson, and B. Lennartson, “Perspectives and results on the stability and stabilizability of hybrid systems,” *Proceedings of the IEEE*, vol. 88, no. 7, pp. 1069–1082, July 2000.
- [59] J. Shen, W. Jywe, and H. Chiang, “Precision tracking control of a piezoelectric-actuated system,” in *Proceedings of the 15th Mediterranean Conference on Control and Automation*, 2007.
- [60] P. J. Antsaklis and A. N. Michel, *A Linear Systems Primer*. Birkhäuser, 2007.
- [61] X. Tan and R. Iyer, “Modeling and control of hysteresis: Introduction to the special section,” *IEEE Control Systems Magazine*, vol. 29, no. 1, pp. 26–29, 2009.
- [62] L. Xie and I. Petersen, “Perfect regulation with cheap control for uncertain linear systems: A Riccati equation approach,” *IET Control Theory Applications*, vol. 2, pp. 782–794, 2008.
- [63] A. V. Pokrovskii and M. Brokate, “Asymptotically stable oscillations in systems with hysteresis nonlinearities,” *Journal of Differential Equations*, vol. 150, pp. 98–123, 1998.
- [64] H. K. Khalil, *Nonlinear Systems*, 3rd ed. Upper Saddle River, NJ: Prentice Hall, 2002.
- [65] K. Zhou, J. C. Doyle, and K. Glover, *Robust and Optimal Control*, 3rd ed. Upper Saddle River, NJ: Prentice Hall, 1996.
- [66] G. P. Tolstov, *Fourier Series*. Prentice-Hall, Inc., 1962.
- [67] A. Esbrook, M. Guibord, X. Tan, and H. K. Khalil, “Control of systems with hysteresis via servocompensation and its application to nanopositioning,” in *Proceedings of the 2010 American Control Conference*, 2010, pp. 6531–6536.
- [68] A. Serrani, A. Isidori, and L. Marconi, “Semiglobal nonlinear output regulation with adaptive internal model,” *IEEE Transactions on Automatic Control*, vol. 46, no. 8, pp. 1178–1194, 2001.
- [69] V. Nikiforov, “Adaptive nonlinear tracking with complete compensation of unknown disturbances,” *European Journal of Control*, vol. 4, pp. 132–139, 1998.
- [70] S. Seshagiri and H. K. Khalil, “Output feedback control of nonlinear systems using rbf neural networks,” *IEEE Transactions on Neural Networks*, vol. 11, pp. 69–79, 2000.

- [71] A. Isidori, L. Marconi, and L. Praly, “A design solution to the problem of adaptive output regulation for nonlinear minimum-phase systems,” in *Decision and Control (CDC), 2010 49th IEEE Conference on*, dec. 2010, pp. 2704–2709.
- [72] L. J. Brown and Q. Zhang, “Periodic disturbance cancellation with uncertain frequency,” *Automatica*, vol. 40, no. 4, pp. 631–637, 2004.
- [73] M. Bodson and S. C. Douglas, “Adaptive algorithms for the rejection of sinusoidal disturbances with unknown frequency,” *Automatica*, vol. 33, no. 12, pp. 2213–2221, 1997.
- [74] J. Lu and L. J. Brown, “Internal model principle-based control of exponentially damped sinusoids,” *International Journal of Adaptive Control and Signal Processing*, vol. 24, no. 3, pp. 219–232, 2010.
- [75] Y. Wang, K. Chu, and T.-C. Tsao, “Adaptive rejection of stochastic and deterministic sinusoidal disturbances with unknown frequency,” in *Proceedings of the 2009 American Control Conference*, 2009, pp. 5641–5646.
- [76] A. Esbrook, X. Tan, and H. K. Khalil, “Control of systems with hysteresis via servocompensation and its application to nanopositioning,” *IEEE Transactions on Control Systems Technology*, 2012, to appear.
- [77] A. Esbrook and X. Tan, “Harmonic analysis for hysteresis operators with application to control design for systems with hysteresis,” in *Proceedings of the 2012 American Control Conference*, 2012, pp. 1652–1657.
- [78] A. Isidori, L. Marconi, and A. Serrani, “Robust nonlinear motion control of a helicopter,” *IEEE Transactions on Automatic Control*, vol. 48, no. 3, pp. 413–426, 2003.
- [79] H. Elliott and G. C. Goodwin, “Adaptive implementation of the internal model principle,” in *Proceedings of the 23rd IEEE Conference on Decision and Control*, 1984, pp. 1292–1297.
- [80] M. Mojiri and A. R. Bakhshai, “An adaptive notch filter for frequency estimation of a periodic signal,” *IEEE Transactions on Automatic Control*, vol. 49, no. 2, pp. 314–318, 2004.
- [81] A. R. Teel, L. Moreau, and D. Nesić, “A unified framework for input-to-state stability in systems with two time scales,” *IEEE Transactions on Automatic Control*, vol. 48, no. 9, pp. 1526–1544, 2003.
- [82] S. Sastry and M. Bodson, *Adaptive control : stability, convergence, and robustness*. Prentice Hall, Englewood Cliffs, N.J. :, 1989.

- [83] L. Riccardi, D. Naso, B. Turchiano, H. Janocha, and D. K. Palagachev, “On PID control of dynamic systems with hysteresis using a Prandtl-Ishlinskii model,” in *Proceedings of the 2012 American Control Conference*, 2012, pp. 1670–1678.
- [84] S. Valadkhan, K. Morris, and A. Khajepour, “Stability and robust position control of hysteretic systems,” *International Journal of Robust and Nonlinear Control*, vol. 20, no. 4, pp. 460–471, 2010.
- [85] B. Jayawardhana, H. Logemann, and E. P. Ryan, “PID control of second-order systems with hysteresis,” *International Journal of Control*, 2008.
- [86] R. Gorbet, K. Morris, and D. Wang, “Passivity-based stability and control of hysteresis in smart actuators,” *IEEE Transactions on Control Systems Technology*, vol. 9, no. 1, pp. 5–16, 2001.
- [87] B. Jayawardhana and V. Andrieu, “Sufficient conditions for dissipativity on Duhem hysteresis model,” in *Proceedings of the 48th IEEE Conference on Decision and Control*, dec. 2009, pp. 4378–4383.
- [88] A. Barreiro and A. Baos, “Input output stability of systems with backlash,” *Automatica*, pp. 1017–1024, 2005.
- [89] S. Tarbouriech, C. Prieur, and I. Queinnec, “Stability analysis for linear systems with input backlash through sufficient LMI conditions,” *Automatica*, pp. 1911–1915, 2010.
- [90] S. Boyd, L. E. Ghaoui, E. Feron, and V. Balakrishnan, *Linear Matrix Inequalities in System and Control Theory*. SIAM, 1994.
- [91] N. Kottenstette and P. J. Antsaklis, “Relationships between positive real, passive dissipative, & positive systems,” in *Proceedings of the 2010 American Control Conference*, 2010, pp. 409–416.
- [92] J. W. Macki, P. Nistri, and P. Zecca, “Periodic oscillations in systems with hysteresis,” *Rocky Mountain J. Math*, vol. 22, no. 2, 1992.
- [93] A. Cavallo, C. Natale, S. Pirozzi, and C. Visone, “Limit cycles in control systems employing smart actuators with hysteresis,” *Mechatronics, IEEE/ASME Transactions on*, vol. 10, no. 2, pp. 172–180, april 2005.
- [94] I. Babaa, T. Wilson, and Y. Yu, “Analytic solutions of limit cycles in a feedback-regulated converter system with hysteresis,” *IEEE Transactions on Automatic Control*, vol. 13, no. 5, pp. 524–531, oct 1968.

- [95] A. Girard, “Computation and stability analysis of limit cycles in piecewise linear hybrid systems,” in *1st IFAC Conference on Analysis and Design of Hybrid Systems*, 2003, pp. 181–186.